The Impact of Plasma Wall Interactions on the Burn Dynamics of Tokamak Reactors

M.R. Gordinier

May 1980

UWFDM-356

Ph.D. thesis.

FUSION TECHNOLOGY INSTITUTE

UNIVERSITY OF WISCONSIN

MADISON WISCONSIN

The Impact of Plasma Wall Interactions on the Burn Dynamics of Tokamak Reactors

M.R. Gordinier

Fusion Technology Institute
University of Wisconsin
1500 Engineering Drive
Madison, WI 53706

http://fti.neep.wisc.edu

May 1980

UWFDM-356

Ph.D. thesis.

IMPACT OF PLASMA WALL INTERACTIONS ON THE BURN DYNAMICS OF TOKAMAK REACTORS

BY

MICHAEL RAYMOND GORDINIER

A thesis submitted in partial fulfillment of the
requirements for the degree of

DOCTOR OF PHILOSOPHY
(Nuclear Engineering)

at the

UNIVERSITY OF WISCONSIN-MADISON

1980

ABSTRACT

IMPACT OF PLASMA WALL INTERACTIONS ON THE BURN DYNAMICS OF TOKAMAK REACTORS

Michael Raymond Gordinier

Under the supervision of Professor Robert William Conn

To date, research into the physics of plasma transport has centered on the core of the discharge, resulting in the development of models which seek to simulate tokamak dynamics. It is becoming increasingly recognized, however, that the global characteristics of the plasma may be determined more by plasma-wall interactions in the scrape-off zone than by plasma physics.

A zero dimensional edge model has been developed which incorporates the relevant plasma-wall interactions of the scrape-off zone. This model provides the self-consistent boundary conditions and fuel/impurity influxes required by one dimensional radial transport codes. By coupling the two codes, the impact of plasma-wall interactions on the burn dynamics of tokamaks can be assessed.

Simulations using this edge model have demonstrated the impurity control features of a cool gas blanket under a wide variety of gas flow rates. While the simulations were not carried to plasma equilibrium, the transient creation and operation of a gas blanket was observed.

ACKNOWLEDGEMENTS

I would like to acknowledge my advisor, Professor Robert W. Conn, for his continual guidance and encouragement. I am indebted to him for his many helpful suggestions and for sharing with me his unique approach to problem solving.

I am also grateful for the support and guidance provided by Professor G.A. Emmert whose interest in both plasma theory and computation provided the driving force for much of my work.

Special thanks are due to Drs. K. Audenaerde and W. Houlberg both of whom initiated my exposure to computational plasma physics. Discussions with fellow research members in the Fusion Design group, especially D. Blackfield and H. Attaya, have been extremely valuable.

The patience and understanding of my wife, Kristine, has played a major role in the successful completion of my work. Her steadfast support during times of frustration provided me with the encouragement necessary to continue.

Last but not least, I would like to acknowledge Ms. Diana Reuschlein whose attention to detail in the preparation of this thesis was masterful indeed.

LIST OF FIGURES

LIST OF TABLES

TABLE OF CONTENTS

TABLE OF CONTENTS (Cont.)

CHAPTER 1

INTRODUCTION

During the last decade great strides have been made in both identifying and quantifying those processes which govern the behavior of tokamak discharges. To date research into the physics of plasma confinement, heating, and transport has produced theoretical and empirical models which seek to simulate tokamak dynamics. While these prescriptions for plasma behavior have met with some success, it is becoming increasingly recognized that the global characteristics of the plasma may be determined more by plasma/wall interactions in the scrape-off zone than by classical plasma physics.

The scrape-off zone, defined as the area between the separatrix or limiter tip and the vacuum wall, is recognized as being critical to the modelling of plasma discharges since this region is the source of impurities which degrade plasma performance. In addition, reflection, trapping, and re-emission processes at the wall have a large impact on the overall density and energy balance of the plasma. The plasma/wall interactions occuring in the scrape-off zone couple the plasma core to the wall (see Figure (1-1)). A model of the physics of the scrape-off zone would: (1) provide self-consistent boundary conditions for the

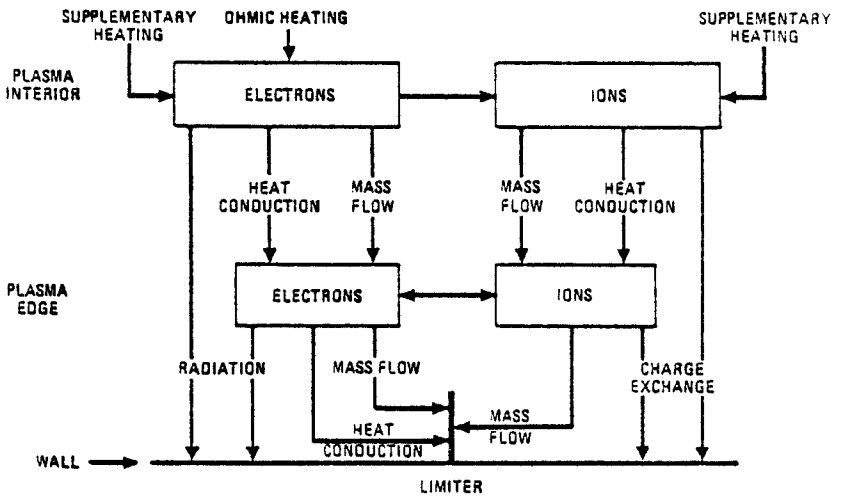

Figure (1-1) Schematic diagram of Tokamak Power Flow.

time evolution of the core plasma, and (2) provide self-consistent hydrogenic and impurity recycling information, both of which are required if simulations of future CTR devices are to be believed.

The goal of this work is the creation of a model for the scrape-off zone of a tokamak suitable for inclusion in a one dimensional radial transport code. In Chapter 2 the fluid equations for tokamak transport are described and in Chapter 3 the numerical scheme used in solving these coupled partial differential equations is examined. In Chapter 4 an exceptionally compact and fast algorithm for one and two specie neutral transport is developed. An indepth review of those plasma/wall interactions which are believed to occur in the scrape-off zone is given in Chapter 5, while the various schemes for controlling the impact of these reactions on the core plasma is discussed in Chapter 6. Chapter 7 documents the development of a zero dimensional model for the scrape-off layer and describes how it interfaces with the 1D radial transport code. In Chapter 8 the impact of this model on tokamak simulations is investigated for a variety of parameters. In Chapter 9 a summary of the results will be presented and conclusions drawn.

CHAPTER 2

TOKAMAK FLUID EQUATIONS

The derivation of the fluid equations which describe the temporal and spatial evolution of tokamak plasmas follows from the Boltzmann equation[1]:

$$\frac{\partial f_j}{\partial t} + \vec{V}_j \cdot \nabla f_j + \frac{e_j}{m_j} (\vec{E} + \vec{V}_j \times \vec{B}) \cdot \nabla_V f_j = \sum_i C_{ij} \qquad (2\text{-}1)$$

where f_j is the velocity space distribution function for specie j, $\vec{E}$ and $\vec{B}$ are the macroscopic electric and magnetic fields and C_{ij} is the collision operator which models the transfer of energy and momentum between species i and j.

By taking the moments of equation (2-1), the fluid particle and energy balance equations for specie j are obtained:

$$\frac{\partial n_j}{\partial t} + \nabla \cdot \Gamma_j = S_j - L_j \qquad (2\text{-}2)$$

$$\partial/\partial t \ (3/2 \ n_j k T_j) + \nabla \cdot Q_j^* = S_j^* - L_j^* \qquad (2\text{-}3)$$

where: Γ_j = specie j particle flux

Q_j^* = specie j energy flux = convection + conduction

S_j, L_j = specie j volumetric particle sources/losses

S_j^*, L_j^* = specie j volumetric energy sources/losses

n_j = density of specie j

T_j = temperature of specie j

If the plasma consists of electrons, deuterons, tritons, alpha particles and an impurity specie, the tokamak fluid equations become in cylindrical coordinates:

$$\frac{\partial n_D}{\partial t} + \frac{1}{r}\frac{\partial}{\partial r}(r\Gamma_D) = S^D_{IONIZ} + S^D_{NB} + S^D_{PEL} - L_{FUS} + L^D_{CX} - L^D_{NB} \qquad (2\text{-}4)$$

$$\frac{\partial n_T}{\partial t} + \frac{1}{r}\frac{\partial}{\partial r}(r\Gamma_T) = S^T_{IONIZ} + S^T_{NB} + S^T_{PEL} - L_{FUS} + L^T_{CX} - L^T_{NB} \qquad (2\text{-}5)$$

$$\frac{\partial n_\alpha}{\partial t} + \frac{1}{r}\frac{\partial}{\partial r}(r\Gamma_\alpha) = S^\alpha_{IONIZ} + L_{FUS} \qquad (2\text{-}6)$$

$$\frac{\partial n_z}{\partial t} + \frac{1}{r}\frac{\partial}{\partial r}(r\Gamma_z) = S^z_{IONIZ} \qquad (2\text{-}7)$$

$$\frac{\partial}{\partial t}\left(\frac{3}{2} n_e k T_e\right) + \frac{1}{r}\frac{\partial}{\partial r}\left[r(3/2\ \Gamma_e k T_e + Q_e)\right] = P_\Omega + P^e_{Rf}$$

$$+ P^e_{NB} - Q_{ei} - P_{Rad} - P^e_{IONIZ} + P^e_\alpha \qquad (2\text{-}8)$$

$$\frac{\partial}{\partial t}\left(3/2\, n_i k T_i\right) + \frac{1}{r}\frac{\partial}{\partial r}\left[r\left(3/2\, \Gamma_i k T_i + Q_i\right)\right] = P_\alpha^i + P_{Rf}^i$$

$$+ P_{NB}^i + Q_{ei} - P_{IONIZ}^i - P_{CX} \qquad (2\text{-}9)$$

where: S_{IONIZ}^j = source of ions due to ionization of recycling and externally introduced neutrals of specie j

S_{NB}^j = source of ions due to the ionization of neutral beams

S_{PEL}^j = source of ions due to pellet injection.

L_{FUS} = thermal fusion term = $n_D n_T \langle\sigma v\rangle_{DT}$

L_{CX}^j = loss/source of ions of specie j due to charge-exchange events with other species.

L_{NB}^j = loss of specie j due to beam/plasma fusions

Q_e, Q_i = electron/ion heat flow due to conduction

P_Ω = ohmic heating source.

$P_{Rf}^{e,i}$ = electron/ion RF power source.

$P_{NB}^{e,i}$ = electron/ion neutral beam power source.

Q_{ei} = electron-ion rethermalization term.

$P_\alpha^{e,i}$ = electron/ion alpha power source.

P_{Rad} = total radiative losses (bremsstralung + impurity)

P_{CX} = charge exchange power loss.

The process of ohmic heating is modelled using the Spitzer resistivity η_s [2] with neoclassical corrections:

$$P_\Omega = E_\phi J_\phi = \eta_{NC} J_\phi^2 \tag{2-10}$$

where:
$$\eta_{NC} = \eta_s [1 - 1.95(r/R)^{\frac{1}{2}} + .95(r/R)]^{-1} \tag{2-11}$$

The rethermalization term Q_{ei} is based on the classical expression:

$$Q_{ei} \equiv \frac{3n_e}{\tau_{ei}} \left(\frac{m_e}{m_i}\right) (kT_e - kT_i) \tag{2-12}$$

where $(\tau_{ei})^{-1}$ is the electron-ion collision frequency.

The fraction of alpha energy going to both electrons (f_e) and ions (f_i) is calculated using the expressions developed by Houlberg [3] for the thermalization of a high energy particle in a multispecies plasma. An approximation to the exact expression yields:

$$f_i \simeq \left(\frac{T_e}{5 \times 10^4}\right) - .37\left(\frac{T_e}{5 \times 10^4}\right)^{7/4}$$
$$f_e = 1 - f_i \tag{2-13}$$

The terms $S_{IONIZ}^{D,T}$, L_{CX}^{j}, and P_{CX} are evaluated in the neutral transport routine, SPUDNUT [4], which is completely described in Chapter 4. The pellet injection terms, $S_{PEL}^{D,T}$, are evaluated using the ORNL pellet injection code, PELLET [5], based on the ablation

model of Milorna and Foster. The treatment of impurity radiation is described in Section (2.5) and derives from the work of Post, et. al.[6].

It should be noted that in the model, the Maxwell equations:

$$\frac{\partial B_\theta}{\partial t} = \frac{\partial E_z}{\partial r} \tag{2-14}$$

$$\mu_o \frac{\partial J_z}{\partial t} = \frac{1}{r} \frac{\partial}{\partial r} \left(r \frac{\partial E_z}{\partial r} \right) \tag{2-15}$$

and Ohm's law:

$$E_z = \eta J_z \tag{2-16}$$

are not solved. The starting point of the simulation is an ohmic heating equilibrium in which the current profile is assumed to be frozen into the plasma, hence the time-dependent equations need not be solved. However, they should be included in any model of start-up.

The electron density and radial flux is determined by the constraint of charge neutrality:

$$n_e = \sum_j Z_j n_j \tag{2-17}$$

$$\Gamma_e = \sum_j Z_j \Gamma_j \tag{2-18}$$

Z_j being the ionic charge of specie j. It is also assumed that the deuterium and tritium temperatures are equal, this following from the magnitude of the rethermalization term.

In order to close these coupled transport equations, the particle and heat fluxes (Γ_j, Q_j) are defined in terms of macroscopic density and temperature gradients via a set of transport coefficients (D,χ)[7].

$$\Gamma_j \equiv -D_{jD}\frac{\partial n_D}{\partial r} - D_{jT}\frac{\partial n_T}{\partial r} - D_{j\alpha}\frac{\partial n_\alpha}{\partial r} - D_{jz}\frac{\partial n_z}{\partial r} - D_{jT_e}\frac{\partial T_e}{\partial r} - D_{jT_i}\frac{\partial T_i}{\partial r}$$

$$Q_j \equiv -\chi_{jD}\frac{\partial n_D}{\partial r} - \chi_{jT}\frac{\partial n_T}{\partial r} - \chi_{j\alpha}\frac{\partial n_\alpha}{\partial r} - \chi_{jz}\frac{\partial n_z}{\partial r} - \chi_{jT_e}\frac{\partial T_e}{\partial r} - \chi_{jT_i}\frac{\partial T_i}{\partial r} \tag{2-19}$$

The functional dependence of these transport coefficients on the parameters of the plasma such as density, temperature and geometry follow from: (1) analyzing the orbits and collisions of particles in a given magnetic configuration and deriving expressions for the resulting diffusion coefficients, or (2) estimating the transport scaling empirically from present day experiments. Obviously (1) represents the preferred course of action. However, when predicted scalings are not observed experimentally (e.g. electron transport in tokamaks), scenario (2) is adopted.

For completeness, a brief review of the relevant transport coefficients following from both (1) and (2) will be presented in the following section.

2.1 Classical Diffusion

Classical cross-field transport represents the lower limit for diffusion from a given magnetic configuration. In a uniform magnetic field, charged particles gyrate about field lines with a gyroradius ρ equal to $V_\perp/\omega_c$. Simple binary Coulomb collisions cause the guiding center of the particle to step from one magnetic surface to another. Such a random walk diffusion process can be characterized by a transport coefficient D which scales like:

$$D \sim (\Delta x)^2/\Delta t \tag{2-20}$$

where (Δx) represents the characteristic step size of the process and $(\Delta t)^{-1}$ the frequency with which such steps occur. Choosing (Δx) as the gyroradius ρ and $(\Delta t)^{-1}$ as the collision frequency ν, the classical diffusion coefficient becomes:

$$D_{CLASS} \sim \rho^2\nu \tag{2-21}$$

2.2 Neoclassical Diffusion

However, in toroidal geometry, the magnetic field is far from uniform, varying as $(R)^{-1}$, where R is the major radius of the torus. This feature of toroidal topology has the following implication. As ions travel along the magnetic flux surfaces they encounter regions of increasing magnetic field B. It follows from the invarience of the magnetic moment $\mu(= V_\perp^2/2B)$ that a

class of ions will be reflected in regions of large B (small R) and become trapped in local magnetic mirrors. These non-circulating ions have orbits resembling a banana as seen in Figure (2-1). Since the fraction of such trapped particles can be shown to be roughly $\sqrt{2r/R}$, at any given time some 60% of all ions are trapped. Thus, if trapped particles are poorly confined, overall plasma containment will suffer. When toroidal transport depends upon geometric and magnetic configurations, the transport is termed neoclassical[9].

The collisionality of the plasma, characterized by the ratio of effective scattering frequency to toroidal bounce frequency for collisional scattering out of the trapped region of velocity space, taking into account the fraction of trapped particles, scales as:

$$\nu_{eff} \simeq \nu(R/r) \tag{2-22}$$

Defining the bounce time (τ_B) as the time required for a trapped particle to complete one orbit yields:

$$\tau_B \simeq qR/V_{\parallel} \tag{2-23}$$

The dimensionless quantity $\nu^* = \nu_{eff}\,\tau_B$ then defines the collisionality of the plasma. If $\nu^* >> 1$, a particle will scatter out of the trapped region of velocity space before it completes one bounce period. Conversely, if $\nu^* << 1$, a trapped particle

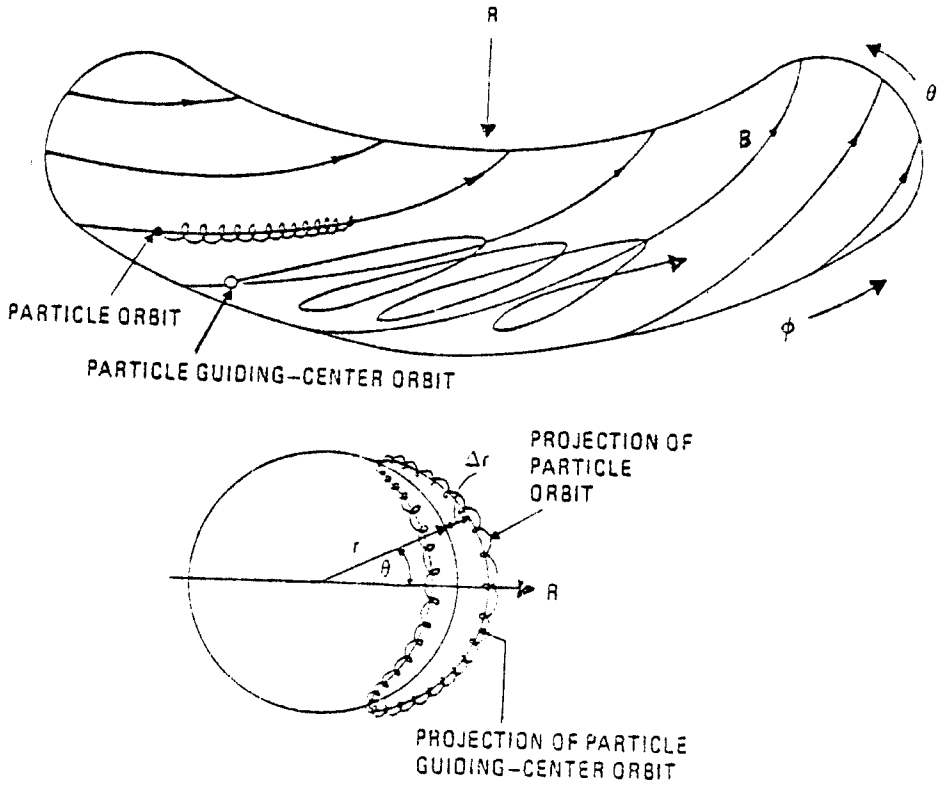

Figure (2-1) Trapped particle orbits in toroidal geometry [Ref. 2-8].

will execute many bounce periods before undergoing a de-trapping collision.

For ν^* << 1, particles are said to be in the collisionless or "banana" regime. The characteristic radial excursion (or step size) of such an orbit is given by:

$$\Delta r \simeq (r/R)^{\frac{1}{2}} \rho_p \tag{2-24}$$

where ρ_p is the gyroradius of the particle in the poloidal field. De-trapping collisions occur at the rate ν_{eff} for a fraction $\sqrt{r/R}$ of all particles. Thus the diffusion coefficient for this regime scales as:

$$D_{Banana} \simeq (r/R)^{\frac{1}{2}} \nu \rho_p^2 \tag{2-25}$$

For ν^* >> 1, particles are said to be in the collisional or "Pfirsch-Schülter" regime. Collisions are so frequent that a completed orbit is unlikely. The diffusion coefficient in this regime scales as:

$$D_{PS} \simeq q^2 \rho^2 \nu \tag{2-26}$$

Finally, in the range $\nu^* \sim 1$, particles are said to be in the "plateau regime" since the diffusion coefficient can be shown to be independent of collision frequency and scale as:

$$D_{plat} \simeq \left(\frac{V}{qR}\right) q^2 \rho^2 \tag{2-27}$$

A plot of neoclassical diffusion coefficient versus collision frequency is given in Figure (2-2), in which the solid curve represents the smoother functional dependence of the exact diffusion coefficient.

In a similar fashion expressions for the ion thermal diffusivity, χ_i, can be derived for each regime of collisionality[9]:

$$\chi_i \text{ (Banana)} = .66\, n_i (r/R)^{\frac{1}{2}} \nu_i \rho_{iP}$$

$$\chi_i \text{ (Plateau)} = 1.9\, n_i \left(\frac{kT_i}{m_i}\right)^{\frac{1}{2}} \frac{q\rho_i^2}{R}$$

$$\chi_i \text{ (Pfirsch-Schülter)} = (1 + 1.6\, q^2)\, n_i \nu_i \rho_i^2 \qquad (2\text{-}28)$$

where: $\rho_i = (2m_i kT_i)^{\frac{1}{2}}/(eB_T)$

$$\rho_{iP} = \rho_i (B_T/B_P)$$

$$\nu_i = 4\sqrt{\pi}\, n_i e^4 \ln\Lambda_i / (3\sqrt{m_i}\, (kT_i)^{3/2}) \qquad (2\text{-}29)$$

Figure (2-3) is a plot of χ_i/χ_i (Plateau) versus the collisionality parameter ν^*. Again, the solid curve represents the exact functional dependence of χ_i on ν^*.

In conclusion, it should be noted that in present day toroidal experiments, ion transport is in reasonable agreement with the above neoclassical expressions. However, the

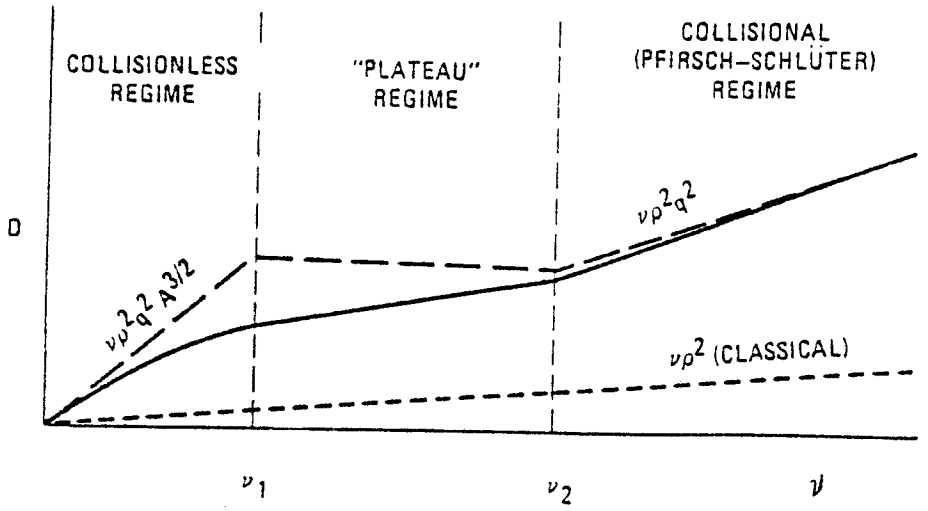

Figure (2-2) Neoclassical diffusion coefficient D as a function of collision frequency ν.

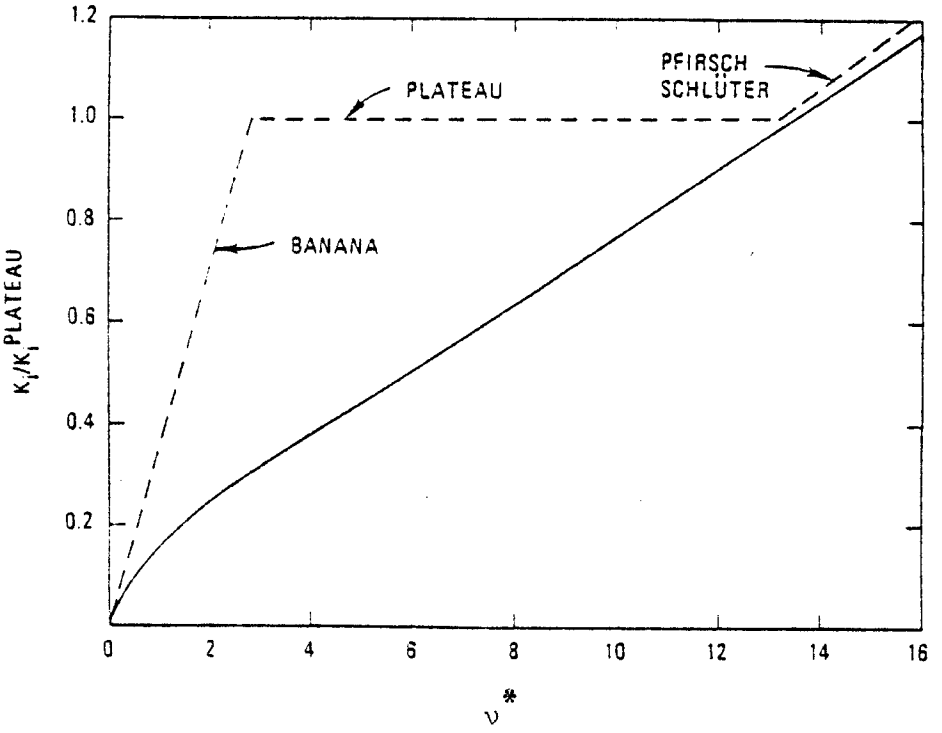

Figure (2-3) Normalized thermal diffusivity as a function of the collisionality parameter ν^*.

neoclassical theory of electron transport cannot account for the anomalously poor electron containment. This is dramatically shown in Figure (2-4) in which the neoclassically predicted and experimentally observed electron confinement times are plotted as a function of election density for ALCATOR. Thus, for the electrons, a more empirical approach to the determination of transport coefficients is taken.

2.3 Empirical Tokamak Scaling

Drawing upon the large data base obtained from tokamak experiments over the last decade, a statistical analysis of the functional dependence of the observed electron energy confinement time τ_e upon various system parameters has yielded several empirical expressions for τ_e (Table 2-1). Note that τ_e is observed to increase almost linearly with electron density and roughly as the square of the plasma minor radius.

In a global sense, if the main electron energy loss channel is due to transport alone, then the confinement time can be related to the transport coefficients by the expressions:

$$\tau_e \propto \frac{a^2}{D_e} , \frac{a^2}{\chi_e} \qquad (2\text{-}30)$$

Empirically $\tau_e \propto \bar{n}_e a^2$, implying that the transport coefficients scale as $(1/\bar{n}_e)$. In addition to this favorable density scaling, preliminary results from PLT injection experiments [17] (in which

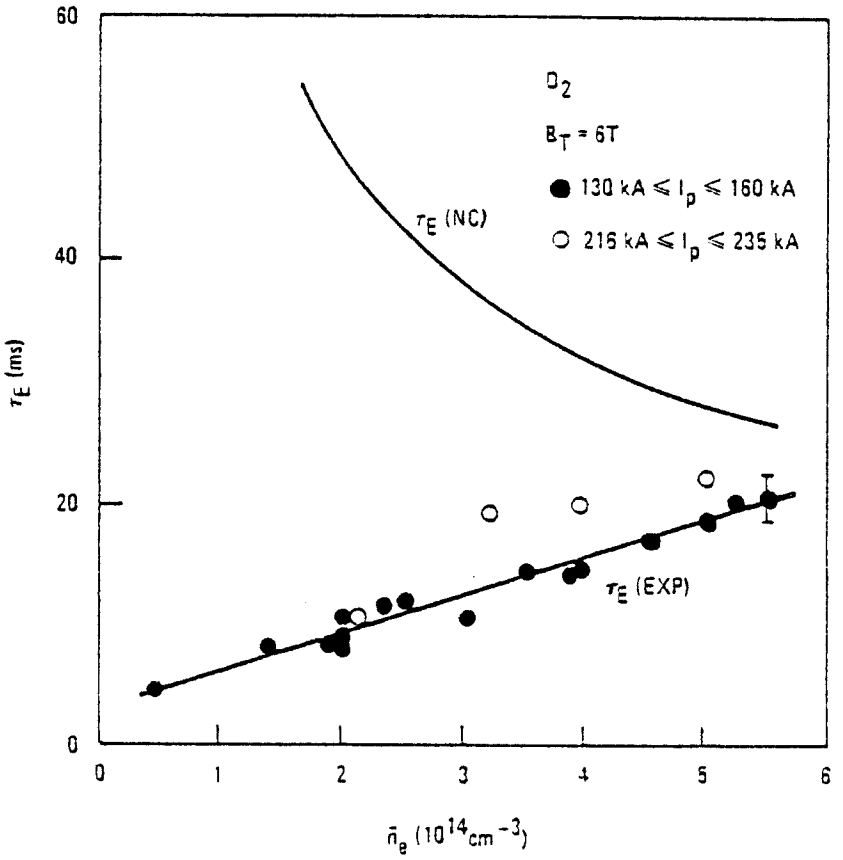

Figure (2-4) Neoclassical prediction and observed electron energy confinement time as a function of $\bar{n}_e$ [Ref. 2-10].

the plasma collisionality attained values characteristic of reactor conditions) indicate a favorable temperature dependence, scaling as $(1/T_e)$.

Recently several empirical scaling laws have been proposed which seek to model the anomalous transport of electrons in toroidal devices. Table (2-2) lists a few of these prescriptions.

2.4 Summary of Transport Scaling

In summary, expressions for ion transport based on classical and neoclassical theory were presented. Present day observations of ion transport spanning all collisionality regimes are in reasonable agreement with neoclassical predictions, differing at most by a factor of ~ 4. However, the neoclassical theory of electron transport is in poor agreement with experiment. Consequently, empirical estimates for electron transport have been made resulting in a number of popular scaling laws. The application of both neoclassical and empirical scaling in the simulation of future reactor conditions seems justifiable since the success of these scalings ranges from the very collisional (ALCATOR) to the reactor-like collisionless (PLT) regime.

2.5 Impurity Effects

The modelling of impurities in tokamaks can be divided into three areas of active concern: (1) the study of the generation mechanisms and subsequent introduction of impurities into the

plasma, (2) the transport of these impurities and (3) the effect of impurities on the discharge characteristics of the plasma. Progress in each of these areas is critical since the successful control of impurities is a key element in the creation of power producing fusion reactors.

The theoretical identification of the myriad sources of impurities is complicated by the lack of data concerning wall chemistry, desorption phenomena, atomic physics and the plasma environment present in the scrape-off layer. In addition, the experimental difficulties are compounded by the inherent inaccuracy of measuring low density, low temperature processes. Also, since the coupling between plasma effects and wall phenomena is so complete, it is difficult to experimentally seperate, analyze and unambiguously quantify these processes. A description of a theoretical model for the study of the impact of plasma/wall interactions on tokamak burn dynamics is given in detail in Chapter 7.

The transport of impurities is an essential aspect of reactor modelling since the accumulation of impurities will substantially limit burn times or may inhibit ignition altogether. Classical calculations indicate that the impurity concentration profile will follow the fuel profile as[19]:

$$n_z(r) \sim [n_i(r)]^Z \qquad (2\text{-}31)$$

where Z is the charge of the impurity. Recent experiments indicate that the inward transport of impurities is roughly that predicted by neoclassical theory but that an anomalous outward mechanism is preventing on-axis accumulation[20]. The theoretical treatment of impurity transport is complicated by the fact that an impurity may be in several charge states. In addition, fuel and impurity ions may be in different regimes of collisionality. The experimental determination of impurity transport coefficients is also difficult since little is known of impurity recycling or the spatial ionization source of incoming neutral impurities.

The effect of finite impurity concentration is perhaps the best understood aspect of the impurity problem. Impurities represent enhanced radiative losses via line, recombination and excitation radiation. These losses can severely limit the burn time of tokamaks and in extreme cases inhibit the ignition process altogether. To illustrate this latter case, refer to Fig. (2-5) in which the maximum impurity concentration consistent with DT ignition is plotted as a function of temperature. The radiative losses are based on the coronal equilibrium calculations of Reference [6]. Note that for candidate structural materials, a concentration of $\gtrsim$ .01% is sufficient to inhibit ignition at reasonable temperatures. This clearly demonstrates the importance of studying the impurity problem in detail. In addition, radiative losses may also precipitate the onset of

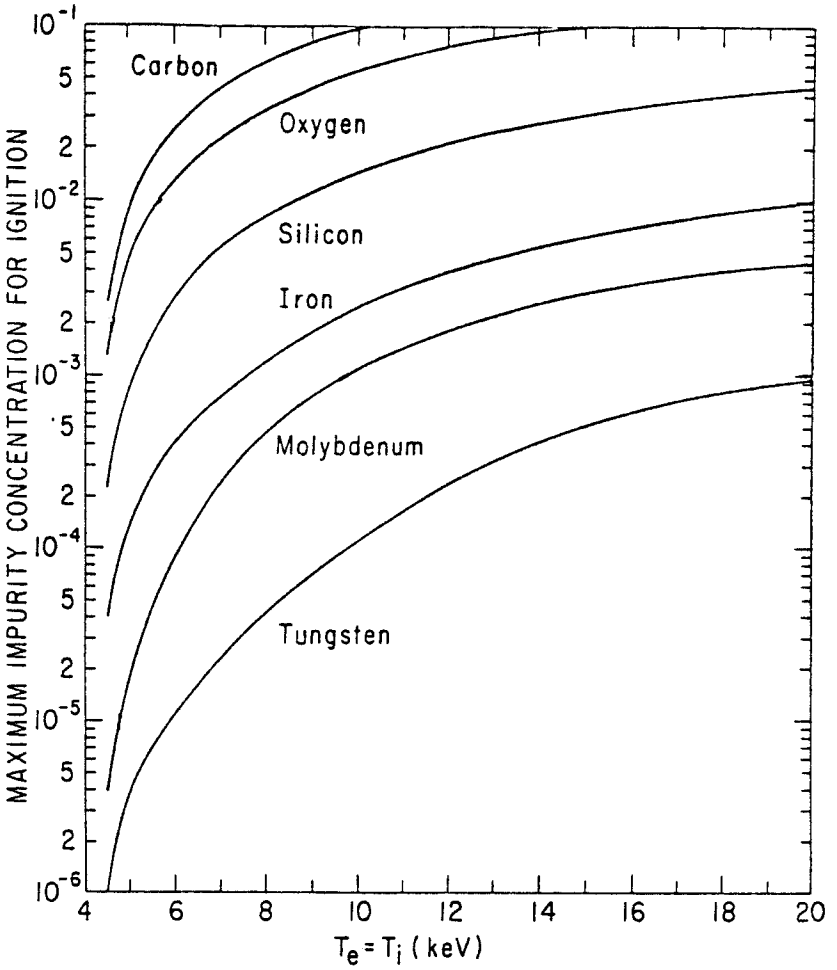

Figure (2-5) Maximum impurity fraction consistent with DT ignition for several species assuming non-radiative $\tau_e = \infty$.

plasma disruptions. Low Z edge cooling causes the current channel to shrink, altering the q(r) profile and inducing MHD activity detrimental to plasma confinement.

The problem of estimating the radiation lost from a high temperature plasma has been complicated by a lack of high Z atomic physics data. Even if such data were available, however, a complete treatment of the radiation problem would involve the solution of a large number of coupled rate equations for the density of the different charge states for each impurity element present. However, by creating a ficticious "average ion" whose charge represents the statistical average of all the possible charge states of the impurity, the problem can be reduced to the calculation of the electron shell populations P_n.

$$\dot{P}_n = S_n - L_n \qquad (2-32)$$

where S_n represents the rate at which electrons are added to the $n^{\underline{th}}$ shell by: (1) recombination (radiative, dielectronic, three-body), (2) collisional transition, and (3) radiative decay. The loss rate of electrons from the $n^{\underline{th}}$ shell, L_n, is composed of: (1) collisional transitions, (2) radiative decay to lower shells, and (3) ionization events (Figures 2-6,8).

Knowing the atomic rate coefficients for these processes, the population of each shell and their energy levels, the radiative losses due to recombination, bremsstrahlung and line

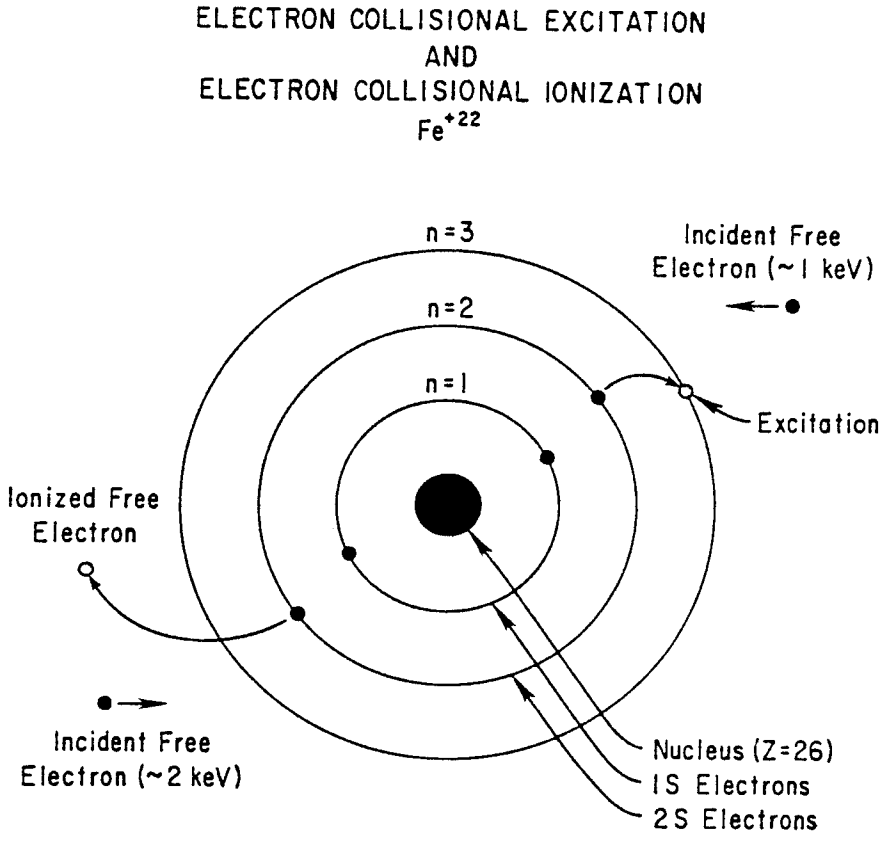

Figure (2-6) Schematic of electron/impurity collisional processes.

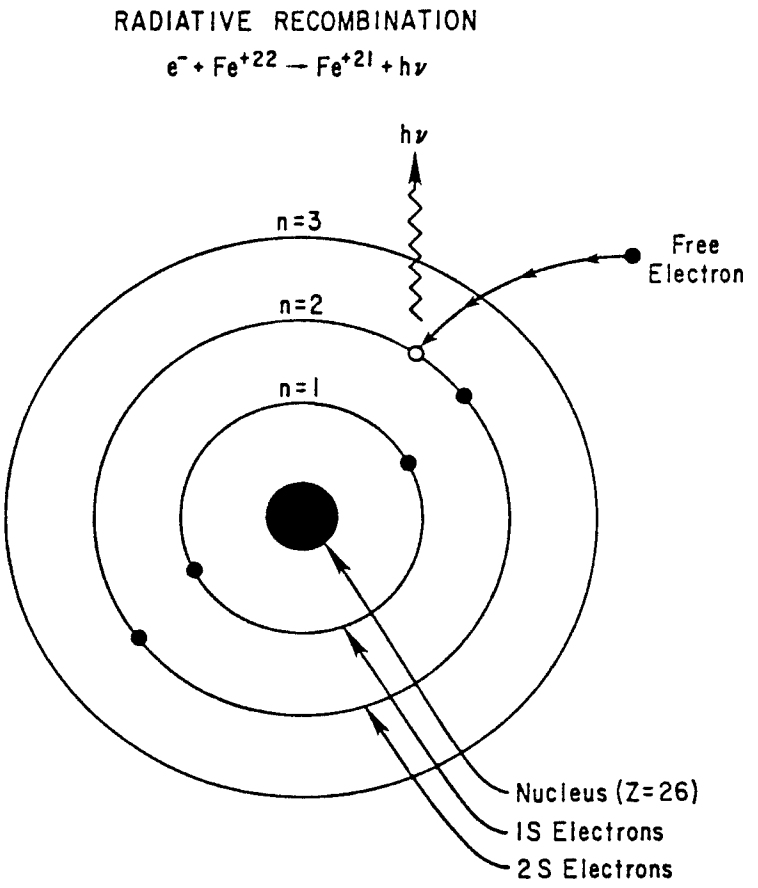

Figure (2-7) Schematic of Radiative Recombination process.

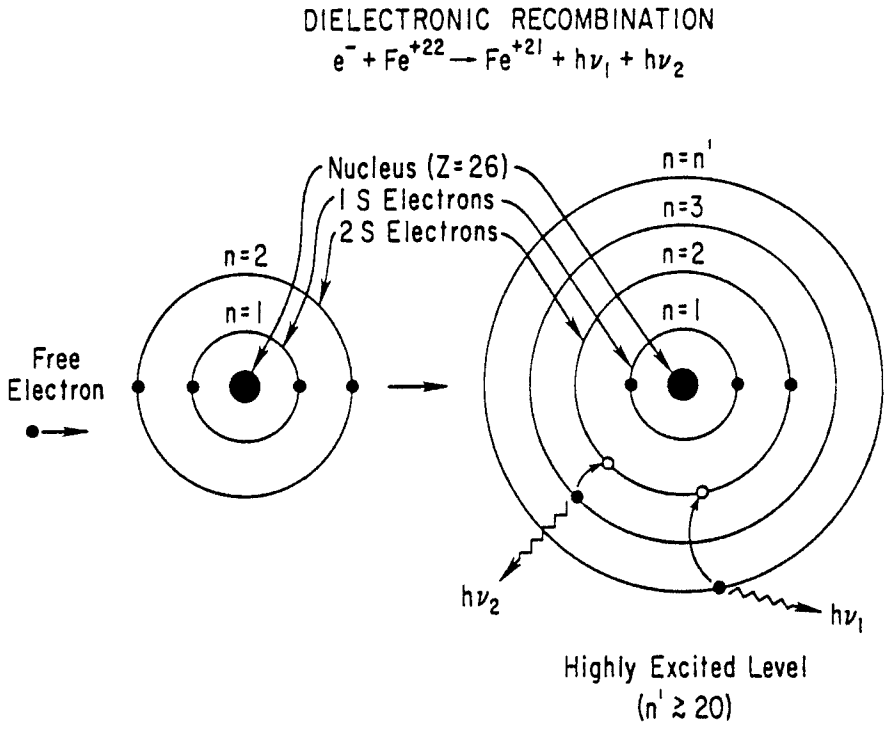

Figure (2-8) Schematic of Dielectronic Recombination processes.

transitions can be calculated. The steady-state situation, in which collisional ionization events are equal to all recombination events, is known as coronal equilibrium.

Post, et. al.[6] has developed a model for impurity radiation based upon this average-ion concept. Fits for the total radiative power per electron per impurity atom ($P_{Rad}/n_e n_z$), average $\langle Z \rangle$ and average $\langle Z^2 \rangle$ as a function of electron temperature have been tabulated. Figure (2-9) is a plot of $P_{Rad}/n_e n_z$ versus electron temperature for a number of elements based upon an average ion calculation. Figures (2-10,12) are plots of radiative losses for oxygen, molybdenum, and iron as calculated by the average ion model and other models[22-25]. The agreement is good over several decades in electron temperature.

Is the assumption of coronal equilibrium justified in a tokamak plasma? The answer depends upon the rate of impurity diffusion. From a physical point of view, coronal equilibrium is valid at a point in the plasma if in the time necessary for all the atomic processes to come to a steady-state, impurity transport to or from the point has been small. Obviously the state of a point in a plasma cannot be characterized by the <u>local</u> temperature if the impurity concentration of that point depends upon transport from neighboring zones of different temperature. Rutherford, et. al.[26] has examined this question in some detail and concludes that in PLT-like plasmas, coronal equilibrium is valid everywhere except for the extreme edge regions of the

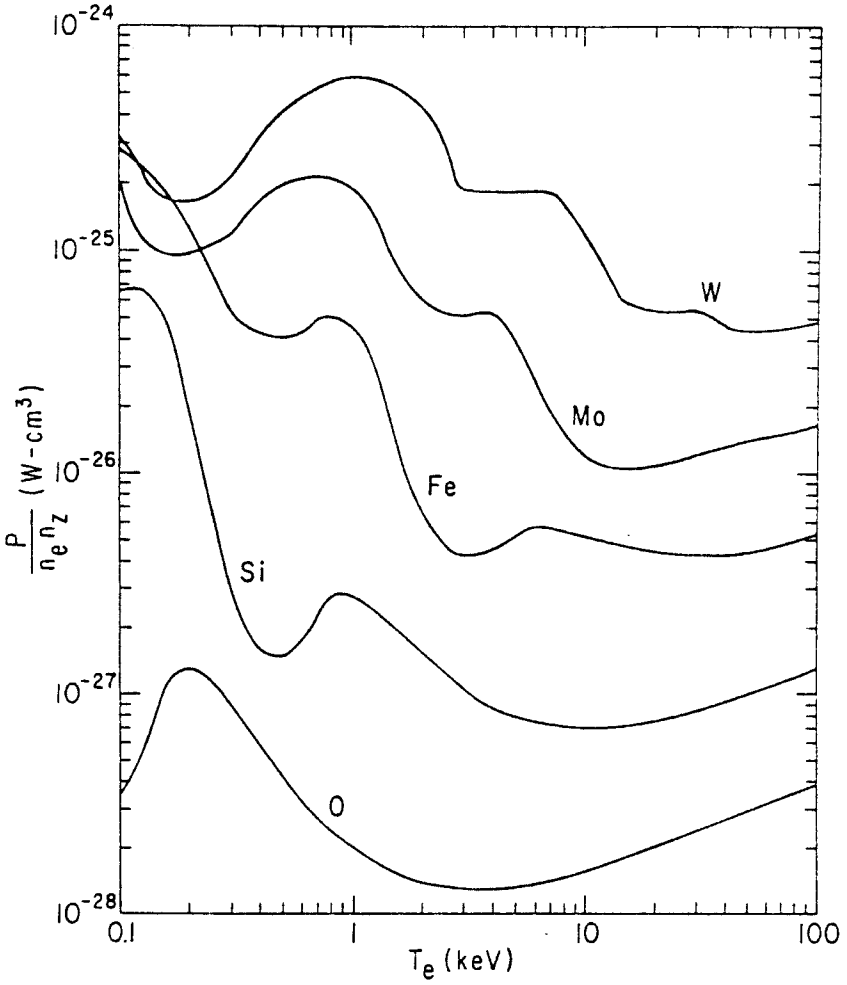

Figure (2-9) Coronal equilibrium radiated power density per electron per impurity atom as a function of electron temperature for several impurity species.

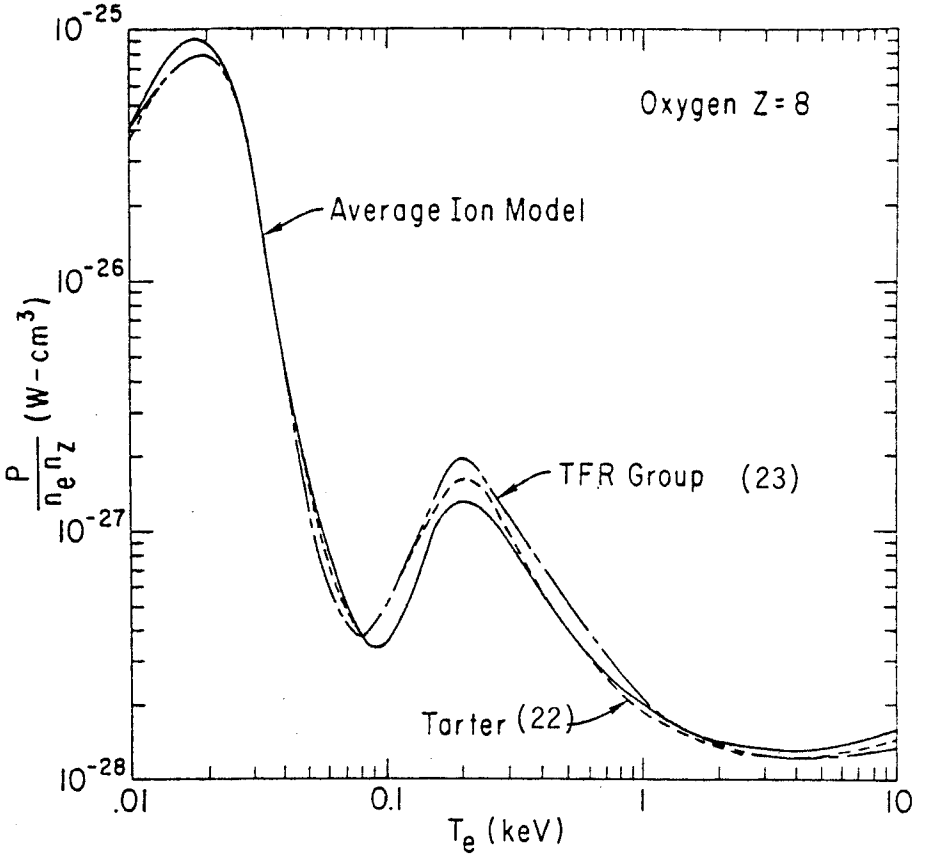

Figure (2-10) Comparison of average ion model radiative losses for oxygen with other models.

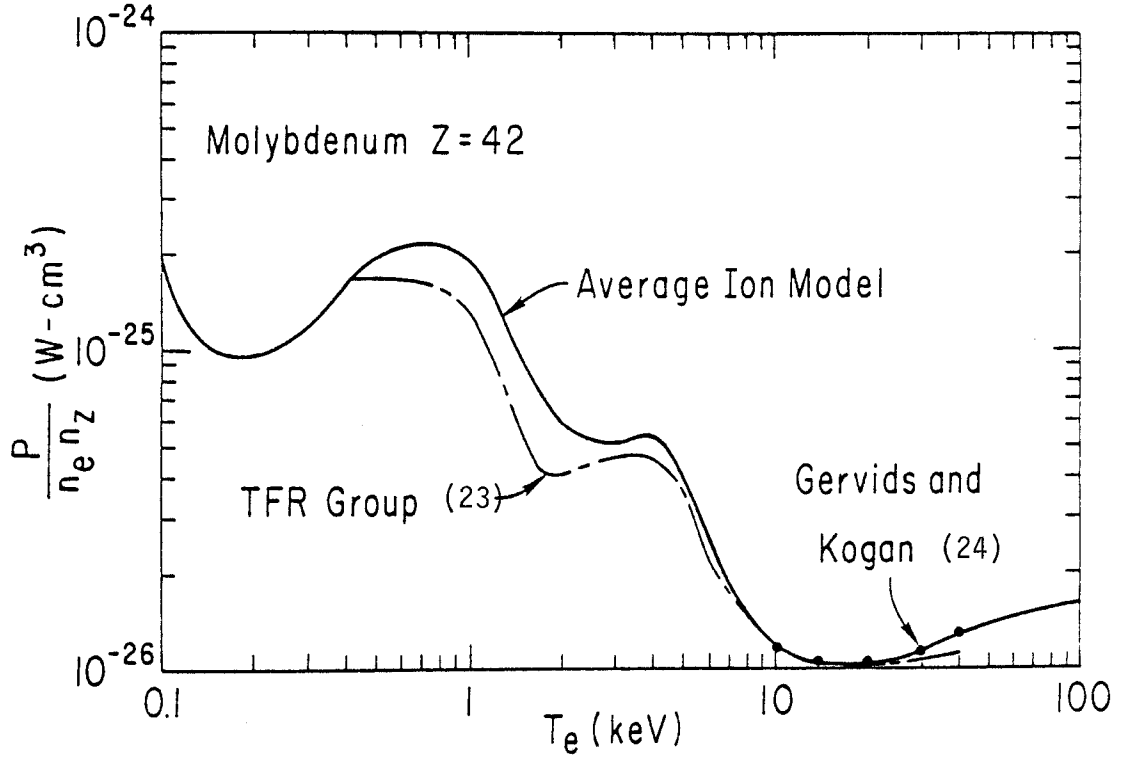

Figure (2-11) Comparison of average ion model radiative losses for molybdenum with other models.

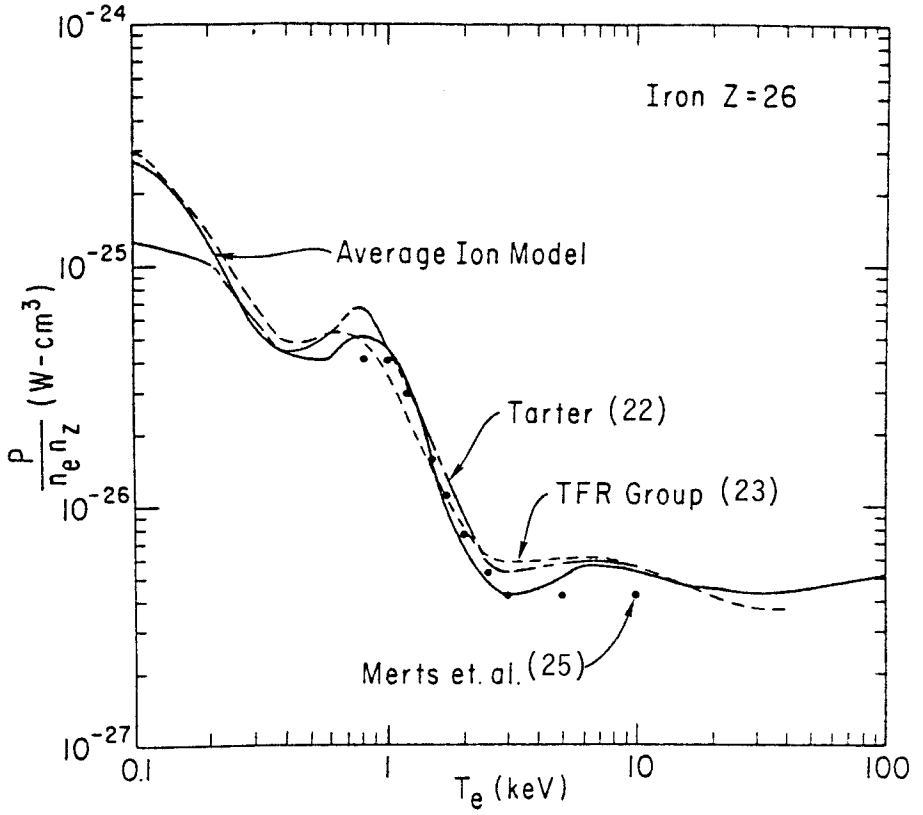

Figure (2-12) Comparison of average ion model radiative losses for iron with other models.

discharge. This is not surprising since the edge region is an area of intense recycling, a situation far from equilibrium. Consequently, the coronal model will be used to calculate the radiative losses for the bulk plasma while a non-coronal model will be employed in modelling the tokamak scrape-off zone (see Chapter 7).

2.6 Summary of Chapter 2

In this chapter the fluid equations used to model tokamak discharges have been examined. A brief review of classical and neoclassical diffusive process yielded expressions for the transport coefficients in each collisionality regime. While neoclassical theory predicts ion transport in rough agreement with experiment, a more empirical approach to electron transport was taken. Statistical analyses of electron energy confinement times indicate that the transport coefficients scale favorably with both density and temperature (i.e. $\sim(nT)^{-1}$). Having justified the neoclassical treatment of the ions and the empirical treatment of the electrons, the scalings of Ref. [7] and [18] were used to model ion and electron transport respectively.

Finally, the importance of impurities and the problems in modelling their behavior was discussed. A model for self-consistent generation of impurities will be presented in Chapter 5. The transport properties are seen to be essentially neoclassical over most of the discharge with anomalous outward

diffusion taking place near the plasma center. The effect of radiative losses on the burn dynamics and stability of the plasma was examined. A coronal equilibrium calculation based on Ref. [6] serves as the basis on which plasma radiative losses are calculated. The assumptions made in the creation of this model make estimates for radiation near the plasma edge uncertain.

In the following chapter, the numerical techniques employed in the solution of the coupled Tokamak fluid equations will be examined.

TABLE (2-1)

EMPIRICAL ELECTRON ENERGY CONFINEMENT

TIME SCALINGS IN MKS UNITS [Ref. 2-8].

Gorbunov, Mirnov and Streikov (11)	$\tau_E = 4 B_p a^2$
"Alcator" (12)	$\tau_E = 6 \times 10^{-21} \bar{n}_e a^2$
Daughney (13)	$\tau_{Ee} = 3 \times 10^{-17} \langle n_e \rangle \langle T_e \rangle^{1/2} a^2/l$
Jassby, Cohn, and Parker (14)	$\tau_E = 3 \times 10^{-21} \bar{n}_e a^2 \sqrt{q(a)}$
Hugill and Sheffield (15)	$\tau_E = 9.1 \times 10^{-16} \langle n_e \rangle^{0.61} a^{1.57} B_T^{0.88}$
Pfeiffer and Waltz (16)	$\tau_{Ee} = 9.5 \times 10^{-20} \langle n_e \rangle^{0.90} a^{0.98} R^{1.63} Z_{eff}^{0.23}$

TABLE (2-2)

EMPIRICAL TRANSPORT COEFFICIENT SCALING LAWS Ref. 2-17

SCALING	χ (cm^2/sec)	D (cm^2/sec)
ALCATOR	$5 \times 10^{17}/n_e$	(.15) χ
PLT-A	$(2.4 \times 10^{18}/n_e)\,(1 - (\frac{T_e}{.1})^3)^{-1/3}$	(.33) χ
PLT-B	$(1 \times 10^{17}/n_e)\,(1 - .4\,(\frac{r}{a})^2)^{-7/2}$	$500(\frac{r}{a})^3 + 1.25 \times 10^{17}/n_e$
	where: $n_e \rightarrow cm^{-3}$, $T_e \rightarrow$ Kev	

CHAPTER 2 REFERENCES

1. N.A. Krall and A.W. Trivelpiece, Principles of Plasma Physics, McGraw Hill (1973); see also R.D. Haxeltine, in Advances in Plasma Physics, Vol. 6, John Wiley and Sons, 1976.

2. R.D. Haxeltine, F.L. Hinton, M.N. Rosenbluth, Phys. Fluids 16, 1645 (1973).

3. W. Houlberg, Ph.D. Thesis, University of Wisconsin, p. 20 (1977).

4. K. Audenaerde, G. Emmert, M. Gordinier, J. Comp. Phys. 34, 268 (1980).

5. W.A. Houlberg, et al., Oak Ridge Report ORNL/TM-6549 (January, 1979).

6. D.E. Post, et al., Atomic Data and Nuclear Data Tables, 20, 397 (1977).

7. F.L. Hinton and T.B. Moore, Nucl. Fus. 14, 639 (1974).

8. J.M. Rawls, et al., Status of Tokamak Research, DOE Report DOE/ER-0034 (1979).

9. F.L. Hinton and R.D. Hazeltine, Rev. Mod. Phys. 48, 239 (1976).

10. A. Gondhaleker, et al., IAEA-7, Vol. 1, 199 (1979).

11. E.P. Gorbunov, et al., Nucl. Fusion 10, 43 (1970).

12. E. Apgar, et al., IAEA-6, Vol. 1, 247 (1977).

13. C. Daughney, Nucl. Fusion 15, 967 (1975).

14. D.L. Jassby, et al., Nucl. Fusion 16, 1045 (1976).

15. J. Hugill and J. Sheffield, Nucl. Fusion 18, 15 (1978).

16. W.W. Pfeiffer and R.E. Waltz, Nucl. Fusion 19, 51 (1979).

17. H. Eubank, et al., IAEA-7 Vol. 1, 167 (1979); also see Intor internal report #19.

18. See Reference #7.

19. J.B. Taylor, in Fusion Reactor Design Problems (Proc. IAEA Workshop, Culham, 1974), Nucl. Fusion Supplement 1974, IAEA, Vienna, 403 (1974).

20. T.E. Stringer, in Theory of Magnetically Confined Plasmas (Proc. Course Varenna, 1977, B. Coppi, Ed.), Pergamon Press, Oxford, 139 (1979).

21. R.V. Jensen, et al., Nuc. Sci. and Engr. 65, 282 (1978).

22. C.B. Tarter, J. Quant. Spect. Rad. Transfer 17, 531 (1977).

23. C. Brenton, et al., Nuc. Fusion 16, 891 (1976).

24. V.I. Gervids and V.I. Kogan, JETP letters 21, 150 (1975).

25. A.L. Merts, et al., Los Alamos Scientific Laboratory Report LA-6220-MS, (1976).

26. P.H. Rutherford, et al., in Proc. of the Int. Symp. on Plasma-Wall Interaction, Julich 1976, Pergamon Press, Oxford, 181 (1971).

CHAPTER 3

TOKAMAK FLUID EQUATION SOLUTION SCHEME

In this chapter the numerical techniques used to solve the coupled tokamak fluid equations (equations 2-4,9) are developed. Since large gradients in density and temperature are present near the plasma edge, a fine radial mesh is required for numerical stability and accuracy. However, near the plasma center the requirements on mesh size can be relaxed considerably. In order to speed the calculation, the numerical technique used to solve the fluid equations uses a non-uniform radial mesh. A box averaging technique is used on all diffusive terms in the equations resulting in the conservation of both particle and energy fluxes. The linearizing time expansion follows from a variable implicit technique which simultaneously preserves accuracy and minimizes time-step considerations. These techniques are based on those used in the WHIST tokamak simulation code[1]. References [2] and [3] contain detailed treatments of the following techniques.

3.1 Spatial Finite Mesh Treatment

The plasma minor radius ($0 \leq r \leq a$) is non-uniformly divided into N-1 zones and N grid points. The radial mesh geometry

is shown in Figure (3-1). Each diffusive term in the fluid equations is spatially averaged over a volume element whose sides are defined by the dotted lines in Figure (3-1). The sides are defined as the midpoint between adjacent grid points. The average value then becomes associated with the grid point contained in the volume element. This averaging process preserves both particle and energy fluxes by insuring that the fluxes leaving zone I are the fluxes entering zone I + 1.

As an example of box averaging, the density balance diffusive term becomes for the i^{th} grid point:

$$\frac{1}{r}\frac{\partial}{\partial r}(r\Gamma)\Big|_i = \int_{r^-}^{r^+} \frac{1}{r}\frac{\partial}{\partial r}(r\Gamma)\, r dr \Big/ \int_{r^-}^{r^+} r dr \qquad (3\text{-}1)$$

$$= \frac{1}{\Delta V_i}\left[(r\Gamma)^+ - (r\Gamma)^-\right] \qquad (3\text{-}2)$$

where ΔV_i is the volume of zone i, and r^{+}_{-} denotes the radial positions of the sides of the volume element. Since the fluxes, which are proportional to the transport coefficients, are needed at the box sides, a prescription for estimating off-node values for the transport coefficients is needed. Since the coefficients are known only at the node points, then:

$$D^{+}_{-} = \frac{1}{2}\left[D_i + D_{i\pm 1}\right] \qquad (3\text{-}3)$$

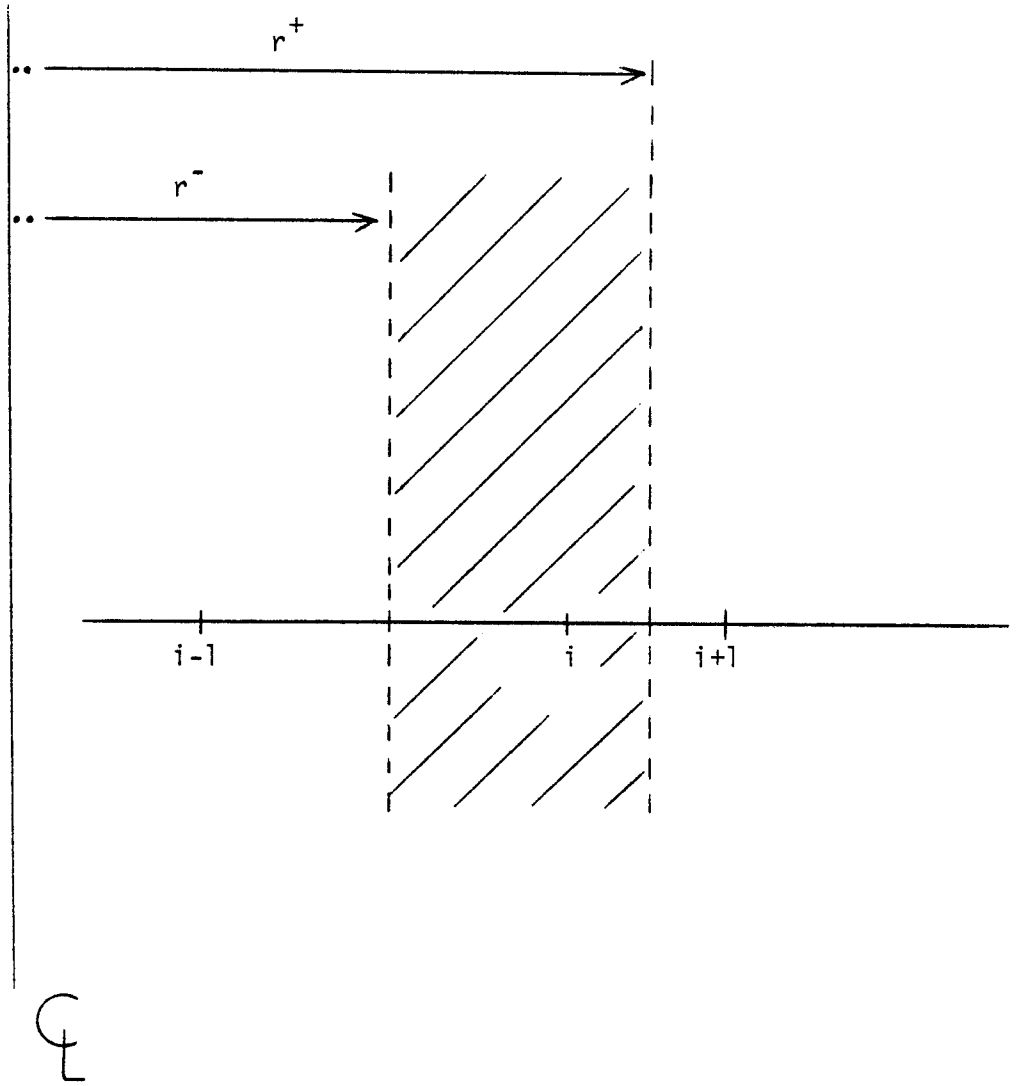

Figure (3-1) Non-uniform spatial mesh used in the one dimensional transport code.

For the volumetric terms in the fluid equations such as ohmic heating and neutral gas ionization, no spatial averaging is necessary since in each case values are known at each radial node point and are assumed to be constant across the zone.

3.2 Spatial Boundary Conditions

From symmetry considerations, all fluxes must vanish at the plasma center, i.e.:

$$\Gamma_D,\ \Gamma_T,\ \Gamma_\alpha,\ \Gamma_z,\ Q_e,\ Q_i\Big|_{r=0} = 0 \qquad (3\text{-}4)$$

At the plasma edge (r=a) defined by a separatrix or limiter tip, the boundary conditions for density and temperature (ψ) can be expressed as [4]:

$$\alpha\psi + \beta\left(\frac{\partial\psi}{\partial r}\right) = \gamma \qquad (3\text{-}5)$$

This expression yields two traditional boundary conditions for the variable :

$$\gamma = 0 \qquad \frac{1}{\psi}\left(\frac{\partial\psi}{\partial r}\right)\Big|_{r=a} \equiv \frac{-1}{\delta} \qquad (3\text{-}6)$$

$$\beta = 0 \qquad \psi\Big|_{r=a} \equiv \psi(a) \qquad (3\text{-}7)$$

Equation (3-6) represents the 'logarithmic derivative' formalism in which δ plays the role of an extrapolation distance. Equation (3-7) represents the 'fixed value' boundary condition.

How are the edge values $\psi(a)$ or the extrapolation distances δ to be determined? To date most tokamak simulation models have legislated these quantities to be time-independent parameters. This provides a numerically 'quick and dirty' way to learn about the overall gross characteristics of a plasma discharge. However, as is well known from differential equation theory, a priori boundary conditions may lead to unrealistic solutions. Fixing the boundary conditions via equations (3-6) or (3-7) effectively decouples the core plasma from the complex plasma-wall interactions taking place in the scrape-off zone ($a \leq r \leq a_{wall}$). Since the details of many tokamak discharges seem to depend more upon plasma-wall interactions than on classical plasma physics, the neglect of such processes through the legislation of fixed boundary conditions is unwise[5]. In Chapters 5 and 7 those processes which merit inclusion in a model of the scrape-off zone and the scheme employed for the dynamic evaluation of the self-consistent plasma edge boundary conditions will be described.

3.3 Time Mesh Treatment

Each term in the fluid equations is expanded in time about $t + \theta\Delta t$, where t represents the old time and θ is a stability parameter. By retaining only terms up to Δt, a linearized set of

equations for all unknown densities and temperatures at the new time is obtained. For special values of θ the time expansion technique reduces to several popular numerical schemes: $\theta = 0$ (Euler method), $\theta = 1/2$ (Crank-Nicholson), and $\theta = 1$ (pure implicit)[6]. In solving the coupled transport equations $\theta \geq 1/2$ yields good accuracy while suppressing unwanted numerical oscillations.

As an example, denote a term in the fluid equations (e.g. equation 3-2) by the variable f:

$$f = f(T_e, T_i, n_D, n_T, n_\alpha, n_z) \tag{3-8}$$

Then the time expansion becomes:

$$f^{i,n+1} \simeq f^{i,n} + \theta \sum_j \left(\frac{\partial f^{i,n}}{\partial X_j}\right) \left(\frac{\partial X_j}{\partial t}\right)\Delta t \tag{3-9}$$

where the superscripts (i) denote mesh point, (n) old time values, (n+1) new time (unknown) values, and the X_j represents the 18 independent variables:

$$X_j = (T_e^{i-1}, T_e^i, T_e^{i+1}; T_i^{i-1}, T_i^i, T_i^{i+1}; n_D^{i-1}, n_D^i, n_D^{i+1}; \tag{3-10}$$

$$n_T^{i-1}, n_T^i, n_T^{i+1}; n_\alpha^{i-1}, n_\alpha^i, n_\alpha^{i+1}; n_z^{i-1}, n_z^i, n_z^{i+1}).$$

If the term $(\partial X_j/\partial t)$ is defined as:

$$(\frac{\partial X_j}{\partial t}) \simeq \frac{X_j^{i,n+1} - X_j^{i,n}}{\Delta t} \qquad (3\text{-}11)$$

then the completed expansion yields a system of coupled linear equations for the unknown densities and temperatures $X_j^{i,n+1}$ at each node point i at the new time[7].

All known quantities are placed in the right hand side of the equations while all the unknowns (with their known coefficients $\propto (\frac{\partial f^{i,n}}{\partial X_j})$) are placed on the left hand side. This system of equations can be expressed in matrix form as:

$$\bar{\bar{A}} \cdot \vec{X}^{n+1} = \vec{B} \quad ; \quad \bar{\bar{A}}, \vec{B} \text{ known} \qquad (3\text{-}12)$$

Inversion of the matrix of coefficients $\bar{\bar{A}}$ yields the new densities and temperatures at each point in the plasma. If these values are 'unphysical', i.e. < 0, the timestep is reduced, the coefficient matrix is re-evaluated and an inversion yields the new values. This process is repeated until physically reasonable results are obtained.

3.4 Summary of Chapter 3

The numerical techniques used to solve the coupled tokamak fluid equations have been examined. Spatial effects involve the use of a non-uniform mesh and the box averaging of all diffusive

terms. The time expansion follows a variable implicit technique which linearizes the equations and permits a matrix solution of the system at each timestep. The incorporation of a stability parameter allows the calculations to proceed without the generation of unwanted numerical oscillations.

In the following chapter, the problem of neutral transport in tokamaks will be explored by employing an algorithm suitable for inclusion in tokamak simulation codes. The scheme is then generalized to treat two specie neutral transport.

CHAPTER 3 REFERENCES

1. W. Houlberg, R.W. Conn, Nuc. Sci. and Engr. 64, 141 (1977).

2. Reference (2-3).

3. A.T. Mense, Ph.D. Thesis, University of Wisconsin, 172 (1977).

4. P. Morse and H. Feshback, Methods of Theoretical Physics (McGraw Hill, N.Y.), Sec. 6-2.

5. A.T. Mense, G.A. Emmert, Oak Ridge Report ORNL/TM-6279 (April, 1978).

6. G. Dahlquist, et al., Numerical Methods (Prentice-Hall, 1974).

7. M. Widner, R. Dory, Oak Ridge Report ORNL/TM-3498 (1971).

CHAPTER 4

NEUTRAL ATOM TRANSPORT IN TOKAMAK PLASMAS

4.1 Motivation

It is well-known that neutral hydrogenic atoms play an important role in the evolution of tokamak discharges. Neutral atoms affect both the particle and energy balance of the plasma and, by wall bombardment, can erode the chamber wall as well as provide a mechanism for the generation of impurities which enter the plasma. Consequently, codes which calculate the transport of neutral atoms are generally included as routines in tokamak simulation codes[1,2]. Furthermore, the energetic neutral particles emerging from the plasma are often used as a diagnostic of the plasma ion temperature and the quantity and energy of these neutrals are of interest to surface physicists.

Greenspan[3] pointed out that neutral particle transport is conceptually the same as photon or neutron transport. Consequently, neutronics codes, such as ANISN, can easily be adapted to neutral atom transport. Several calculations of this type have been reported [3-7]. Unfortunately such codes are bulky and slow since they are designed to treat complicated neutron interactions; the neutral atom processes in a plasma are rather simple in comparison. This simplicity has led to the development of

special purpose neutral transport routines which are better suited for inclusion in tokamak simulation codes. Some of these special purpose routines have been discussed by Hogan[2] in his review. The role then, of codes based on neutron transport methods has been to provide an accuracy standard for the special purpose routines[6,7].

A special purpose neutral transport routine (developed by G.A. Emmert, K. Audenaerde, and M. Gordinier) which is exceptionally compact and fast is presented here. This routine, which is designed for inclusion in tokamak simulation codes, is based on an integral equation for neutral particle transport. The geometry is that of a finite thickness plasma slab with a source of neutral atoms at the plasma edge. For large tokamaks in which the neutral atom mean free path is much less than the minor radius, this assumption of slab geometry is sufficient for wall-originated neutrals. For neutrals originating near the center of the device (e.g., from beam injection) or for "optically thin" plasmas cylindrical effects are more important. In Section (4.2) the integral equation on which the neutral transport routine is based is formulated. This equation is then transformed in Section (4.3) into a finite dimensional matrix equation in a manner which conserves particles and energy. The dimensionality of the matrix equation is the number of mesh points over which neutral particle transport is to be calculated. In Section (4.4) a comparison of this neutral code with the ANISN calculation of Gilligan

et al.[7] and with results using another neutral atom transport routine (FASLAB), developed at Oak Ridge[8] are presented.

In Sections (4.5) - (4.8) generalization of the one specie neutral transport algorithm to a two specie model is presented. In Section (4.9) results obtained from the two species neutral transport model are presented.

4.2 The Transport Integral Equation

Consider a slab of width d filled with plasma as shown in Figure (4-1). The plasma density and temperatures are functions of x, the coordinate normal to the slab face. Divide the neutral particles into two classes: those emitted from the wall at x = 0, and those born inside the plasma by charge exchange. The latter are assumed to be born isotropically and with a single energy E, defined by the ion temperature T_i at the place of birth.

$$E = \frac{1}{2} mv^2 = \frac{3}{2} k_B T_i(x). \qquad (4\text{-}1)$$

The isotropic assumption has been shown to be adequate in ANISN calculations[7]; the monoenergetic assumption can only be justified a posteriori, i.e. by comparison to multi-group calculations. This is done in Section (4.4). The neutral particles emitted by the wall are divided into discrete energy groups and have a specified angular distribution with respect to the x-axis. The boundary condition at x = d is perfect absorption.

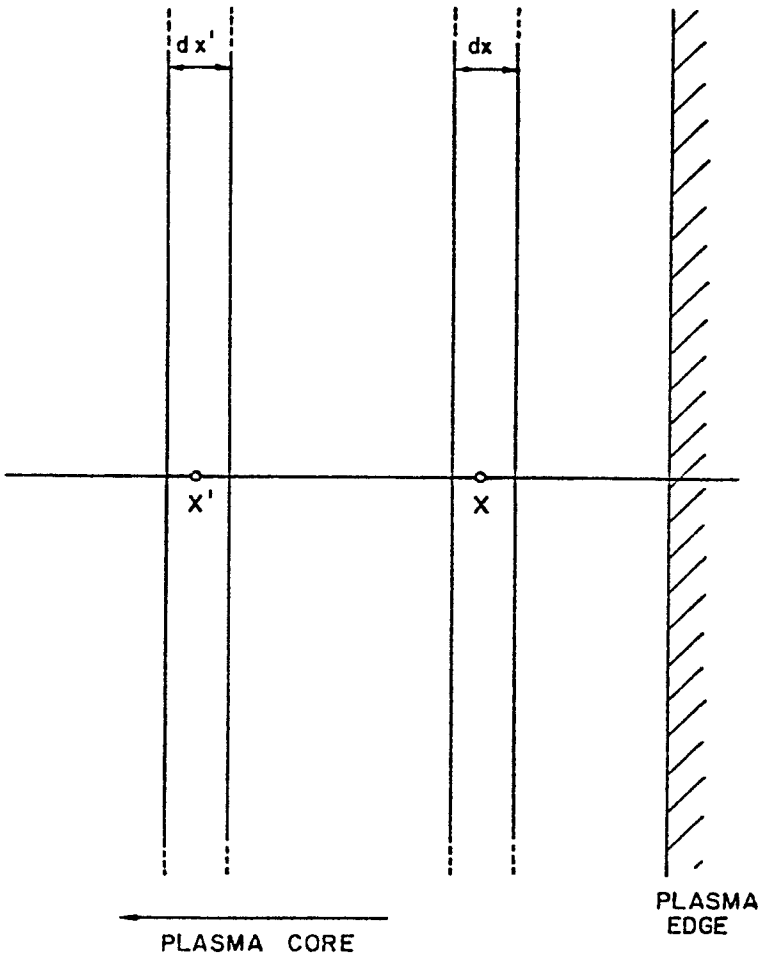

Figure (4-1) Slab geometry for neutral transport.

Consider first the wall-originated particles. Let $\eta(\theta)$ be the number emitted per unit wall area per unit time per unit solid angle in the direction θ, in a single energy group with energy $E_o = \frac{1}{2} mv_o^2$. The number of particles traversing a differential area da (normal to the x-axis) per unit time due to source points in an annular ring of width dr and radius r, as shown in Figure (4-2), is

$$\frac{dN}{dt} = \eta(\theta)\ 2\pi\ rdr\ d\Omega\ \ e^{-\int \frac{\mu_o(x',E_o)}{v_o} ds'} \qquad (4\text{-}2)$$

where $d\Omega = da\ \cos\theta/s^2$. The exponential factor is due to absorption along the path length s, and

$$\mu_o(x,E_o) = n_e(x) \langle\sigma v\rangle_e + n_i(x) [\langle\sigma v\rangle_i + \langle\sigma v\rangle_{cx}]. \qquad (4\text{-}3)$$

Since $x = s\cos\theta$:

$$\int_o^s \frac{\mu_o(x',E_o)}{v_o} ds' = \frac{1}{\cos\theta} \int_o^x \frac{\mu_o(x',E_o)dx'}{v_o} = \frac{\beta_o(x)}{\cos\theta}\ , \qquad (4\text{-}4)$$

$\beta_o(x)$ being the optical depth on axis.

To obtain the neutral particle flux Γ traversing da, we integrate (2) over r and divide by da;

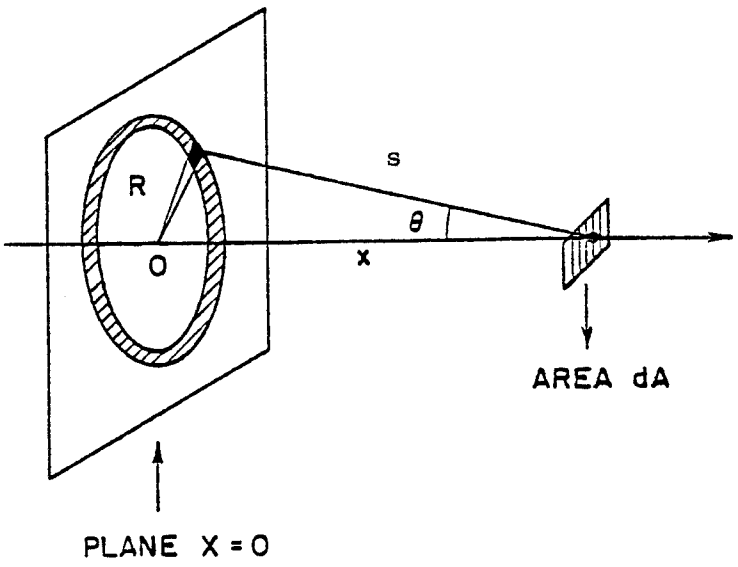

Figure (4-2) Source annulus for neutral particle transport.

$$\Gamma = 2\pi \int_0^\infty r dr \, \frac{n(\theta)\cos\theta}{s^2} \, e^{-\beta_o(x)/\cos\theta}. \tag{4-5}$$

$u = 1/\cos\theta.$ $$\Gamma = 2\pi \int_1^\infty du \, \frac{n(\theta(u))}{u^2} \, e^{-\beta_o u} \tag{4-6}$$

Letting the source function $\eta(\theta)$ be isotropic ($\eta(\theta) = \eta$), Then

$$\Gamma(x) = \Gamma_o \, E_2(\beta(x)). \tag{4-7}$$

For the second case, consider a $\cos\theta$ source ($\eta(\theta) = \eta_1 \cos\theta$)

$$\Gamma(x) = 2\Gamma_o \, E_3(\beta(x)). \tag{4-8}$$

The absorption rate per unit volume in the plasma is

$$A(x) = \frac{d\Gamma}{dx} \tag{4-9}$$

and the fraction of the absorption rate due to charge exchange is $n_i \langle\sigma v\rangle_{cx}/\mu(x,E_o)$. Each charge exchange event produces a first generation neutral particle in the plasma. Thus,

$$S_1(x) = \frac{n_i(x)\langle\sigma v\rangle_{cx}}{\mu_o(x,E_o)} A(x) \tag{4-10}$$

is the source rate for first generation internally born neutral particles. This expression can be rewritten as:

$$S_1(x) = 2 \frac{n_i(x)\langle\sigma v\rangle_{cx}}{v_o} E_2(\beta_o(x))\ \Gamma_o. \qquad (4\text{-}11)$$

To obtain the total source rate for first generation neutrals, write equation (4-10) for each energy group and sum over groups.

Consider now the internally born neutral particles. Let $S_p(x)$ be the source function for the p'th generation. At each possible birth point x, they are assumed to be born isotropically and with a single energy $E(x) = \frac{3}{2} k_B T_i(x) = \frac{1}{2} mv^2(x)$. Consider a slab of thickness dx' at x' (See Fig. (4-1)); the flux of particles at $x(x > x')$ due to the source in the slab at x' is

$$d\Gamma_p^r(x) = \frac{1}{2} S_p(x')\ E_2(\beta(x', x))dx'. \qquad (4\text{-}12)$$

The r superscript denotes that these particles are travelling to the right at x and the $\frac{1}{2}$ arises because only half of the particles born at x' go to the right (i.e., $v_x > 0$). Also:

$$\beta(x', x) = \left| \int_{x'}^{x} \frac{\mu(x'', x')}{v(x')} dx'' \right| \qquad (4\text{-}13)$$

$$\mu(x'', x') = n_e(x'') \langle\sigma v\rangle_e + n_i(x'') [\langle\sigma v\rangle_i + \langle\sigma v\rangle_{cx}].$$

Now differentiate $d\Gamma_p^r(x)$ with respect to x to obtain the absorption rate at x due to the particles born in dx' and

multiply this by $n_i(x)\langle\sigma v\rangle_{cx}\,\mu^{-1}$ to get the charge exchange rate at x. This gives the contribution to the source rate at x of the (p + 1)'th generation due to the p'th generation at x'. A similar expression for the particles travelling to the left at x also exists; they were born at x' > x. The total source rate S_{p+1} is then found by integrating over x':

$$S_{p+1}(x) = \int_0^d dx'\, K(x, x')\, S_p(x'). \qquad (4\text{-}14)$$

where the kernel K(x, x') is given by

$$K(x, x') = \frac{1}{2}\,\frac{n_i(x)\langle\sigma v\rangle_{cx}}{v(x')}\,E_1(\beta(x', x)) \qquad (4\text{-}15)$$

The interesting property of (4-14) and (4-15) is that the kernel is independent of the generation. It is convenient to write (4-14) symbolically as

$$S_{p+1}(x) = K\,S_p(x), \qquad (4\text{-}16)$$

where K is the integral operator whose kernel is given by (4-15). The total charge exchange rate per unit volume S(x) is found by summing over generations;

$$S(x) = \sum_{p=1}^{\infty} S_p(x)$$

$$= (I + K + K^2 + K^3 + \ldots)\, S_1(x)$$

$$= \frac{1}{I - K}\, S_1(x) \qquad (4\text{-}17)$$

using (4-16) recursively. This expression can be rewritten as:

$$S(x) = S_1(x) + K\, S(x) \qquad (4\text{-}18)$$

which, when written out explicitly, is

$$S(x) = S_1(x) + \int_0^d dx'\, K(x, x')\, S(x'). \qquad (4\text{-}19)$$

This is an integral equation determining the total charge exchange rate per unit volume S(x) in the plasma; the inhomogeneous term $S_1(x)$ is given by equation (4-11). Internal isotropic sources of neutral atoms with energy E are easily included; their source strength is merely added to $S_1(x)$. From the function S(x) one can determine all other quantities of interest.

For example, the ionization rate due to electron impact is:

$$S_e(x) = \int_0^d dx'\, \frac{n_e(x)\langle\sigma v\rangle_e}{n_i(x)\langle\sigma v\rangle_{cx}}\, K(x, x')\, S(x') \qquad (4\text{-}20)$$

$$+ \frac{n_e(x)\langle\sigma v\rangle_e}{n_i(x)\langle\sigma v\rangle_{cx}}\, S_1(x).$$

the energy loss rate due to charge exchange is

$$W_{cx}(x) = \int_o^d dx' \, \frac{3}{2} k_B [T_i(x) - T_i(x')] \, K(x, x') \, S(x') \qquad (4\text{-}21)$$

$$+ [\frac{3}{2} k_B T_i(x) - E_o] \, S_1(x),$$

and the neutral particle flux incident on the wall is

$$\Gamma_w = \int_o^d dx \, \frac{1}{2} S(x) \, E_2(\beta(o,x)) \qquad (4\text{-}22)$$

The integrand in (4-22) has an interesting significance. It is the source rate of particles that reach the wall without further collision. From this source rate and the temperature profile, one can construct the energy distribution of the neutral particles incident on the wall. This will be discussed further in the next section. The neutral particle density profile in the plasma is most easily found from the electron impact ionization rate. Since $\langle \sigma v \rangle_e$ is essentially independent of neutral particle energy but is a function of $T_e(x)$, we can write

$$S_e(x) = n_i(x) \, n_o(x) \, \langle \sigma v \rangle_e . \qquad (4\text{-}23)$$

Hence the neutral particle density $n_o(x)$ can be obtained from (4-20) and (4-23).

4.3 The Discretized System

In this section, the reduction of the integral equation (4-19) to a finite dimensional matrix equation which is then solved by a single matrix inversion is achieved.

Consider a set of mesh points j with coordinates $x_j (j = 1,N)$ and associated zones, as shown in Figure (4-3). The boundaries between the zones are midway between mesh points (which may be non-uniformly spaced). The zone widths are $\Delta_j = (x_{j+1} - x_{j-1})/2$. This is the mesh-zone configuration used in the space-time code for the plasma transport equations. The required plasma data is given at each of the mesh points j.

The reduction scheme consists of calculating, for a given generation, the flux entering and leaving each zone. This difference represents the net absorption in that zone; a certain fraction of it is due to charge exchange and represents the source for the next generation. This source is assumed to be concentrated at the meshpoints.

Consider first the neutral particles streaming from the wall. The optical depth to the left face of the j'th zone is

$$\beta_j^o = \sum_{i=1}^{j-1} \frac{\mu(x_i, E_o)}{v_o} \Delta_i . \qquad (4-24)$$

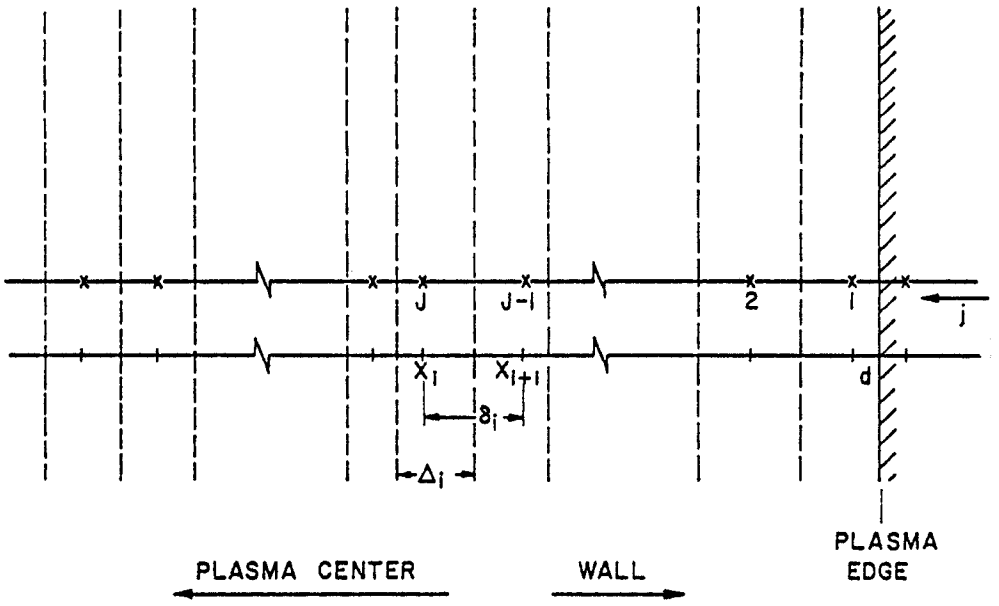

Figure (4-3) Discretized spatial grid for neutral transport.

The absorption rate per unit volume in the j'th zone is

$$A_j = 2\Gamma_o \frac{E_3(\beta_j^o) - E_3(\beta_{j+1}^o)}{\Delta_j} . \qquad (4\text{-}25)$$

Hence the source for the first generation of internally born neutral particles is

$$S_1(x_j) = 2\Gamma_o \frac{n_i(x_j)\langle\sigma v\rangle_{cx}}{\mu(x_j,E_o)\Delta_j} [E_3(\beta_j^o) - E_3(\beta_{j+1}^o)]. \qquad (4\text{-}26)$$

A similar procedure for the internally born neutral particles is followed. In this case the optical depths are calculated between the k'th meshpoint and the two faces of the j'th zone. Introducing the shorthand notation $v_j = v(x_j)$, $\mu_{jk} = \mu(x_j,x_k)$, then:

$$v_k \beta_{jk}^- = \sum_{i=k+1}^{j-1} \mu_{ik}\Delta_i + \frac{1}{2}\mu_{kk}(x_{k+1} - x_k) \qquad (4\text{-}27)$$

if $j > k$, and

if $k > j$.
$$v_k \beta_{jk}^- = \sum_{i=j+1}^{k-1} \mu_{ik}\Delta_i + \frac{1}{2}\mu_{kk}(x_k - x_{k-1}) \qquad (4\text{-}28)$$

also define:
$$\beta_{jk}^+ = \beta_{jk}^- + \frac{\mu_{jk}\Delta_j}{v_k}. \qquad (4\text{-}29)$$

Clearly β_{jk}^- is the optical depth to the near face of the j'th zone and β_{jk}^+ is the optical depth to the far face.

The absorption rate in the j'th zone due to the source in the k'th zone is

$$A_{jk} = \frac{1}{2} \frac{S_p(x_j)\Delta_k}{\Delta_j} \left(E_2(\beta_{jk}^-) - E_2(\beta_{jk}^+)\right) \qquad (4\text{-}30)$$

for $k \neq j$. For $k = j$, the flux out the right face is

$$\Gamma_r = \frac{1}{2} S_p(x_j)\ \Delta_j\ E_2(\beta_j^r), \qquad (4\text{-}31)$$

and out the left face is

$$\Gamma_\ell = \frac{1}{2} S_p(x_j)\ \Delta_j\ E_2(\beta_j^\ell), \qquad (4\text{-}32)$$

where

$$\beta_j^r = \frac{\mu_{jj}(x_{j+1} - x_j)}{2v_j} \qquad (4\text{-}33)$$

$$\beta_j^\ell = \frac{\mu_{jj}(x_j - x_{j-1})}{2v_j} \qquad (4\text{-}34)$$

The absorption rate in the j'th zone due to the particles born in the same zone is

$$A_{jj} = S_p(x_j) - \frac{(\Gamma_r + \Gamma_\ell)}{\Delta_j}, \qquad (4\text{-}35)$$

which becomes

$$A_{jj} = \frac{1}{2} S_p(x_j)\ [2 - E_2(\beta_j^r) - E_2(\beta_j^\ell)].$$

Multiplying the absorption rate A_{jk} by the probability that the absorption was due to charge exchange and summing over the source slabs k results in the source for the next generation. This yields:

$$S_{p+1}(x_j) = \sum_k K_{jk} S_p(x_k), \tag{4-36}$$

where:

$$K_{jk} = \frac{1}{2} \frac{n_i(x_j)\langle\sigma v\rangle_{cx}}{\mu_{jk}} \frac{\Delta_k}{\Delta_j} [E_2(\beta^-_{jk}) - E_2(\beta^+_{jk})] \tag{4-37}$$

if $j \neq k$, and

$$K_{jj} = \frac{1}{2} \frac{n_i(x_j)\langle\sigma v\rangle_{cx}}{\mu_{jj}} [2 - E_2(\beta^r_j) - E_2(\beta^\ell_j)] \tag{4-38}$$

if $j = k$.

The matrix K_{jk} is the discretized form of the integral operator K defined in equation (4-15). The neutral particle code SPUDNUT calculates the vector $\vec{S}_1$ (determined by the wall-originated particles and internal sources, if any), the matrix $\vec{\vec{K}}$ and then calculates $\vec{S}$ by computing the inverse $(\vec{\vec{I}} - \vec{\vec{K}})^{-1}$. The inversion routine used is due to Crout[9]. The particle source and energy sink terms needed by the plasma transport equations are then calculated by matrix operators using $\vec{S}$.

In the same way as in the continuous system, a summation over generations yields the total charge exchange rate per unit

volume. This is determined by the matrix equation

$$\vec{S} = \vec{S}_1 + \vec{\vec{K}} \cdot \vec{S}, \tag{4-39}$$

which has the solution

$$\vec{S} = (\vec{\vec{I}} - \vec{\vec{K}})^{-1} \cdot \vec{S}_1 \tag{4-40}$$

For completeness, the matrix equations for these source and sink terms are listed here:

Electron impact ionization rate:

$$S_e(x_j) = \sum_k \frac{n_e(x_j)\langle\sigma v\rangle_e}{n_i(x_j)\langle\sigma v\rangle_{cx}} K_{jk} S(x_k) + \frac{n_e(x_j)\langle\sigma v\rangle_e}{n_i(x_j)\langle\sigma v\rangle_{cx}} S_1(x_j). \tag{4-41}$$

Ion impact ionization rate:

$$S_i(x_j) = \sum_k \frac{n_i(x_j)\langle\sigma v\rangle_i}{n_i(x_j)\langle\sigma v\rangle_{cx}} K_{jk} S(x_k) + \frac{n_i(x_j)\langle\sigma v\rangle_i}{n_i(x_j)\langle\sigma v\rangle_{cx}} S_1(x_j). \tag{4-42}$$

Energy loss rate from the ions due to charge exchange:

$$W_{cx}(x_j) = \frac{3}{2} k_B \sum_m [T_i(x_j) - T_i(x_m)] K_{jm} S(x_m) \tag{4-43}$$

$$+ [\frac{3}{2} k_B T_i(x_j) - E_o] S_1(x_j).$$

Kinetic energy deposition in the ions due to ionization:

$$W_i(x_j) = \sum_k \frac{n_e(x_j)\langle\sigma v\rangle_e + n_i(x_j)\langle\sigma v\rangle_i}{n_i(x_j)\langle\sigma v\rangle_{cx}} \cdot \frac{3}{2} k_B T_i(x_k)\, K_{jk}\, S(x_k) \tag{4-44}$$

$$+ \frac{n_e(x_j)\langle\sigma v\rangle_e + n_i(x_j)\langle\sigma v\rangle_i}{n_i(x_j)\langle\sigma v\rangle_{cx}} \cdot E_o\, S_1(x_j).$$

The flux of energetic neutrals incident on the wall is calculated using the discretized from of equation (4-22):

$$\Gamma_w = \frac{1}{2} \sum_k S(x_k)\, E_2(\beta(0, x_k)), \tag{4-45}$$

where

$$\beta(0, x_k) = \sum_{i=1}^{k-1} \frac{\mu_{ik}\, \Delta_i}{v_k} + \frac{\mu_{kk}(x_k - x_{k-1})}{2v_k}. \tag{4-46}$$

The energy distribution of the particles hitting the wall is obtained by noting that the particles belonging to each term in the summation in equation (4-45) have an energy $E_k = \frac{3}{2} k_B T_i(x_k)$.

Reflection of energetic particles at the wall is incorporated in the routine by introducing an energy dependent reflection coefficient and a prescription for dividing the reflected particles into the various energy groups comprising the flux Γ_o of particles entering the plasma. The outgoing fluxes are then calculated iteratively until the results converge.

4.4 Comparative Calculations

Multi-group ANISN calculations of the neutral particle transport were reported by Gilligan[7] for the TFTR plasma. For these calculations the plasma density and temperature were taken to be

$$n_e(r) = n_i(r) = n_o(1 - (r/a)^3) + n_B,$$
$$T_e(r) = T_i(r) = T_o(1-(r/a)^2) + T_B. \qquad (4\text{-}47)$$

where $n_o = 4 \times 10^{13}$ cm^{-3}, $n_B = 1 \times 10^{13}$ cm^{-3}, $T_o = 9950$ eV, $T_B = 50$ eV. Here r is the radial coordinate and a is the wall radius. The coordinate x used in Sections (4.2) and (4.3) is $x = a-r$. The density, n_c, of the neutral particles incident on the plasma at the edge was taken to be 5×10^9 cm^{-3} and their energy, E_c, was 3 eV. (The neutral particle flux into the plasma is given by $\Gamma = .5\, n_c \bar{v}$, where $\bar{v} = \sqrt{2E_c/m}$). Thirty-one energy groups were used in the multi-group calculations to which results from SPUDNUT will be compared.

Using the parameters above, the same calculation was done using SPUDNUT and FASLAB. The neutral density profile obtained by each of the routines is shown in Figure (4-4). As can be seen, significant differences in the neutral density, as calculated by the three different codes, appear only after the neutral density has been attenuated by more than two orders of magnitude. This difference is not generally significant in tokamak simulation

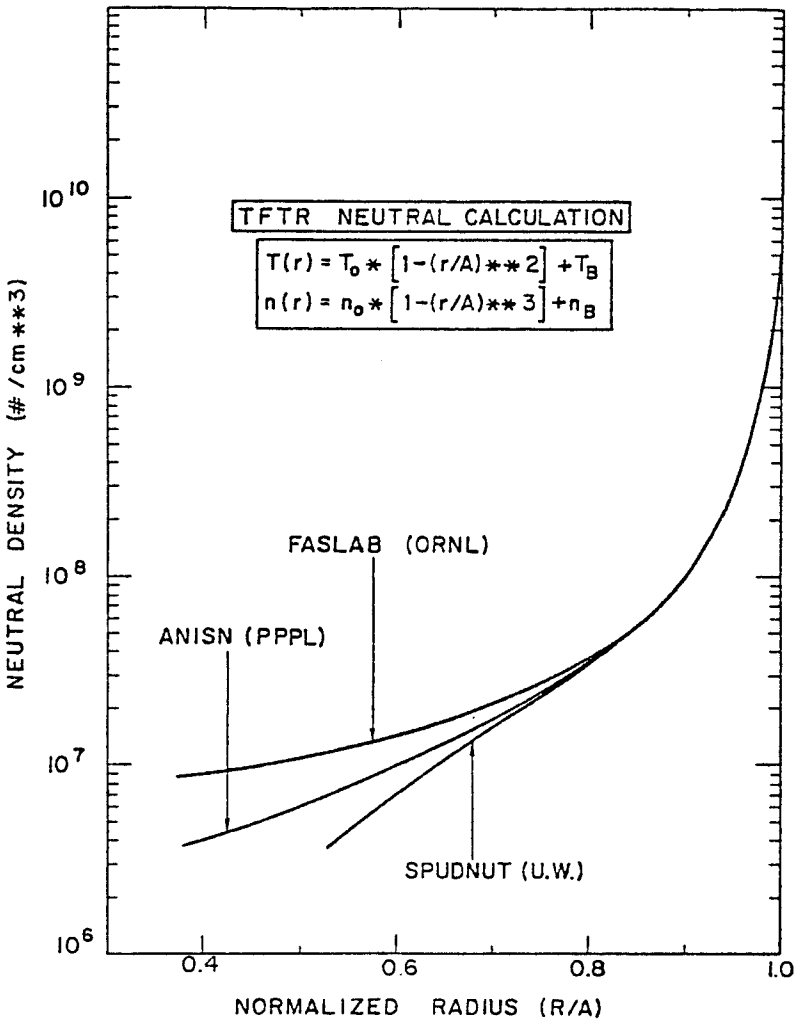

Figure (4-4) Neutral density as a function of normalized plasma radius for TFTR using ANISN, FASLAB, and SPUDNUT codes.

codes; the interesting region is the first two orders of magnitude. The energetic neutral particles reaching the wall are born primarily in this region. Furthermore, the neutral particle effects in the plasma transport equations are significant only in this zone (i.e., near the edge of the plasma). The energy spectrum of the energetic neutral particle flux incident on the wall is shown in Figure (4-5) for the ANISN and SPUDNUT calculations; again the agreement is good. One conclusion from this comparison is that the assumption of the charge-exchange neutrals being born (locally) monoenergetically is reasonable.

It should be noted that the ANISN calculation was done in cylindrical geometry, whereas SPUDNUT uses a slab with a source on one side, and FASLAB uses a symmetric slab (source on both sides and symmetry about the midplane). The ANISN calculation took 75 sec on an IBM 360/91[7], compared to 1.35 sec for FASLAB and .06 sec for SPUDNUT, both on the CDC-7600. Twenty zones were used for the SPUDNUT calculation; the computational time scales as the square of the number of zones. The most time consuming step is the calculation of the reaction rates needed in the matrix K_{jk}. Simpler routines for the reaction rates would substantially reduce the computation time.

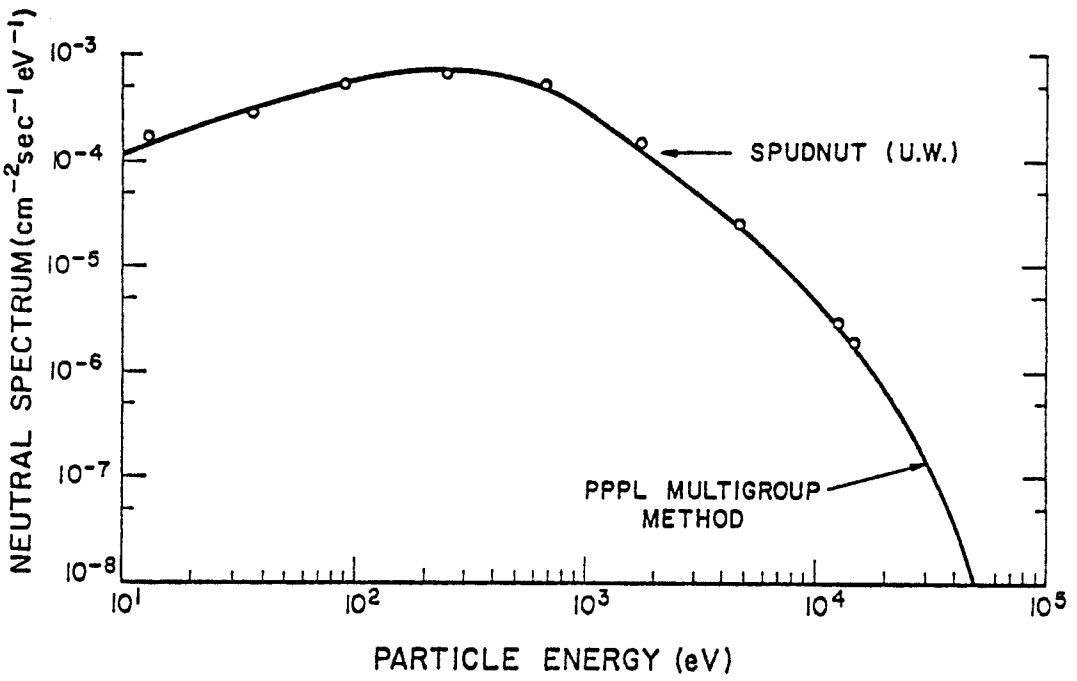

Figure (4-5) Charge exchange energy spectrum of TFTR evaluated using ANISN and SPUDNUT codes.

4.5 Two Species Generalization

In the preceding sections, an exceptionally fast and accurate algorithm for one specie neutral transport in a tokamak plasma was developed. This package is suitable for inclusion in a one dimensional radial transport code in which deuterium and tritium are lumped together as a single 'ion'. However, many second-generation transport codes now treat deuterium and tritium as seperate species. With this motivation, the generalization of the one specie algorithm to perform two specie neutral transport is presented.

4.6 Reaction Channels

The treatment of deuterium and tritium as two distinct species requires following ten reaction channels which model all the inter and intra specie interactions (Table 4-1). This is in contrast to the one specie model in which only three reactions were followed. These additional atomic reactions have the following consequence. Since the bulk of the calculation involves evaluation of reaction rates, the two specie version runs about $(10/3) \underset{\sim}{} 3.3$ times slower than the previous one specie model. However, practically speaking, the model is still substantially faster than the usual algorithms.

4.7 Coupled Integral Transport Equations

Since a given neutral atom can now be attenuated in the plasma by electrons, deuterons and tritons, the optical depths, μ, become specie dependent and are redefined as:

(4-48)

$$\mu^D \equiv n_e \langle\sigma v\rangle_e^{De} + n_D \left[\langle\sigma v\rangle_{cx}^{DD} + \langle\sigma v\rangle_i^{DD}\right] + n_T \left[\langle\sigma v\rangle_{cx}^{DT} + \langle\sigma v\rangle_i^{DT}\right]$$

$$\mu^T \equiv n_e \langle\sigma v\rangle_e^{Te} + n_D \left[\langle\sigma v\rangle_{cx}^{TD} + \langle\sigma v\rangle_i^{TD}\right] + n_T \left[\langle\sigma v\rangle_{cx}^{TT} + \langle\sigma v\rangle_i^{TT}\right].$$

By analogy to the single specie integral equation for the charge-exchange source rate S(x) (equation 4-19), the charge-exchange source rates for deuterium and tritium can be expressed as:

(4-49)

$$S^D(x) = S_1^D(x) + \int_o^d \left[K_{DD}(x, x')\, S^D(x') + K_{TD}(x, x')\, S^T(x'')\right] dx'$$

$$S^T(x) = S_1^T(x) + \int_o^d \left[K_{DT}(x, x')\, S^D(x') + K_{TT}(x, x')\, S^T(x')\right] dx'.$$

Note that the equations are coupled through deuterium-tritium charge exchange events. As usual, the K_{ij} terms are the kernels representing the interaction of neutral specie i with an ion of specie j.

4.8 Discretized Matrix Scheme

By analogy to equation (4-39), these coupled integral equations can be written in matrix form as:

$$\vec{S}^D = \vec{S}_1^D + \bar{\bar{K}}_{DD} \cdot \vec{S}^D + \bar{\bar{K}}_{TD} \cdot \vec{S}^T \qquad (4\text{-}50)$$

$$\vec{S}^T = \vec{S}_1^T + \bar{\bar{K}}_{DT} \cdot \vec{S}^D + \bar{\bar{K}}_{TT} \cdot \vec{S}^T.$$

This system of equations can be solved by creating a "super matrix" composed of the kernel matrices K_{ij}:

$$\begin{bmatrix} \bar{\bar{1}} - \bar{\bar{K}}_{DD} & -\bar{\bar{K}}_{TD} \\ -\bar{\bar{K}}_{DT} & \bar{\bar{1}} - \bar{\bar{K}}_{TT} \end{bmatrix} \cdot \begin{bmatrix} \vec{S}_D \\ \vec{S}_T \end{bmatrix} = \begin{bmatrix} \vec{S}_1^D \\ \vec{S}_1^T \end{bmatrix}$$

where the kernels are given by:

$$K_{DD}^{j,k} \equiv \frac{1}{2} \frac{n_D \langle \sigma v \rangle_{cx}^{DD}}{\mu_{j,k}^D} \frac{\Delta x_k}{\Delta x_j} \left[E_2 \left(\beta_{jk}^{D-} \right) - E_2 \left(\beta_{jk}^{D+} \right) \right]$$

$$K_{TT}^{j,k} \equiv \frac{1}{2} \frac{n_T \langle \sigma v \rangle_{cx}^{TT}}{\mu_{j,k}^T} \frac{\Delta x_k}{\Delta x_j} \left[E_2 \left(\beta_{jk}^{T-} \right) - E_2 \left(\beta_{jk}^{T+} \right) \right]$$

$$K_{TD}^{j,k} \equiv \frac{n_D \langle \sigma v \rangle_{cx}^{TD}}{n_T \langle \sigma v \rangle_{cx}^{TT}} K_{TT}^{j,k}$$

$$K_{DT}^{j,k} \equiv \frac{n_T \langle \sigma v \rangle_{cx}^{DT}}{n_D \langle \sigma v \rangle_{cx}^{DD}} K_{DD}^{j,k}$$

Note that the order of this super matrix is a factor of 2 larger than the one specie case. As before, the inversion of this matrix yields the charge exchange source vectors $\vec{S}^{D}(x)$ and $\vec{S}^{T}(x)$ after an infinite number of charge exchange generations. These quantities then enable the evaluation of all the other parameters of interest (ionization rates, energy sources/sinks, neutral outflux energy spectrum, etc.).

4.9 Two Species Results

Perhaps the most striking consequence of modelling deuterium and tritium as seperate species occurs when a tokamak plasma composed of 90% D^{+} and 10% T^{+} is subjected to a pure D^{o} neutral flux. The surprising results of such a two specie simulation is presented in Figure (4-6).

Note that near the plasma edge, the particle source rate for tritium is actually negative, i.e. there is a large sink of tritium near the edge! This follows from the charge-exchange and subsequent replacement of tritium ions with deuterium ions. Since a fraction of the tritium neutrals born near the edge region travel towards the plasma core, they become ionized there, serving as a source of tritium ions. Thus, by modelling deuterium and tritium as seperate species, a scenario of deep tritium fueling employing only a deuterium gas puff can be envisioned.

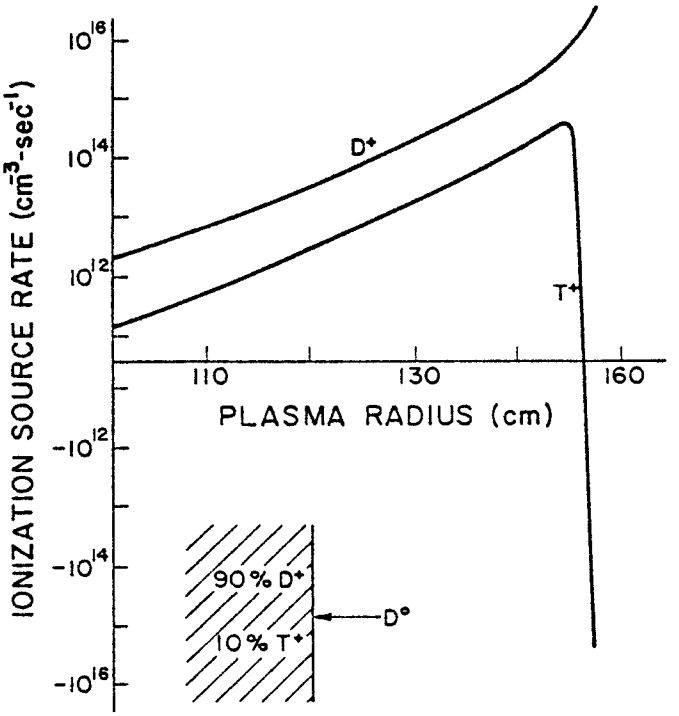

Figure (4-6) Deuterium and Tritium ionization source rate as a function of normalized plasma radius evaluated using two specie SPUDNUT code.

TABLE (4-1)

ATOMIC REACTIONS FOLLOWED IN TWO SPECIE

NEUTRAL TRANSPORT MODEL

$$D^0 + D^+ \rightarrow D^+ + D^\circ$$
$$D^\circ + T^+ \rightarrow T^\circ + D^+$$
$$T^\circ + D^+ \rightarrow D^\circ + T^+$$
$$T^\circ + T^+ \rightarrow T^\circ + T^+$$

$$e^- + D^\circ \rightarrow D^+ + 2e^-$$
$$D^+ + D^\circ \rightarrow 2D^+ + e^-$$
$$T^+ + D^\circ \rightarrow D^+ + T^+ + e^-$$

$$e^- + T^\circ \rightarrow T^+ + 2e^-$$
$$D^+ + T^\circ \rightarrow T^+ + D^+ + e^-$$
$$T^+ + T^\circ \rightarrow 2T^+ + e^-$$

CHAPTER 4 REFERENCES

1. D.F. Duchs, D.E. Post, P.H. Rutherford, Nuclear Fusion 17, 565 (1977).

2. J.T. Hogan, "Multifluid Tokamak Transport Models", in Methods of Computational Physics (J. Killeen, Ed.), Academic Press, New York 16, p. 131 (1976).

3. E. Greenspan, Nuclear Fusion 14, 771 (1974).

4. Z. El-Derini, E.M. Gelbard, Trans. Am. Nuclear Soc. 23, 45 (1976); "Neutral Transport Code in Plasma", Argonne National Laboratory Report FPP/TM-75 (1977).

5. J.H. Marable, E.M. Oblow, Nuclear Sci. Eng. 61, 90 (1976).

6. W. Pfeiffer, "Calculation of Neutral Transport in a Plasma Using A Neutron Transport Method", General Atomic Company Report GA-A13995 (1976).

7. J.G. Gilligan, S.L. Gralnick, W.G. Price, Jr., T. Kammash, Nuclear Fusion 18, 63 (1978).

8. H. Howe, private communication.

9. P.D. Crout, Trans. AIEE 60, 1235 (1941).

CHAPTER 5

PLASMA/WALL INTERACTIONS

This chapter represents a review[1-3] of those processes which are believed to occur in the scrape-off zone of tokamaks. This zone of plasma/wall interactions is defined as the area between the plasma "edge" (as created by a separatrix or limiter tip) and the vacuum wall. Since the detailed study of plasma/wall interactions is still in its infancy, many processes can only be quantified to within an order of magnitude. However, due to the growing appreciation that plasma/wall interactions play a significant role in tokamak discharges, this lack of precision is temporary.

The study of plasma/wall (PW) interactions can be divided into two parts: (1) determination of the type, magnitude and energy distribution of incident particles to the wall and limiters of the device, and (2) the response of the wall and limiters to such bombardment. Once these aspects have been quantified, a model for PW interactions can be created which when incorporated into a model for plasma transport can assess the impact of these interactions on overall plasma performance. Such a model will be described in Chapter 7.

5.1 Energy and Particle Fluxes to Wall and Limiter

The torus wall and limiter are subjected to: (1) energetic ions diffusing from the plasma, (2) radiation from the bulk plasma, and (3) charge-exchange neutrals.

In a stable system with a limiter, very little plasma outflux will impact upon the wall. This conclusion is reached by examining the ratio $\Gamma_\perp/\Gamma_\parallel$ for plasma in the scrape-off zone. $\Gamma_\perp$ represents the cross-field plasma flux and $\Gamma_\parallel$ is the transport of plasma along field lines in the scrape-off zone. Representing the fluxes by:

$$\Gamma_\perp \simeq -D\nabla n \tag{5-1}$$

$$\Gamma_\parallel \simeq nV_{th}$$

where V_{th} is the plasma thermal velocity, the ratio $\Gamma_\perp/\Gamma_\parallel$ becomes:

$$R \equiv \frac{\Gamma_\perp}{\Gamma_\parallel} = \frac{Dn}{n\ell V_{th}} = \frac{4.5\sqrt{T_{ev} \cdot AMU}}{B_{gauss} \cdot \ell_{cm}} \tag{5-2}$$

for Bohm-like diffusion with gradient scale length ℓ. For $B_{gauss} = 6 \times 10^4$ gauss, $T_{ev} = 100$ eV, $\ell = 5$ cm. and AMU = 2.5 the ratio is:

$$R \simeq 2 \times 10^{-4} \tag{5-3}$$

Thus most of the transport is in the parallel direction. The magnitude and energy of this parallel flux can be estimated by:

$$\Gamma_{\parallel} = \frac{\bar{n}\, V_P}{\tau_p\, A_{LIM}} \; ; \; Q_{\parallel} = 2kT\, \Gamma_{\parallel} \qquad (5\text{-}4)$$

For τ_p = .1 sec, $\bar{n} = 2 \times 10^{14}$ cm^{-3}, $V_P = 2 \times 10^{8}$ cm^3, T = 200 eV and $A_{LIM} = 2 \times 10^{4}$ cm^2 (poloidal limiter of width 10 cm):

$$\Gamma_{\parallel} = 2 \times 10^{19}/\text{cm}^2 - \text{Sec.}$$

$$Q_{\parallel} = 1200 \text{ Watts/cm}^2.$$

The limiter will thus be subjected to intense heat and particle fluxes if the edge temperatures are large and the confinement time short. Such fluxes will erode the limiter surface rapidly via sputtering (section 5.5). From both an engineering (heat transfer) and plasma physics (impurity production) point of view, the prediction of edge temperatures and confinement times are of great importance.

The flux which does reach the wall is primarily charge-exchange DT neutrals. However, charge-exchange with impurity ions may also be important. The resonant charge-exchange of neutral atoms with hot plasma ions produces a neutral flux to the wall which is directly proportional to the incoming neutral flux. The energy distribution of this flux for non-beam heated plasmas is roughly Maxwellian. The temperature of this Maxwellian is

characteristic of the edge ion temperature if the plasma is opaque to core-born charge-exchange neutrals. This is the case when the $\bar{n}a > 10^{15}/cm^2$ [4] 'gas blanket' criterion is achieved. Calculations[5] of neutral transport have yielded neutral fluxes to the first wall in the range $10^{15} \rightarrow 10^{17}/cm^2$ - sec. with effective temperatures of 100 → 1000 eV. Since there are many energetic particles in the tail of such distributions the sputtering yield can be significantly enhanced over the mono-energetic estimate.

Radiation from the plasma consists of bremsstrahlung, line, and recombination photons. Since most low Z impurities (carbon, oxygen) are fully stripped in the center of the plasma, they tend to radiate energy primarily from the periphery[6]. Higher Z materials such as iron or tungsten, being incompletely stripped at the plasma center, will radiate primarily from this region. Estimates of the radiative power flux to the wall can easily be made. Typically 50% of the Ohmic heating power is radiated away in present tokamak discharges, depending of course on the purity of the plasma. If $P_\Omega \simeq 300$ kW then $P_{Rad} \simeq 150$ kW. Spreading this isotropic flux over the first wall in a device of minor radius 30 cm and aspect ratio 3, the radiative power flux is on the order of 2 W/cm^2. This has been verified experimentally on the ST tokamak[7]. Such low energy fluxes will not cause impurity generation via thermal evaporation (section 5.6). Extrapolation to fusion reactor regimes indicates radiative fluxes on the order

of 100 W/cm^2, again too small to be a concern.

5.2 Reflection and Trapping Phenomena

The behavior of ions and neutrals upon wall and limiter impact is an important aspect of PW modelling since: (1) the reflection of fuel ions will have an immediate impact upon the plasma density balance and (2) the trapping and subsequent release of incident ions will provide a time-dependent source of fuel. The problem of trapping and re-release is also a concern to those responsible for minimizing the on-site tritium inventories of near term ignition experiments[8].

To date a great body of experimental data for the reflection of ions from surfaces as a function of incident energy has been assembled[9-12]. It has been noted that if the reflection coefficient R_p is plotted against the reduced energy ϵ (as introduced by Lindhard[13]), a universal curve is obtained (Figure 5-1). The reduced energy is defined as:

$$\varepsilon = \frac{32.5\ M_2}{(M_1 + M_2)\ (Z_1^{2/3} + Z_2^{2/3})^{\frac{1}{2}}\ Z_1 Z_2} E(\text{Kev}) \qquad (5\text{-}5)$$

where M_1, Z_1 and M_2, Z_2 are the dimensionless mass and charge numbers of the incident and target atoms respectively. Measurements of R_p at small energies ($\sim$ 10 ev) are difficult to make. However, the low energy data to date suggests that the universal

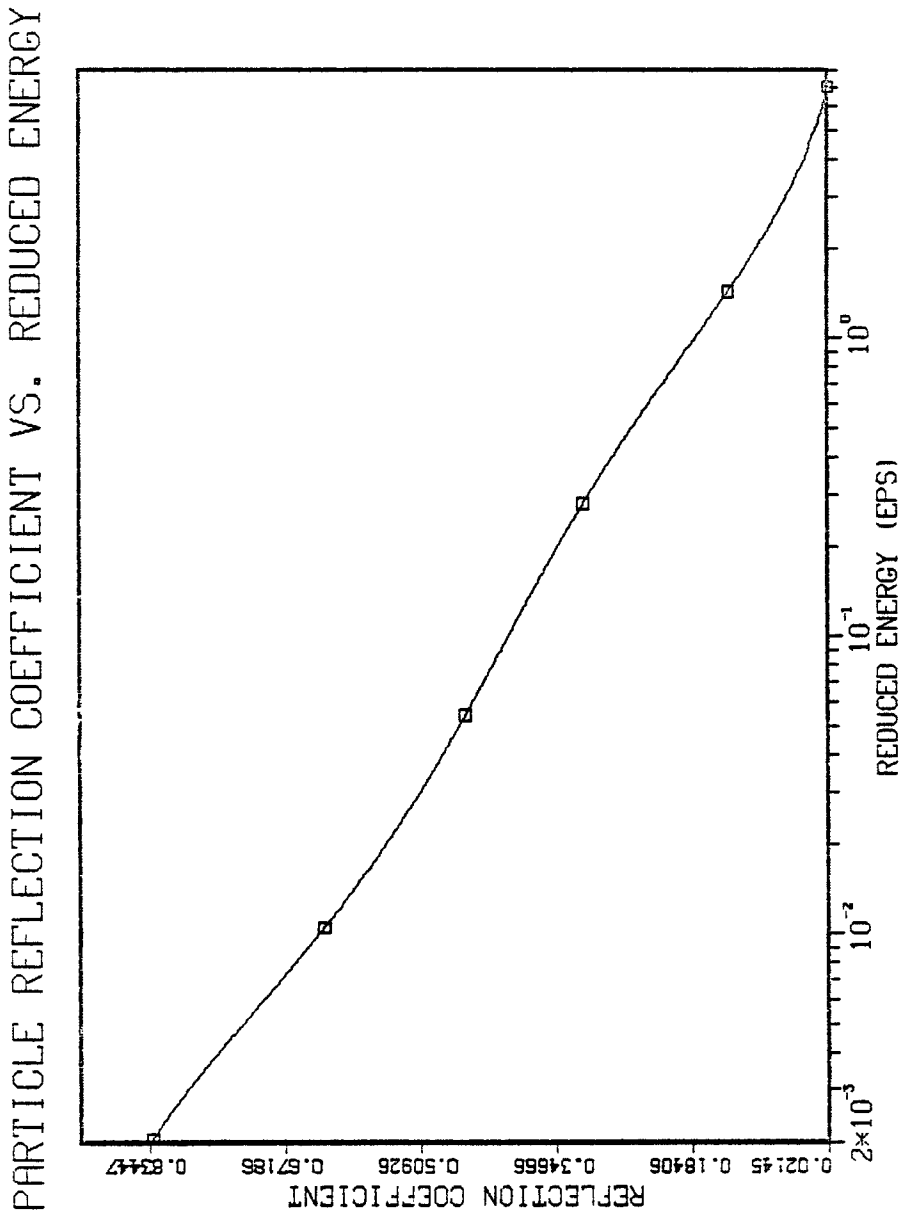

Particle (5-1) Particle reflection coefficient as a function of reduced energy.

curve concept still applies[14].

The energy reflection coefficient R_e can also be expressed as a function of the reduced energy ε. Figure (5-2) is a plot of R_e versus ε. As the energy of the incident particles is reduced the average energy of the reflected particles approaches the incident energy. The angular dependence of the reflection coefficients yields a maximum ($\sim$ factor of 3) at approximately 60° from normal incidence. The backscattered atoms have an angular dependence roughly given by $(\cos\theta)^{-\nu}$, where $\nu \underset{\sim}{>} 1$.

Those incident ions not backscattered from the limiter or wall surface will thermalize in the material and become trapped. The behavior of this trapped gas depends upon the material, the temperature and damage history of the lattice and the chemical reactivity of the gas with the substrate.

In the case of hydrogen, the diffusion coefficient is large and in unreactive metals such as nickel the implanted gas diffuses to the surface at a rate determined by temperature and implantation depth. If the sample has a large concentration of damage sites (produced by hydrogen or helium implantation) the diffusion rate can be significantly reduced. The time dependence of the re-emission of implanted gas in an undamaged sample is given by the expression[15]:

$$J/J_o = \mathrm{erf}\left[\frac{R}{\sqrt{4Dt}}\right];\ R \equiv \text{ion range} \qquad (5\text{-}6)$$

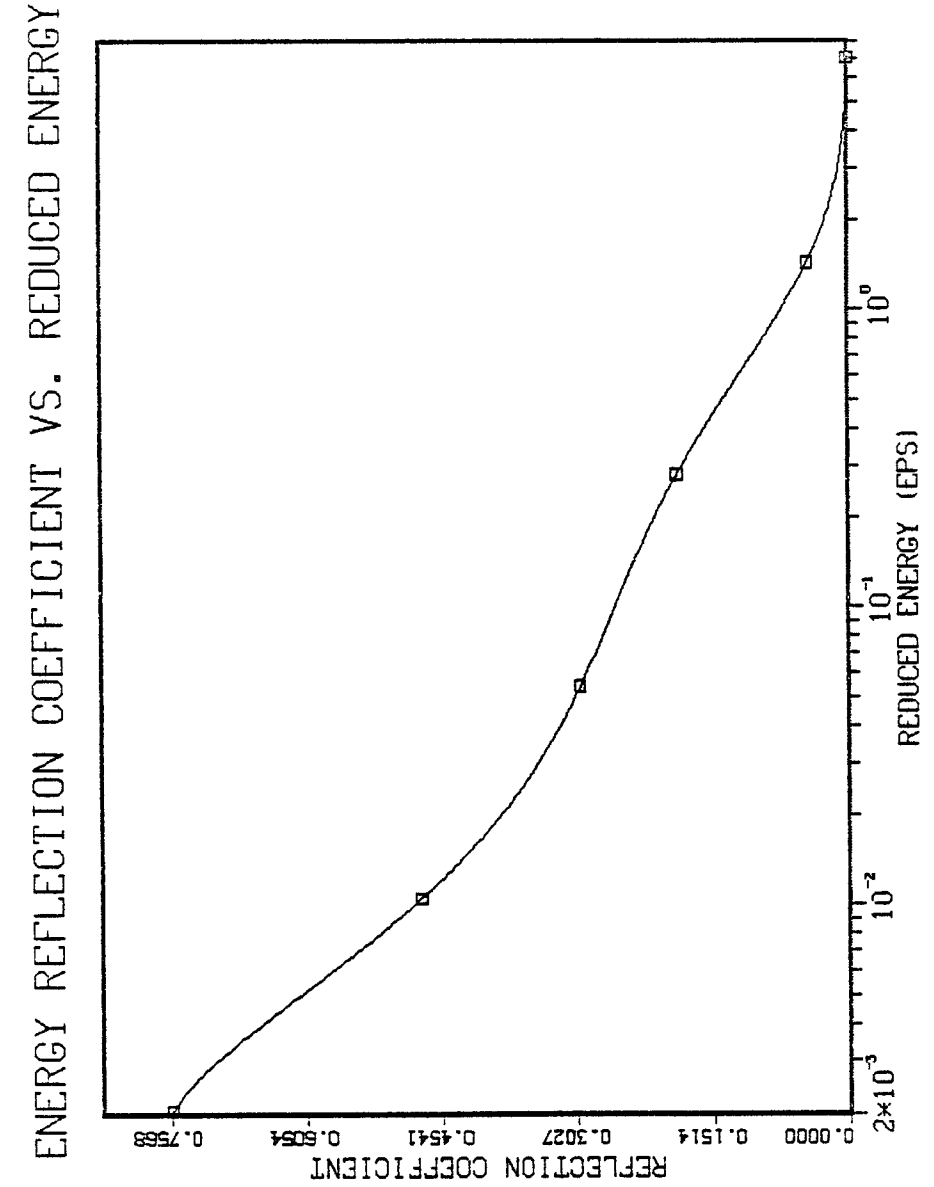

Figure (5-2) Energy reflection coefficient as a function of reduced energy.

A plot of J/J_o versus time is presented in Figure (5-3) for various values of $R/\sqrt{D}$. A more detailed treatment of wall diffusion will be presented in Chapter 7.

In addition to the thermal diffusion of trapped gas, atoms trapped in a material can be 'desorbed' by surface ion impact. Representing the cross-section for desorption by σ, the concentration c in the surface obeys the equation:

$$\dot{c} = \Gamma(1 - R_p) - \Gamma c\sigma \qquad (5\text{-}7)$$

where Γ is the incident flux. This equation has the solution:

$$c(t) = \frac{1 - R_p}{\sigma}\,(1 - \exp(-\Gamma\sigma t)). \qquad (5\text{-}8)$$

From experimental values of saturation ($c(t) \underset{\sim}{} \text{constant}$), the desorption cross-section can be determined. For incident energies of $\sim$10 Kev; $\sigma \underset{\sim}{} 10^{-17}$ cm^2 [16]. At energies characteristic of the scrape-off zone, however, $\sigma \underset{\sim}{} 10^{-19}$ cm^2. In a reactor, with walls operating at 500°C, thermal diffusion will be the dominant process for trapped gas release.

5.3 Sheath Effects

Any insulated object immersed in a plasma will develop an electrostatic sheath. The potential of the sheath assumes a value consistent with zero net electrical current. The presence

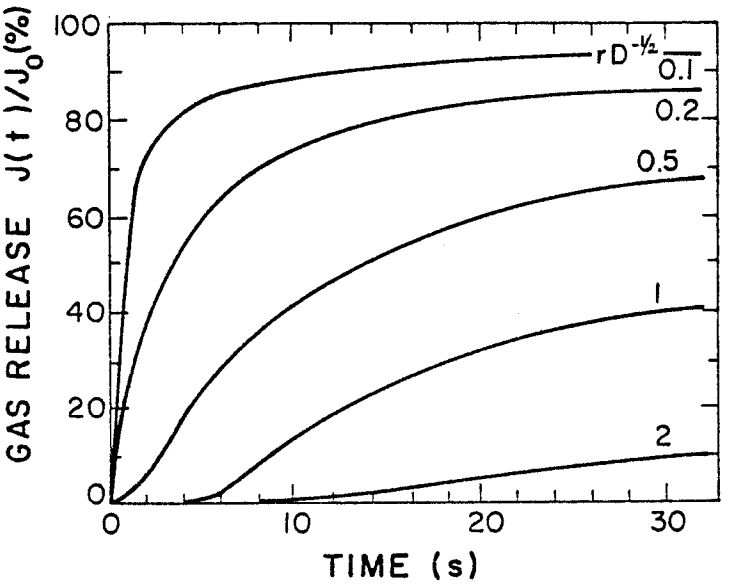

Figure (5-3) Normalized wall release rate as a function of time for several values of $R/\sqrt{D}$.

of such a sheath at the plasma/limiter interface can serve as an acceleration mechanism for those fuel ions and ionized impurities comprising the parallel flux in the limiter shadow[17]. These accelerated ions have impact energies greatly in excess of their thermal values. This leads to the creation of a hot neutral recycling flux and to enhanced limiter erosion due to sputtering.

The importance of the sheath effect can be dramatized by the following example. Assume that the scrape-off electron temperature is 100 ev. At this temperature calculations show that oxygen will be six times ionized[18]. Since the magnitude of the sheath potential is roughly $4T_e$, the oxygen ion will have an energy in excess of 2500 ev upon limiter impact! In addition, those neutrals undergoing acceleration and reflection at the limiter re-enter the discharge as neutrals whose energies approach the sheath potential. These neutrals will penetrate the plasma more deeply than, say, Franck-Condon neutrals, thereby influencing the ionization source rate.

To determine the depth of the sheath potential, the electron and ion fluxes to the limiter are equated. Define the ion flux as:

$$\Gamma_{\shortparallel}^{+} = \int f_i(v)\, V_z\, d^3v \qquad (5\text{-}9)$$

where $f_i(v)$ is the ion distribution function (assumed Maxwellian):

$$f_i(v) = n_i\left(\frac{m_i}{2\pi kT_i}\right)^{3/2} e^{-m_i V_i^2/2kT_i} \tag{5-10}$$

Performing the integration in equation (5-9) yields:

$$\Gamma_{\perp}^{+} = \frac{n_i V_i}{4} \; ; \; V_i = \sqrt{\frac{8kT_i}{\pi m_i}} \; . \tag{5-11}$$

The electron flux is evaluated in a similar fashion but with a change in integration limits. Since the sheath potential ϕ_o is negative, a class of impinging electrons will be reflected. Classically all electrons whose energies are less than $|e\phi_o|$ will be excluded. Define the minimum electron velocity in the z direction capable of reaching the limiter surface as V_o:

$$V_o = \sqrt{\frac{2|e\phi_o|}{m_e}} \; . \tag{5-12}$$

This value becomes the lower limit on the integration over V_z. The expression for the collected electron flux then becomes:

$$\Gamma_{\perp}^{-} = \left(\frac{n_e V_e}{4}\right) e^{-|e\phi_o|/kT_e} . \tag{5-13}$$

Equating (5-11) and (5-13) the potential depth $|e\phi_o|$ is found to be:

$$|e\phi_o| = \frac{kT_e}{2} \ln\left[\frac{T_e}{T_i}\frac{m_i}{m_e}\right] . \tag{5-14}$$

Defining the energy flux to the limiter as:

$$Q_{\perp} \equiv \int \frac{1}{2} m v^2 \, f(v) \, V_z \, d^3v \tag{5-15}$$

yields the relation:

$$Q_{\perp} = (2kT) \, \Gamma_{\perp}. \tag{5-16}$$

Thus the total energy of an impacting ion of charge Z is:

$$E_{TOT} = 2kT + Z\left(\frac{kT_e}{2}\right) \ln \left(\frac{T_e}{T_i} \frac{m_i}{m_e}\right) \tag{5-17}$$

For hydrogen, the logarithmic factor is roughly 7.5 when $T_i \simeq T_e$.

The phenomenon of secondary electron emission serves to limit the sheath potential as T_e increases. As the ions and electrons which impact upon the limiter increase in energy, the collision process ejects electrons from the surface thereby reducing the sheath potential. The general expression for the sheath potential incorporating secondary electron emission has been shown to be[19]:

$$|e\phi_o| \simeq \frac{kT_e}{2} \ln\left[\frac{T_e}{T_i} \frac{m_i}{m_e} \gamma\right] \tag{5-18}$$

where: $\gamma = \left(\frac{1 - \gamma_e}{1 + \gamma_i}\right)^2 < 1$

γ_e, γ_i being the energy dependent secondary electron emission coefficients for electrons and ions respectively.

5.4 Desorption of Absorbed Gases

Upon contact with the first wall, fuel ions become neutralized and may adhere to the surface under the action of Van der Waal forces. Typical binding energies for the force are of the order of .3 ev. Several monolayers of gas can quickly form on the surface. An estimate of the magnitude of this particle reservoir can easily be made. If a torus of minor radius a is covered by a 10% gas monolayer and through a "black-box" process is evolved into the chamber, the particle density n would be:

$$n = \left(\frac{2}{a}\right) n_{\omega}. \qquad (5\text{-}19)$$

where n_{ω} is the concentration of gas on the wall. Assuming $n_{\omega} \underset{\sim}{\sim} 2.5 \times 10^{15}$ molecules/cm^2 and a minor radius of 100 cm, the resulting density is:

$$n \underset{\sim}{\sim} 1 \times 10^{14} \text{ atoms/cm}^3.$$

This value is on the order of the initial density of the discharge! Having motivated the study of adsorbed gases, the mechanisms by which this gas can be desorbed from the wall is investigated.

The rate at which gas randomly desorbs from a metallic surface due to thermal effects is described by an equation of the form[20]:

$$\dot{c} = \frac{-c}{\tau_o} \exp(-E_B/kT) \qquad (5\text{-}20)$$

where c represents the surface concentration, E_B the binding energy of adsorbed gas, T the surface temperature and τ_o a constant on the order of 10^{-13}. The e-folding time for thermal desorption is a strong function of binding energy. For example, weakly bound gas ($E_B \sim .3$ ev) on a surface with a temperature of 293 K has an e-folding time of 1.4×10^{-8} seconds. However, with $E_B \sim 5$ ev even with temperatures approaching 800 K, the e-folding desorption time is nearly 10^{11} years! Thus, the 'bake-out' procedures remove the loosely bound adsorbed gas, leaving the more tightly bound gas to be desorbed by particle impact.

The impact of energetic electrons, ions and neutrals on adsorbed gas layers serves to erode the layers as a function of time. Such an erosion process can be characterized by a cross-section :

$$\dot{c} = -C_o \Gamma\sigma e^{-\Gamma\sigma t} \qquad (5\text{-}21)$$

where C represents the adsorbed gas concentration and Γ the flux of particles to the surface. Plots of $\dot{c}$ versus time yields the cross-section σ. Typical values of σ for ion-induced desorption range from $10^{-16} \rightarrow 10^{-15}$ cm^2 [21], with yields on the order of $1 \rightarrow 10$ atoms/ion. For typical charge-exchange fluxes on the order of $10^{16}/cm^2$ -sec, the e-folding time for tightly bound adsorbed gas via ion induced desorption is roughly .1 second. In a long pulse reactor, the modelling of such transient effects need not be considered. The desorption efficiencies of electrons

are a factor of 10 less than ions and neutrals, hence their impact can be neglected[22].

While the preceding section has demonstrated that particle induced desorption need not be incorporated in a model of the plasma/wall interactions in the scrape-off zone of a reactor, it does indicate that particle desorption may be an effective cleaning mechanism. In fact, the success of "discharge cleaning" in improving the discharge characteristics of tokamaks relies directly upon the phenomenon of particle induced desorption[23].

5.5 Sputtering

When an energetic ion or neutral interacts with a surface, the transfer of momentum involved in the collision may be large enough to eject atoms from the material. The general theory of sputtering predicts yields in reasonable agreement with experiment for medium to heavy ion/target combinations, while low energy, light-ion estimated yields have been in poor agreement with experiment. However, recent Monte Carlo calculations of Hagmar[24] have yielded light ion sputtering coefficients which are comparable to experiment. It is precisely these ions and energies which are of critical importance in the modelling of the scrape-off zone. Experimental results for ions and energies in the fusion regime have recently been compiled by the Garching group[25]. The analysis of this data base revealed that the sputtering yield S(E) could be factored into an energy dependent

expression $f(E^*)$ and a material dependent expression $Q(M_1, M_2, E_B)$:

$$S(E) = f(E^*) \cdot Q(M_1, M_2, E_B) \tag{5-22}$$

where M_1, M_2 represent the masses of the incident and target atoms respectively, E_B is the sublimation energy of the solid and E^* is a dimensionless energy parameter defined by:

$$E^* \equiv \frac{E}{E_{th}} \; ; \; E_{th} = \frac{E_B}{\gamma(1 - \gamma)} \tag{5-23}$$

where: $\gamma = \dfrac{4M_1M_2}{(M_1 + M_2)^2}$

The threshold energies E_{th} for several ion/target combinations are given in Table (5-1).

Plotting yield versus E^*, the energy dependence of S(E) was found to be (Figure (5-4)):

$$f(E^*) \simeq 8.5 \times 10^{-3} \, (E^*)^{1/4} \, (1 - 1/E^*)^{7/2} \tag{5-24}$$

Plotting the ratio Q/M_2 versus γ, (Figure (5-5)), the material dependence of S(E) was found to be represented by the expression:

$$Q(M_1, M_2, E_B) \simeq .75 \, M_2(\gamma)^{5/3} \tag{5-25}$$

The complete expression for the energy dependent sputtering yield for low energy, light ions then becomes:

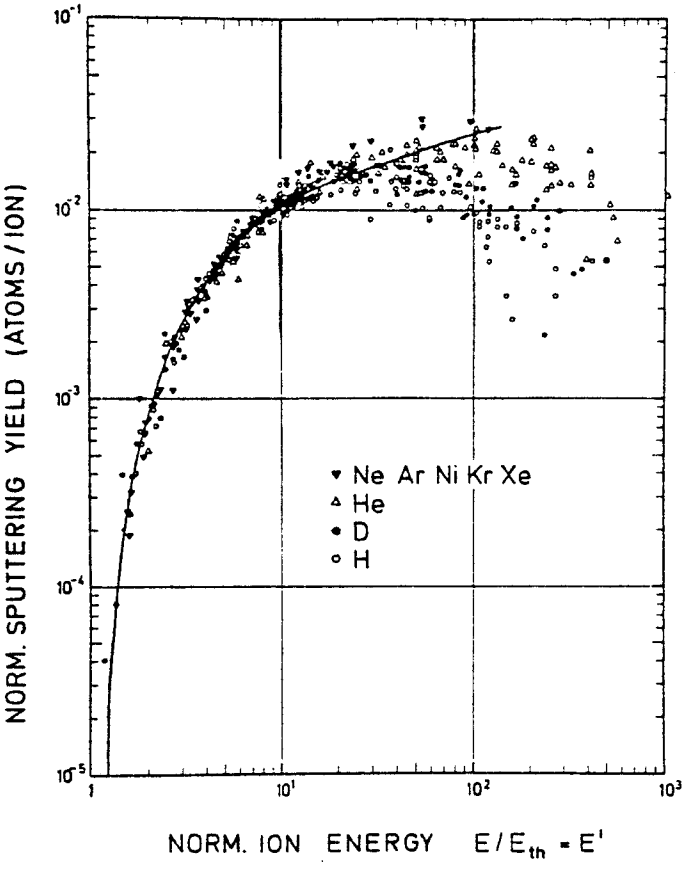

Figure (5-4) Energy dependence of sputtering yield as a function of normalized energy.

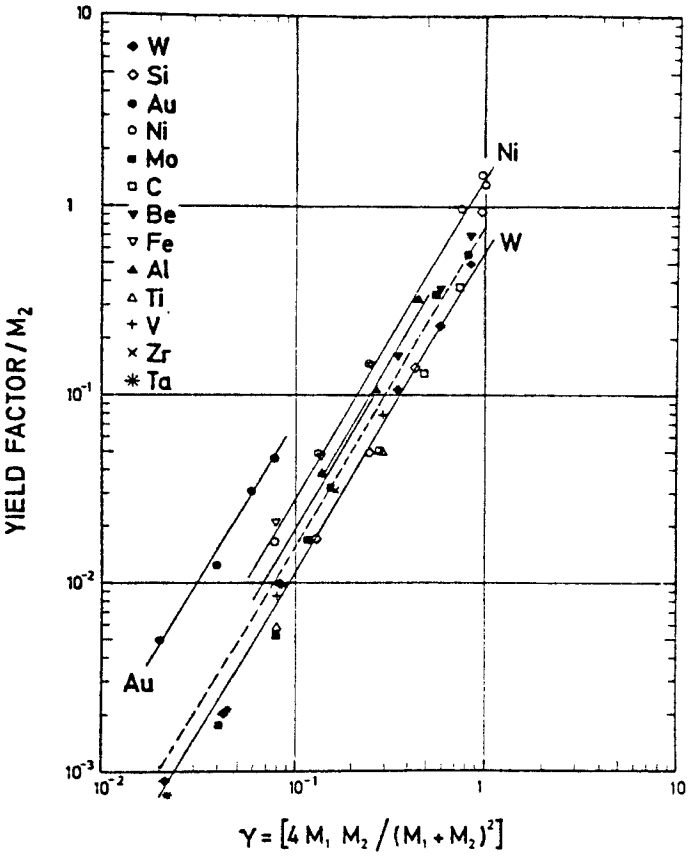

Figure (5-5) Mass dependence of sputtering yield as a function of γ.

$$S(E) = 6.4 \times 10^{-3} (\gamma)^{5/3} M_2 (E^*)^{\frac{1}{4}} (1 - 1/E^*)^{7/2}. \qquad (5\text{-}26)$$

Comparisons of this fit with experimental data indicate that for mass ratios $(M_1/M_2) \lesssim .4$ and $1 < E^* < 20$, equation (5-26) is correct to within a factor of two. Figures (5-6) → (5-10) are plots of the sputtering yield for several candidate wall materials as a function of energy for several light ions.

The angular dependence of S(E) has also been investigated[26]. Figure (5-11) is a plot of normalized angular yield $S(E,\theta)/S(E,0^\circ)$ versus angle of ion incidence for hydrogen and deuterium beams on gold. Note that the data indicates a $(\cos\theta)^{-1}$ dependence. The angular distribution of bombarding particles can thus account for a factor of ∿2 increase over the normal value of S(E).

In addition the angular distribution of sputtered atoms as a function of incident angle has also been investigated[27]. Figure (5-12) is a plot of the differential sputtering yield versus angle of incidence for an 8 KeV H_2^+ beam on a nickel substrate. Note that the sputtered atoms are peaked at ∿30°, only the yield being a function of incident angle.

The modelling of heavy ion sputtering has been achieved by Smith[28]. Blending the theory of Sigmund[29] and experimental observations, an empirical expression for the sputtering yield of heavy ions has been developed. This expression is valuable, for example, when the interaction of multiply charged impurity ions with a limiter assembly is modelled. For normally incident ions

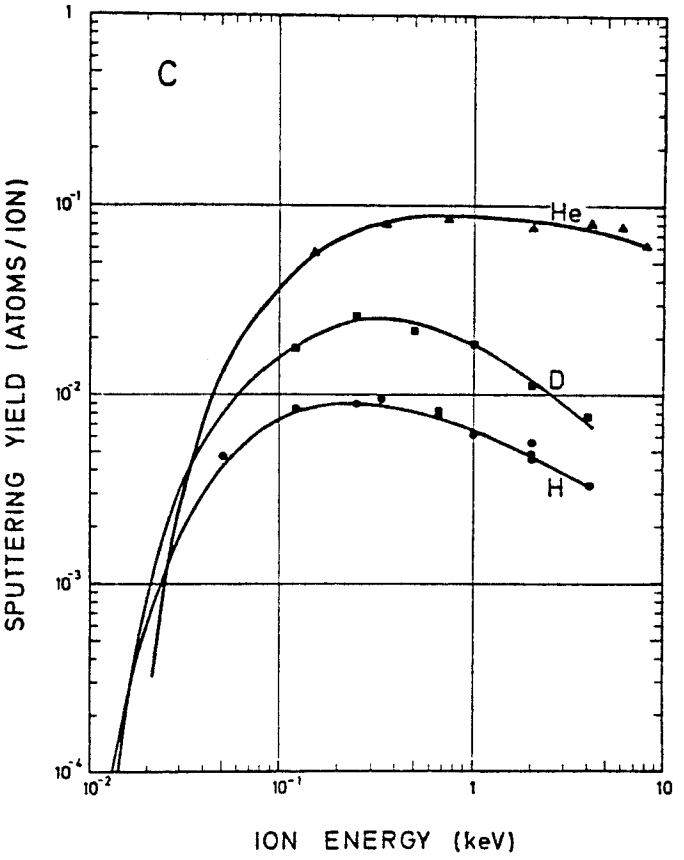

Figure (5-6) Sputtering yield for carbon evaluated using the Garching fit for several light ions.

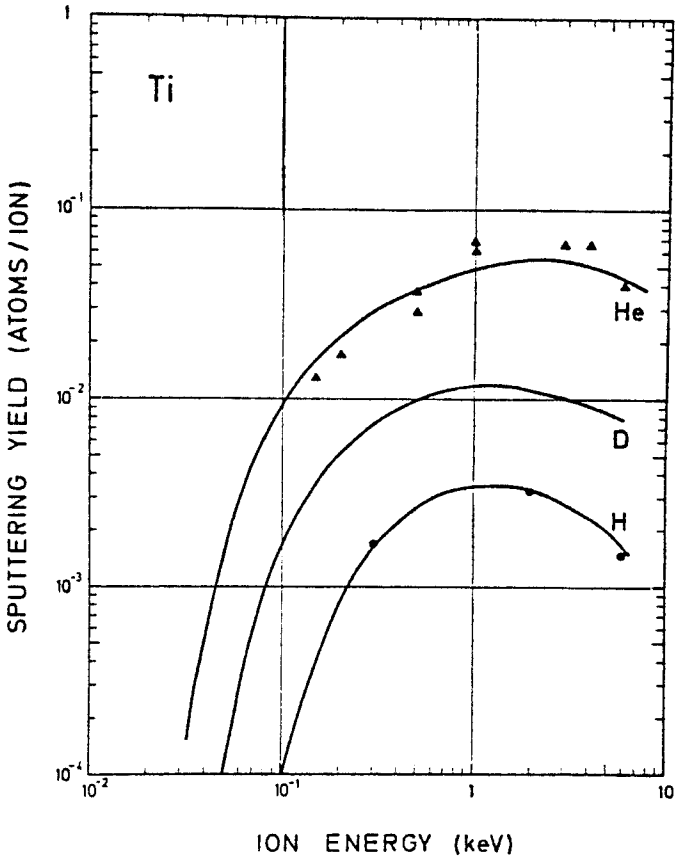

Figure (5-7) Sputtering yield for titanium evaluated using the Garching fit for several light ions.

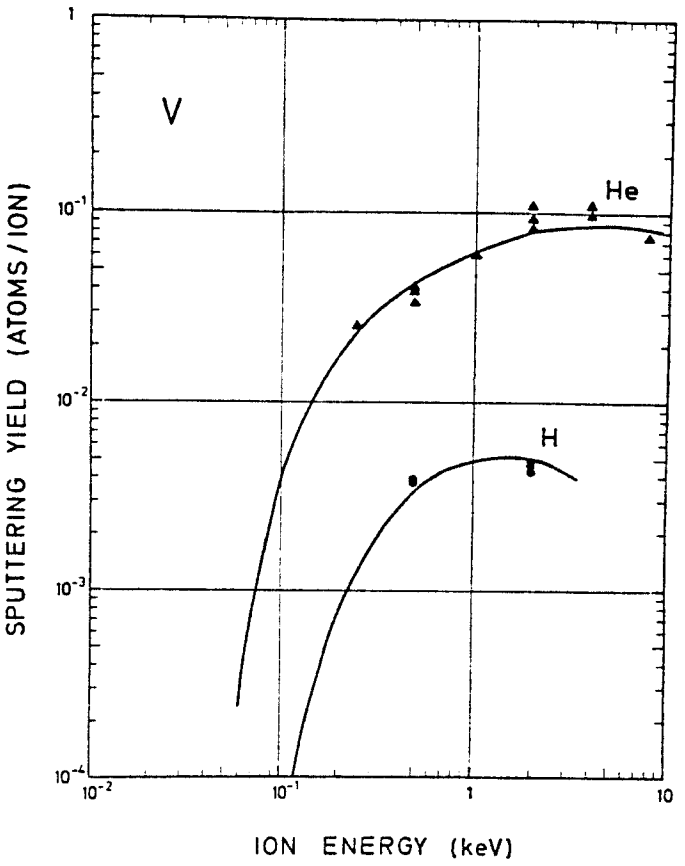

Figure (5-8) Sputtering yield for vanadium evaluated using the Garching fit for several light ions.

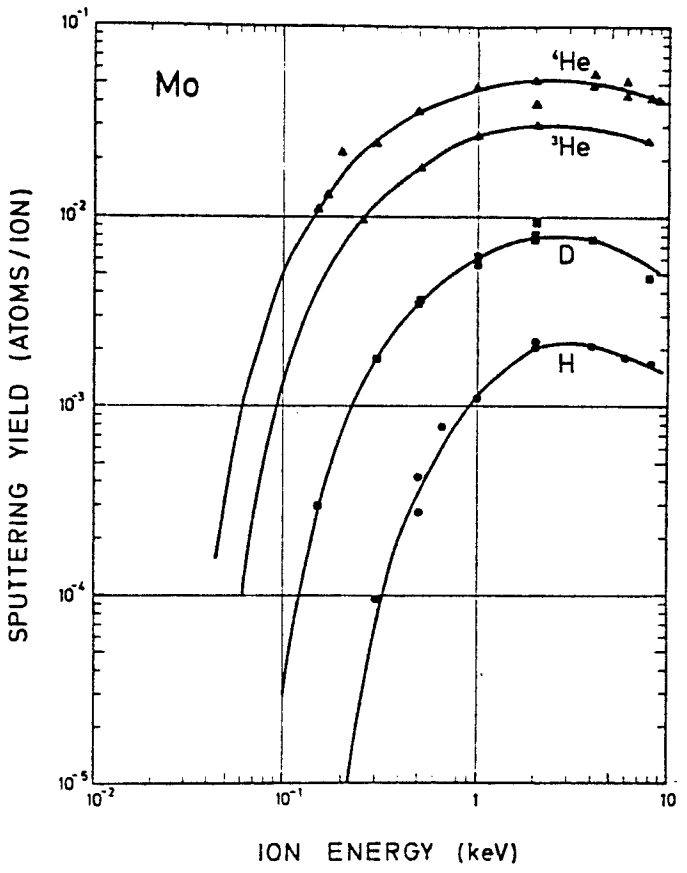

Figure (5-9) Sputtering yield for molybdenum evaluated using the Garching fit for several light ions.

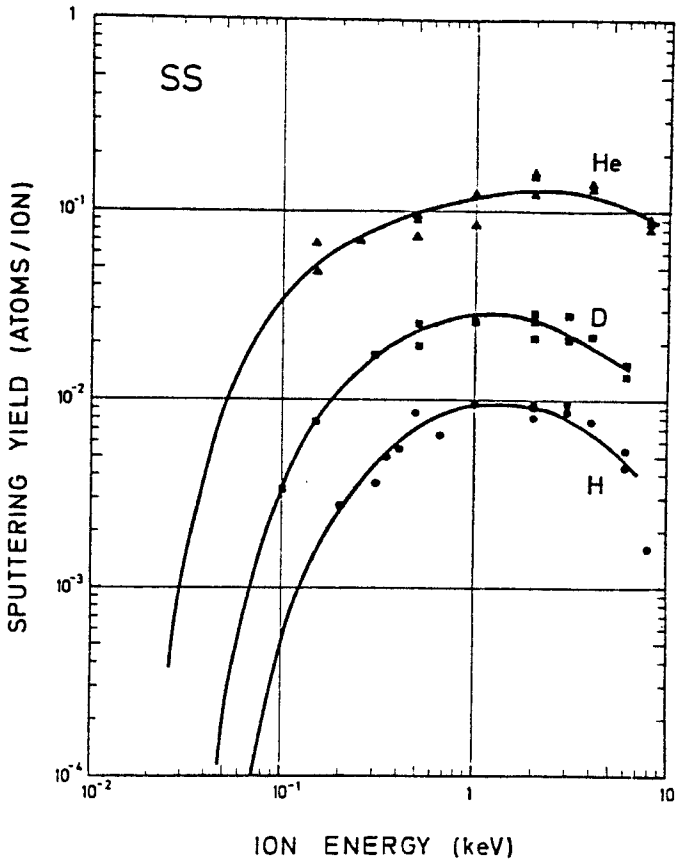

Figure (5-10) Sputtering yield for stainless steel evaluated using the Garching fit for several light ions.

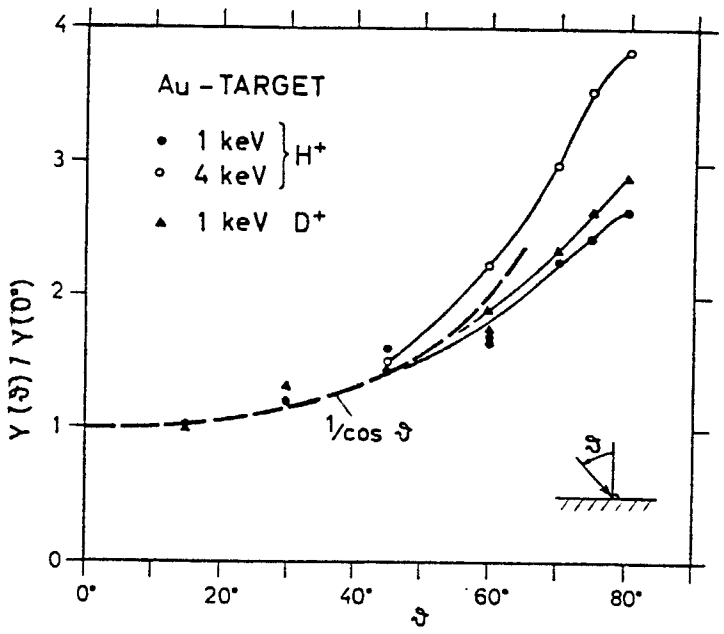

Figure (5-11) Normalized angular dependence of sputtering yield as a function of incident angle for H^+, D^+ on Au target.

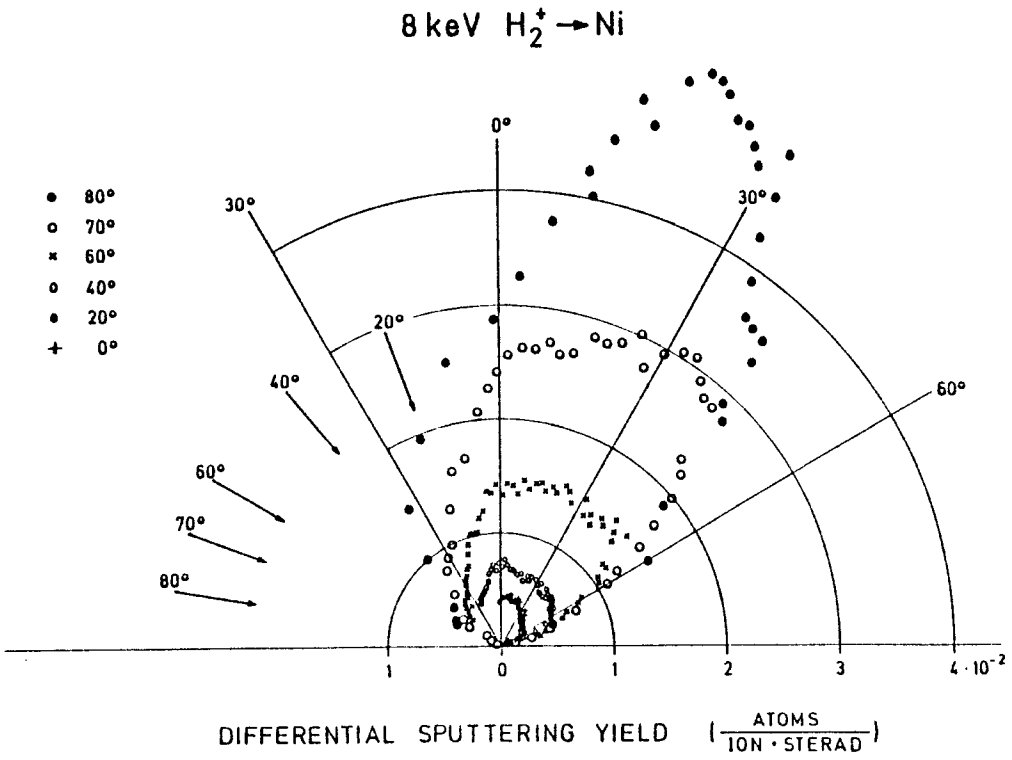

Figure (5-12) Differential sputtering yield on a function of incident angle for 8 Kev H_2^+ on Ni.

of mass and charge number M_1, Z_1 incident on target atoms of mass and charge M_2, Z_2, the yield can be expressed as:

$$S(E) = \frac{20}{U_o} \left(\frac{M_1}{M_2}\right) Z_1^2 Z_2^2 \frac{E}{(E + 50\, Z_1 Z_2)^2} \qquad (5\text{-}27)$$

where E is the incident particle energy in eV and U_o is the surface binding energy in eV. Equation (5-27) is to be applied only for energies greater than "threshold", i.e. for:

$$E > \frac{(M_1 + M_2)}{4M_1 M_2} U_o. \qquad (5\text{-}28)$$

Figure (5-13) is a plot of the "self-sputtering" yield versus incident ion energy for a number of materials. Note that even at modest energies the yield can approach and even exceed unity.

The possibility of self-sputtering yields exceeding unity has important plasma physics consequences. Assume for the moment that only impurity atoms will contribute to sputtering. If the confinement time of impurities in the plasma is defined by τ, then the time rate of change of the impurity density in the plasma is given by:

$$\dot{n} = \frac{-n}{\tau} (1 - S) \qquad (5\text{-}29)$$

where S is the self-sputtering yield. The solution of equation (5-29) is:

$$n(t) = n_o\, e^{\left(\frac{S - 1}{\tau}\right)t} \qquad (5\text{-}30)$$

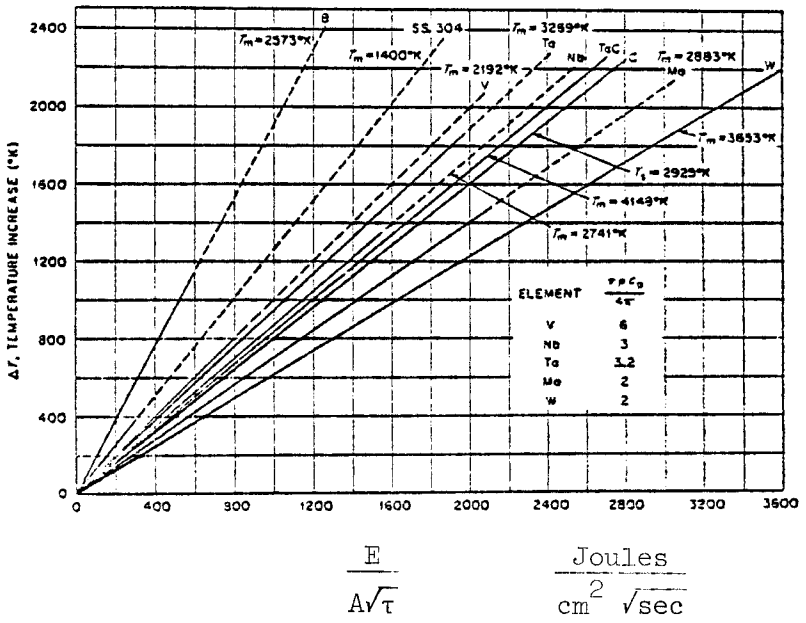

Figure (5-14) Instantaneous rise in surface temperature as a a function of $\frac{E}{A\sqrt{\tau}}$ for several materials.

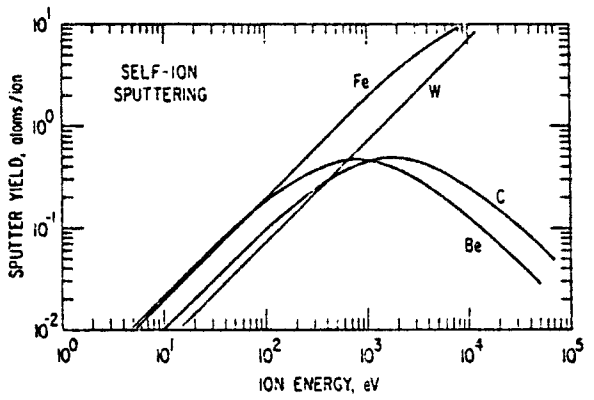

Figure (5-13) Self-sputtering coefficients based on the fit of Smith for several species.

By analogy with neutron multiplication in an infinite medium, if $S > 1$ the impurity density will diverge for $t >> \frac{\tau}{S - 1}$. Given a sputtering yield of 1.1 and a confinement time of .5 seconds, the impurity density will increase by 100% in only 3.5 seconds! Of course this analysis neglects any self-stabilizing effects (such as plasma cooling as n increases, thereby reducing S). However it does highlight the need for a self-consistent model of the scrape-off zone which incorporates self-sputtering phenomena.

In conclusion, empirical expressions modelling both light and heavy ion sputtering have been developed which are in good agreement ($\sim$2) with experiment. The angular dependence of the sputtering yield and sputtered particles has also been investigated, indicating increases in yield by factors of 2 for incident angles approaching 60°. Other factors such as surface imperfections, oxide layers and impurity re-deposition are sources of error in the determination of sputtering yields. The problem of self-sputtering was shown to be an important effect in the modelling of the scrape-off zone since the possibility of an "impurity runaway" was demonstrated.

5.6 Thermal Evaporation

In addition to the process of sputtering, other methods of impurity generation have been proposed to explain the presence of impurities in present day tokamak discharges. This section will investigate the response of a material surface to a heat flux.

In a solid with finite temperature T, there may be atoms in the tail of the distribution whose energy exceeds the surface binding energy. If these particles have momentum directed out from the surface, they will spontaneously escape, resulting in an "evaporation" of the surface. The evaporation rate $\dot{n}$ is described by the expression[30].

$$\dot{n} = 3.5 \times 10^{22} \, (P) \, (\alpha) \, (AT)^{-\frac{1}{2}} \, (\text{atoms/cm}^2\text{-sec}) \qquad (5\text{-}31)$$

where T is the surface temperature in ^{o}K, A the mass number of the solid, α the sticking coefficient ($\sim$1) and P is the vapor pressure of the surface in torr. The vapor pressure follows the well known expression[31]:

$$P = P_o \, e^{-H/kT} \qquad (5\text{-}32)$$

where H is the heat of sublimation of the material in question. For candidate first wall materials such as titanium, vanadium and molybdenum at a temperature of $600^{o}C$, the evaporation rate is predicted to be less than 10^{4} atoms/cm^2-sec. Clearly this is negligible in comparison with sputtering.

However, if a situation develops in which a large quantity of energy is dumped onto a surface in a time shorter than the heat conduction time, extreme surface temperatures may develop which greatly exceed the temperature of the bulk material. These situations may develop due to poor plasma positioning, a plasma

disruption or localized run-away electron beams. The temperature increase ΔT of a solid in response to a quantity of energy E being dumped in a time τ over an area A is given by[32]:

$$\Delta T \sim \frac{2E}{A}\sqrt{\frac{1}{\pi k \rho C_p}\ \frac{1}{\tau}} \qquad (5\text{-}33)$$

where C_p is the specific heat, k the thermal conductivity and ρ the density of the solid. Figure (5-14) is a plot of temperature rise ΔT versus $\frac{E}{A\sqrt{E}}$ for a number of elements.

As an example, if the plasma were to momentarily "lean" on a section of the wall for a short time τ, what would the temperature rise and impurity evaporation rate be? Let:

$$\bar{n}_e = 1 \times 10^{14}\ \text{cm}^{-3}$$

$$\bar{T} = 10^{4}\ \text{eV}$$

$$V_p = 2 \times 10^{8}\ \text{cm}^{3}$$

$$A_{wall} = 3 \times 10^{6}\ \text{cm}^{2}$$

$$\tau = 10^{-3}\ \text{sec.}$$

Assuming that 30% of the plasma thermal energy is to be deposited on 20% of the first wall, the ΔT for a steel wall would be:

$$\Delta T \sim 2500\ ^{\circ}\text{C}$$

or about a factor of two greater than the melting point of steel! The question of plasma contamination in this scenario is moot.

Thus, flash evaporation will be a concern only in situations which can be characterized as "transients". Since the scrape-off model to be developed will not incorporate accident modes, this process will be neglected. While this is justified in modelling, a credible reactor design would have to account for such contingencies.

5.7 Arcing Phenomena

Recently arc tracks have been observed on the limiters and surfaces of ISX[33], DITE[34] and PULSATOR[35]. By measuring the length and depth of these arcs, Figure (5-15), estimates have been made as to the impurity generation rate. These estimates seem to be consistent with observed heavy impurity plasma densities.

A theory for the formation of arcs has been developed by Robson and Thonemann[36]. If the local electron temperature is large enough, the sheath potential at the limiter surface may achieve values consistent with arcing. The arc serves as a copious source of electrons which reduces the sheath further, thereby allowing more electrons to reach the limiter surface. This process creates a circulating current between plasma and limiter surface. The localized heating of the surface due to intense electron bombardment may cause surface melting which in turn creates observable tracks. However, experimentally it is found that arcing in tokamaks occurs primarily during start-up, shut-down or a phase of high MHD activity[37].

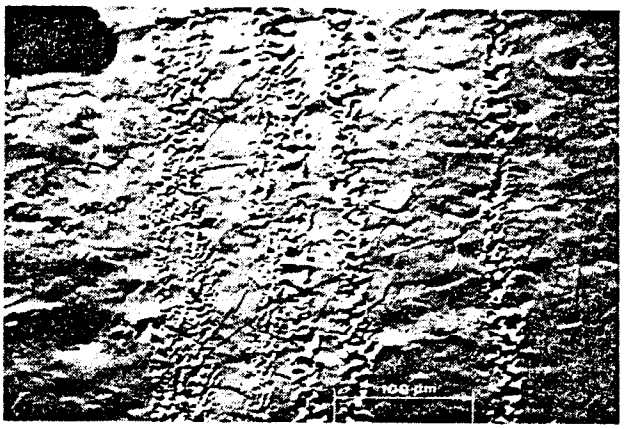

Figure (5-15) Observed arc tracks on limiter surfaces.

The arcing phenomenon may be suppressed by insuring that material surfaces have no surface inhomogenities such as small, sharp appendages which may initiate arcing via the "lightning rod" effect. In addition, the reduction of sheath potentials through a decrease in edge electron temperature should substantially reduce arcing.

5.8 Summary of Plasma/Wall Interactions

In this chapter the plasma/wall interactions which are believed to occur in the scrape-off zone of tokamaks have been examined. Expected fluxes to the walls and limiters have been quantified. In response to such bombardment, processes such as reflection, trapping, re-emission and desorption have been investigated. The impact of sheaths upon sputtering, for both light and heavy ions, has been made. Impurity generation via thermal evaporation was demonstrated to be significant only in an "accident" mode, while the phenomena of arcing,still inadequately understood, may be playing an active role even in present day devices.

Unfortunately, as mentioned in the introduction to this chapter, the study of PW interactions is an area of plasma physics research only now receiving detailed attention. The majority of the above processes are known only qualitatively and those quantitative estimates which do exist are admittedly order of magnitude. However, as research into this rapidly growing

discipline expands, a basic understanding of the physics of plasma/wall interactions will surely follow. The net result of such understanding will be the better modelling of tokamak discharges with an eye towards improving future fusion devices by being able to identify and hopefully suppress those PW interactions found to be deliterious to plasma performance. In the following chapter, several proposed schemes which seek to control the impact of PW interactions on the tokamak discharge will be discussed. In Chapter 7 a model of the scrape-off zone for tokamaks which incorporates the relevant PW interactions examined in Chapter 5 is presented, while in Chapter 8 results of tokamak simulations which utilize this self-consistent scrape-off model will be given.

TABLE (5-1)

THRESHOLD ENERGIES FOR SEVERAL ION/TARGET COMBINATIONS

Target \ Ion	H	D	He^3	He^4
Al	53	34		20.5
Au	184	94	60	44
Be	27.5	24		33
C	9.9	11		16
Fe	64	40		35
Mo	164	86	45	39
Ni	47	32.5		20
Si	24.5	17.5		14
Ta	460	235		100
Ti	43.5			22
V	76			27
W	400	175		100
Zr				60

energy in eV

CHAPTER 5 REFERENCES

1. G.M. McCracken and P.E. Stott, Nuc. Fusion 19, 889 (1979).
2. R. Behrisch, Nuc. Fusion 12, 695 (1972).
3. Plasma-Wall Interactions (Proc. Int. Symp. Jülich, 1976), Pergamon Press, Oxford (1977).
4. B. Lehnert, Nuc. Fusion 13, 69 (1971).
5. See Reference (2-4).
6. TFR Group, Reference #3, page 3.
7. E. Hinnov, J. Nuc. Mat. 53, 9 (1974).
8. J. Cecchi, in Proc. on the Workshop on Hydrogen Recycling, Dublin, CA (October 17-19, 1979), D.O.E. Report CONF 791057, (Feb. 1980).
9. R. Weissmann and P. Sigmund, Rad. Effects 20, 65 (1973).
10. J. Bohdansky, et al., J. Nuc. Mat. 63, 115 (1976).
11. O.S. Oen and M.T. Robinson, Nucl. Instr. and Meth. 132, 647 (1976).
12. R. Weissmann and P. Sigmund, Rad. Effects 19, 19 (1973).
13. J. Lindhard, et al., Mat. Fys. Medd. 33, 39 (1963).
14. W. Eckstein, et al., J. Nuc. Mat. 63, 199 (1976).
15. S.K. Erents and G.M. McCracken, Br. J. Appl. Phys. 2, 1397 (1969).
16. E. Taglauer, et al., Appl. Phys. 49, 47 (1977).
17. R.W. Conn, J. Bohdansky and R. Behrisch, A.P.S. Bulletin, Vol. 22, October, 1977, 8D3.
18. Chapter #2, Ref. #6, Pg. 406.
19. Chapter #3, Ref. #3, Pg. 121.

20. P.A. Redhead, J.P. Hobson and E.V. Kornelsen, The Physical Basis of Ultra-High Vacuum, Chapman and Hall, London, 77 (1968).

21. H.F. Winters, J. Vac. Sci. Tech. 8, 17 (1971).

22. T.E. Madey and J.T. Yates, J. Vac. Sci. Tech. 8, 525 (1971).

23. L. Oren and R.J. Taylor, Nuc. Fusion 17, 1143 (1977).

24. P. Sigmund, Phys. Rev. 189, 383 (1969).

25. J. Roth, J. Bohdansky and W. Ottenberger, Max-Planck-Institut für Plasmaphysik report IPP 9/26 (May, 1979).

26. H.L. Bay and J. Bohdansky, to be published in Applied Physics.

27. H.L. Bay, et al., to be published.

28. D.L. Smith, J. Nuc. Mat. 75, 20 (1978).

29. Reference #24; also see Ref. #12.

30. L. Holland, Vacuum Deposition of Thin Films, John Wiley, (1961).

31. R. Hultgren, et al., Selected Values of Thermodynamic Properties of Metals and Alloys, John Wiley, (1972).

32. M. Jakob, Heat Transfer, Vol. 1, John Wiley, (1958).

33. R.J. Colchin, et al., J. Nuc. Mat. 76/77, 405 (1978).

34. G.M. McCracken and D. Goodall, Nuc. Fus. 18, 537 (1978).

35. P. Staub and G. Staudenmaier, J. Nuc. Mat. 63, 37 (1976).

36. A.E. Robson and P.C. Thonemann, Proc. Phys. Soc. 73, 508 (1959).

CHAPTER 6

CONTROL OF PLASMA/WALL INTERACTIONS

In this chapter a brief review of the schemes for controlling the extent of plasma/wall interactions will be given. These schemes can be divided into two categories, "passive" and "active". Examples of passive control are such pre-discharge activities as baking and discharge cleaning while the active control mechanisms encompass limiters, magnetic divertors, gas blankets and gettering. Each control mechanism has drawbacks ranging from engineering considerations to physics uncertainties.

6.1 Passive Control

As already discussed in Section (5.4), a high temperature ($\sim$ 450 ^{o}C) baking of the torus wall for an extended period of time will reduce the surface concentration of weakly bound impurity molecules such as carbon and oxygen. In addition to the adsorbed gas, baking increases the outgassing rate of gas trapped in the material during manufacturing and welding processes. However, the more tightly bound molecules ($\sim$ 2 ev) resist thermal desorption and must be removed by energetic particle impact.

It has been determined that discharge cleaning at high surface temperatures (> 300 ^{o}C) and low gas densities is most effective[1]. Both high material temperature and low gas density

reduce the probability that the "scrubbing gas" will become trapped in the surface, thereby increasing the outgassing rate. By discharge cleaning in selected gases such as argon, hydrogen and oxygen, certain contaminants can be selectively removed. For example, carbon can be removed effectively by discharges in oxygen since oxygen and carbon have a great chemical affinity[2]. After the carbon is removed, the oxygen can then be eliminated by discharges in hydrogen. The optimization of discharge cleaning techniques continues to provide increasingly effective pre-discharge impurity control.

6.2 Limiters

Limiters perform two seperate functions: (1) in the event of unstable plasma operation the limiters are expected to protect the first wall by becoming sacrificial dumps for the thermal energy of the plasma, and (2) in a stable discharge the limiter serves as an impurity control scheme by reducing the plasma flux to the wall.

Unstable events range from plasma disruptions,in which the entire discharge terminates, to the generation of intense beams of run-away electrons which have been known to puncture vacuum walls[3]. By careful materials selection and geometric design, limiters can be designed to withstand large thermal fluxes without melting or cracking. "Mushroom" shaped[4] carbon limiters seem to hold great promise.

The impurity control function of the limiter in a stable discharge has been demonstrated in TFR[5]. By increasing the width of the limiter, the oxygen density in the plasma was reduced, apparently confirming the belief that the wall is the major source of light impurities. In addition, the density of heavy impurities was also observed to decrease. Recent results from PLT[6] have demonstrated the advantages of using carbon limiters instead of high Z steel limiters. Figure (6-1) is a comparison of the radiated radial power loss in PLT using carbon and steel limiters. Note that the profiles indicate large core losses for steel limiters and medium edge losses for the carbon limiters. By radiatively cooling the edge, sputtering can be reduced, making the carbon limiter an attractive alternative.

Limiter geometry can be poloidial (encircling the plasma in the θ direction) or toroidal (encircling the plasma in the ϕ direction). From a heat transfer point of view the area of the limiter should be maximized in order to reduce heat loadings. Since a toroidal limiter has an area $(R_o/a) \sim 3$ times greater than a poloidial limiter, the toroidal position is preferred. However, such a configuration can be accused of complicating the maintainance and accessability of the torus.

6.3 Magnetic Divertors

By manipulating the magnetic field topology near the plasma edge, field lines can be made to channel diffusing ions into a

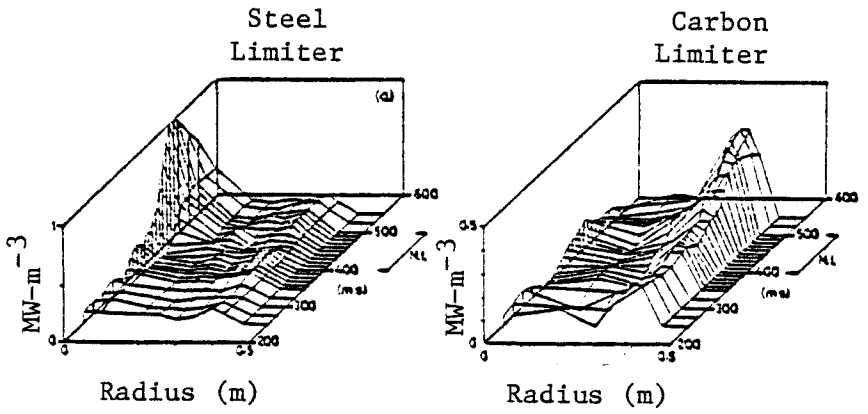

Figure (6-1) Comparison radiative losses as a function of space and time for steel and carbon limiters in PLT [Ref. 6-6].

chamber in which the plasma is neutralized and pumped away. Divertor schemes perform plasma/wall control by: (1) protecting the first wall from plasma outflux, and (2) by shielding the plasma core from wall originated impurities.

The first wall is protected from plasma outflux since cross-field collisional transport is much less than parallel transport (section (5.1)). If the divertor zone is sufficiently wide, the plasma flux to the first wall can be significantly reduced.

The plasma core is shielded from impurity fluxes if neutral wall atoms traversing the divertor zone become ionized. The probability of impurity ionization is a function of electron density and temperature in the divertor zone. Thus, if the zone can be made wide enough, the neutral impurity flux reaching the plasma would be highly attenuated.

Both aspects of divertor action have been observed experimentally[7]. Figure (6-2) is a plot of radiative losses in DIVA for divertor and divertorless operation[8]. Note that the radiative losses in the divertor mode are a factor of ~ 2 less than in the divertorless mode, indicating a combination of first wall protection and impurity shielding.

Unfortunately, the engineering implications of generating the magnetic divertor topology are troublesome. In the case of the poloidal divertor, field shaping coils may be placed inside the toroidal coils, complicating maintainance and accessability.

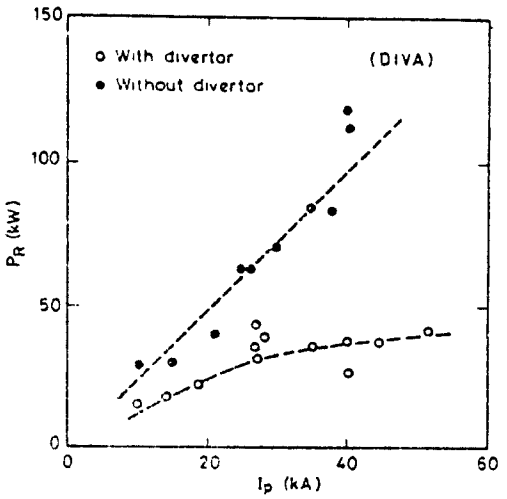

Figure (6-2) Radiated power levels in a DIVA plasma with and without a divertor.

In addition, the shielding of these coils in an intense neutron environment is non-trivial. Bundle divertor coils, while localized on the outside of the torus, are expected to be subjected to large torques. This divertor scheme also destroys the axisymmetry of the plasma, the consquences of this being poorly known at the present time.

Given these engineering problems and physics uncertainties, attention has recently been given to other non-divertor methods of plasma/wall interaction control. These include gas blankets and the gettering of the torus wall. Since the value of these concepts will ultimately have to be determined experimentally, it is premature to view the effective but cumbersome divertor configurations as "a dispensable luxury[9]".

6.4 Gas Blankets

The creation of a cool ($\sim$ 10 ev) and dense ($\sim$ 1 x 10^{14} cm^{-3}) plasma blanket near the plasma edge would: (1) drastically reduce ion sputtering, (2) shield the wall from energetic core-born charge exchange neutrals, and (3) possibly provide a mechanism for fueling the plasma core. The viability of this concept has been subject to scrutiny for a number of years[10-16] and has been incorporated into several reactor scenarios (NUWMAK[17], JET[18]).

In the NUWMAK design, a cool dense gas blanket was created by periodically puffing neutral gas at the plasma edge. This

process created large plasma densities at the edge and large gradients in temperature. These temperature gradients are believed to isolate incoming impurities into a "radiating halo", uniformly distributing some 40% of the alpha power to the first wall, thereby reducing limiter loading and 'hot spots'.

In the JET scenario, low energy neutral beam injection provides the particle source for the blanket. Gibson has shown[18] that a 20 cm thick, 15 ev plasma can be produced by 3 MW of 13 Kev neutral beam injection. Without this blanket Z_{eff} approaches 5 after 1 second while <u>with</u> the blanket $Z_{eff} \sim 1$.

While the experimental verification of all features of gas blankets awaits the next generation of tokamak experiments, hydrogen gas injection into ALCATOR has been correlated to lower edge temperatures and energetic neutral shielding[3]. Such encouraging signs should be tempered, however, by the realization that the gas blanket concept: (1) places a large burden on the gas handling equipment, and (2) oversimplifies the treatment of helium ash. While the gas blanket concept has great appeal, the viability of long burn tokamak operation based upon this scheme awaits a more sophisticated analysis of divertorless operation.

6.5 Gettering

By periodically coating the torus wall with titanium thin films, improvements in tokamak discharge characteristics have

been reported. The effect of gettering is to chemically trap such low Z elements as oxygen in a titanium substrate. Subsequent layers of fresh titanium then effectively bury the oxygen. By reducing the low Z impurity density, higher plasma density, disruption-free discharges have been obtained in ATC[19], PLT[20], and ISX-A[21]. This follows from the apparent correlation between high low-Z edge densities and the onset of current channel shrinkage and eventual disruption.

While this technique is useful in reducing oxygen levels in present day experiments, it remains to be seen whether the alpha ash produced in reactor grade plasmas can be gettered. Brooks[22] has investigated this "helium retention" process and found that substances exist which have helium fluence limits compatible with burn times on the order of minutes. The physics uncertainties of this approach involve the extrapolation of high energy helium implantation experiments down into the ranges characteristic of the plasma edge. In addition, the method and speed of helium purging of the saturated wall material is an area of controversy.

6.6 Summary

This chapter has explored several techniques for the control of plasma/wall interactions. All the schemes investigated are promising. This belief, however, may derive from an ignorance of the relevant physics involved. The next generation of large reactor-like tokamak plasmas will provide experimentalists with the

opportunity to extrapolate these impurity control mechanisms into the reactor regime. The success or failure of these concepts will to a large extent determine how economically and reliably tokamak reactors can be operated, if indeed the solution of the impurity problem is even consistent with tokamak geometry.

CHAPTER 6 REFERENCES

1. R.S. Calder, Vacuum 24, 437 (1974).

2. R.E. Clausing, et al., J. Vac. Sci. Tech. 13, 437 (1976).

3. E. Apgar, et al., in Plasma Physics and Controlled Nuclear Fusion Research (Proc. 6th Conf., Berchtesgaden, 1976), Vol. I, IAEA, Vienna, 247 (1977).

4. R.W. Conn, et al., Problems of Fusion Research, IEEE, San Francisco, 1979.

5. Equipe TFR, Nuc. Fusion 18, 791 (1978).

6. H. Eubank, et al., in Plasma Physics and Controlled Nuclear Fusion Research (Proc. 7th Intl. Conf., Innsbruck, 1978) Vol. I., IAEA, Vienna, 167 (1979).

7. P.E. Stott, et al., in Plasma-Wall Interactions (Proc. Intl. Symp., Julich, 1976), Pergamon Press, Oxford, 39 (1977).

8. Y. Shimomura and H. Maeda, J. Nuc. Mat. 76/77, 45 (1978).

9. J.T. Hogan, in Tokamak Impurity Report, Dept. of Energy report DOE/ET-0001, 24 (December, 1977).

10. G.K. Verboom and J. Rem, Nuc. Fusion 13, 69 (1973).

11. T.F. Volkov, et al., IAEA-CN-34/I9-3.

12. Y. Igitkhanov, et al., Nuc. Fusion 18, 415 (1978).

13. R.A. Gross, Nuc. Fusion 15, 729 (1975).

14. B. Lehnert, Nuc. Fusion 13, 958 (1973).

15. W.J. Goedheer, Reference #7, Pg. 665.

16. G.K. Verboom, Plasma Physics 11, 903 (1969).

17. B. Badger, et al., "NUWMAK - A Tokamak Reactor Design Study", University of Wisconsin, UWFDM-330.

18. A. Gibson, J. Nuc. Mat. 76/77, 92 (1978).

19. P.E. Stott, Nuc. Fusion 15, 431 (1975).

20. K. Bol, et al., Reference #6, Pg. 11.

21. Chapter #5, Reference #33.

22. J.N. Brooks, Proc. of Third Topical Meeting on the Technology of Controlled Nuclear Fusion, Sante Fe, New Mexico, Vol. 2, 873 (1978).

CHAPTER 7

EDGE MODEL FOR TOKAMAK SCRAPE-OFF ZONE

In this chapter a zero dimensional model of the tokamak scrape-off zone is developed which incorporates the relevant atomic and surface physics outlined in Chapter 5. By using this model in conjunction with the one dimensional radial transport code described in Chapter 2, a set of time-dependent, self-consistent boundary conditions is calculated. The impact of plasma-wall interactions on the burn dynamics of a tokamak reactor is then determined quantitatively in Chapter 8.

Plasma simulation work to date has emphasized the development of models for the central region of the plasma discharge. A variety of codes now exist which incorporate most of the essential physical processes present in the core region. By contrast, serious modelling of the 'edge' region is only now receiving detailed attention.

The scrape-off zone, defined as the region between the separatrix or limiter tip and the vacuum wall, is recognized as being critical to the modelling of tokamak discharges since this region is the source of impurities which degrade plasma performance. The complex plasma-wall processes examined in Chapter 5 have a strong effect on the overall density and energy balance by serving as sources and sinks of ions due to diffusion, trapping,

and reflection phenomena. So strong is the coupling between plasma core and edge that in many current devices agreement between simulation and experiment is only achieved by judiciously varying the phenomenological parameters present in crude recycling models. In assessing the impact of plasma-wall interactions on the burn dynamics of future fusion reactors, extrapolation based upon such device-dependent parameters is unwise.

A model of the tokamak scrape-off zone will allow tokamak simulators to: (1) self-consistently evaluate the edge boundary conditions placed upon one dimensional radial transport codes, (2) specify the incoming fluxes of fuel and impurity neutrals with a minimum of adjustable parameters, and (4) estimate the sensitivity of the discharge parameters to plasma-wall interactions.

As discussed in Chapter 3, a knowledge of the plasma boundary conditions is essential if the solutions to the coupled tokamak transport equations are to be believed. The practice of 'guesstimating' time independent edge boundary conditions has to a large extent been based upon an ignorance of the relevant plasma-wall interactions. Such simplifications, however, can force the solutions to the transport equations to unrealistic areas of the solution space which may underestimate or overestimate the engineering requirements of a reactor. The calculation of self-consistent boundary conditions and influxes is thus of critical importance in the design and economic operation of future fusion devices.

Successful control of plasma wall interactions will play a major role in determining the potential of fusion power. As discussed in Chapter 6, several options for such control are under active investigation. In lieu of experiments in the reactor regime, a model for the scrape-off zone would allow researchers to quantify the magnitude and energy of the impurities to be controlled. This information may precipitate the adoption of one particular control scheme or may highlight the inadequacy of all presently known schemes. In short, a model of plasma-wall interactions represents a valuable simulation tool whose power lies in its ability to predict impurity generation in regimes not presently accessable to experiment.

In the next section, a model for the scrape-off zone of a tokamak will be presented as well as a short discussion on the linkage of such a model to a one dimensional radial transport code.

7.1 Boundary Model

The model to be presented is based on the previous work of Hinnov, Fallon and Bishop[1], Hogan[2], and Fielding[3]. The model consists of a series of coupled ordinary differential equations for the density and temperature of the atomic and molecular species present in the scrape-off zone. The species followed include deuterium (D_2^o, D_2^+, D^o, D^+), tritium (T_2^o, T_2^+, T^o, T^+), alpha ash and as an impurity one of several wall

materials (C, Ti, Va, Mo, Fe).

A zero dimensional scheme is chosen because simple continuity agruments are able to provide the approximate spatial profiles of charged particle densities and temperatures. To illustrate, the steady-state equation for ion density in the scrape-off zone can be written as:

$$\vec{\nabla} \cdot \vec{\Gamma} = \vec{\nabla}_{\perp} \cdot \vec{\Gamma} + \vec{\nabla}_{\parallel} \cdot \vec{\Gamma}_{\parallel} = S_i - L_i \qquad (7\text{-}1)$$

where $\Gamma_{\perp}$, $\Gamma_{\parallel}$ represent the cross-field and parallel-field transport fluxes and S_i, L_i model the volumetric sources and losses of ions in the scrape-off zone. Neglecting ionization events and using equation (5-1) for $\Gamma_{\parallel}$, equation (7-1) becomes:

$$\frac{1}{r} \frac{\partial}{\partial r} (r\Gamma_{\perp}) = \frac{-n_i \bar{v}_i}{8\pi r} = \frac{-n_i}{\tau_{\parallel}} \qquad (7\text{-}2)$$

where $\tau_{\parallel}$ is the characteristic time for transport in the parallel direction:

$$\tau_{\parallel} = \frac{8\pi r}{\bar{v}_i} = \pi r \sqrt{\frac{8\pi m_i}{kT_i}} \qquad (7\text{-}3)$$

Represent the cross-field flux by a Ficks' Law expression of the form:

$$\Gamma_{\perp} = -D \left(\frac{\partial n_i}{\partial r}\right) \qquad (7\text{-}4)$$

By substituting equation (7-4) into (7-2), the ion density in the

scrape-off zone obeys the equation:

$$\frac{\partial^2 n_i}{\partial r^2} + \frac{1}{r}\left(\frac{\partial n_i}{\partial r}\right) - \left(\frac{n_i}{2\tau_{\prime\prime} D}\right) = 0. \tag{7-5}$$

The solution to this equation is a zero-th order modified Bessel function:

$$K_o(\alpha r); \quad \alpha = (2\tau_{\prime\prime} D)^{-\frac{1}{2}}. \tag{7-6}$$

The ion density in the scrapeoff zone is then given by:

$$n_i(r) = n_i(a)\,\frac{K_o(\alpha r)}{K_o(\alpha a)}\;; \quad r \geq a \tag{7-7}$$

where $n_i(a)$ is the ion density at the plasma edge.

In a reactor-like device $(\alpha a) >> 1$. In this regime $K_o(\alpha a) \approx K_1(\alpha a)$, so the characteristic length for density decay in the scrape-off zone, δ, can be estimated by:

$$\frac{1}{n_i}\left(\frac{\partial n_i}{\partial r}\right)\Bigg|_{r=a} = \frac{-1}{\delta} \tag{7-8}$$

so: $$n_i(r) = n_i(a)\, e^{+(r-a)/\delta}\;; \quad \delta \geq \sqrt{2D\tau_{\prime\prime}} \tag{7-9}$$

If the diffusion is Bohm-like ($D \sim T/B$), then for reactor-like devices $\delta \geq 5$ cm. In a similar fashion expressions for the temperature decay lenth in the scrape-off zone can be estimated by

solving the continuity equation for ion energy density.

Since the approximate spatial profiles for density and temperature are known, a simple zero dimensional model for average charged particle densities and temperatures can be employed. But is a zero dimensional treatment valid for neutral species such as D_2^o and T^o?

The mean free path of a neutral in the scrape-off zone, λ^o, is defined by

$$\lambda^o = \frac{v^o}{n\langle\sigma v\rangle} \qquad (7\text{-}10)$$

where v^o is the thermal velocity of the neutral, $\langle\sigma v\rangle$ the reaction rate which attenuates the neutral, and n is the background density of target particles. For the 'typical' scrape-off densities and temperatures:

$$T_e \simeq 50 \text{ ev}$$

$$n_e \simeq 5 \times 10^{12} \text{ cm}^{-3}.$$

a neutral deuteron born as a result of a Franck-Condon process ($E \sim 5$ ev):

$$e^- + D_2^o \rightarrow D^+ + D^o + 2e \qquad (7\text{-}11)$$

will have a mean free path:

$$\lambda^o \simeq 13 \text{ cm}; \quad \langle\sigma v\rangle_{ion} \simeq 3 \times 10^{-8} \text{ cm}^3/\text{sec}$$

However, for a neutral diatomic molecule (D_2^o) at the wall temperature (.025 ev), the mean free path is considerably shorter:

$$\lambda^o \underset{\sim}{} .7 \text{ cm}; \quad \langle\sigma v\rangle \underset{\sim}{} 3 \times 10^{-8} \text{ cm}^3/\text{sec}.$$

Since the scrape-off zone is traditionally on the order of 10 cm, a zero dimensional scheme will be appropriate to all but the coldest molecular species. As a future refinement of this model a radial dependence should be included to account for the short diatomic neutral mean free path.

The edge equations involve specie and isotopic coupling due to ionization, dissociation and charge-exchange events. In addition, sources of particles from the plasma core and from the diffusion of wall trapped gas are included. Radiation, charged-particle rethermalization, surface recombination, sputtering, sheath effects, and charged-particle parallel transport have also been incorporated.

The model is self-consistent in that the edge density and temperature as well as the fuel and impurity influxes to the core are evaluated by solving these coupled rate equations subject to the core sources as predicted by the radial transport code. The resulting influxes and edge values determine the boundary conditions for the radial model. This in turn determines the discharge characteristics of the core and the resulting plasma outflux to the scrape-off zone. This clearly demonstrates the iterative

coupling between the plasma core and the plasma-wall interactions in the scrape-off zone.

7.2 Boundary Equations

The zero dimensional rate equations solved in the scrape-off zone for the spatially averaged densities and temperatures are:

$$\frac{d}{dt}(H_2^o) = \sum_{i,j} n_i n_j \langle\sigma v\rangle_{ij} + S_{wall} + S_{gas\text{-}puff} + S_{recomb} \tag{7-12}$$

$$\frac{d}{dt}(H_2^+) = \sum_{i,j} n_i n_j \langle\sigma v\rangle_{ij} + L_{recomb} - L_{''} \tag{7-13}$$

$$\frac{d}{dt}(H^o) = \sum_{i,j} n_i n_j \langle\sigma v\rangle_{ij} - S_{recomb} - H^o/\tau_p \tag{7-14}$$

$$\frac{d}{dt}(H^+) = S_{core} + \sum_{i,j} n_i n_j \langle\sigma v\rangle_{ij} - L_{recomb} - L_{''} \tag{7-15}$$

$$\frac{d}{dt}(N_\alpha) = S_{core} - L_{''} \tag{7-16}$$

$$\frac{d}{dt}(N_z) = \sum_{i,j} n_i n_j \langle\sigma v\rangle_{ij} + S^o_{sput} - L_{''} \tag{7-17}$$

(7-18)

$$\frac{d}{dt}\left(\frac{3}{2} H_2^o T_2^o\right) = \sum_{i,j} n_i n_j \langle\sigma v\rangle_{ij} \left(\frac{3}{2} T_i - \frac{3}{2} T_j\right) + S^*_{recomb} - \xi/\tau_p$$

(7-19)

$$\frac{d}{dt}\left(\frac{3}{2} H_2^+ T_2^+\right) = \sum_{i,j} n_i n_j \langle\sigma v\rangle_{ij} \left(\frac{3}{2} T_i - \frac{3}{2} T_j\right) + \sum_i Q_{H_{2,j}^+} - L^*_{recomb} - L^*_{''}$$

$$\frac{d}{dt}\left(\frac{3}{2} H^{o}T^{o}\right) = \sum_{i,j} n_i n_j \langle\sigma v\rangle_{ij} \left(\frac{3}{2} T_i - \frac{3}{2} T_j\right) - \xi/\tau_e + S^{*}_{recomb} \quad (7\text{-}20)$$

(7-21)

$$\frac{d}{dt}\left(\frac{3}{2} H^{+}T^{+}\right) = \sum_{i,j} n_i n_j \langle\sigma v\rangle_{ij} \left(\frac{3}{2} T_i - \frac{3}{2} T_j\right) + S^{*}_{core} + \sum_{i} Q^{+}_{H,j} - L^{*}_{\shortparallel}$$

(7-22)

$$\frac{d}{dt}\left(\frac{3}{2} n_e T_e\right) = \sum_{i,j} n_i n_j \langle\sigma v\rangle_{ij} \left(\frac{3}{2} T_i - T_j\right) - L_{rad} - L^{*}_{\shortparallel} + S^{*}_{core} + \sum_{j} Q_{T_e,j}$$

where:

S_{core} = particle source from core

S^{*}_{core} = power source from core

$L_{\shortparallel}$ = particle loss in parallel direction

$L^{*}_{\shortparallel}$ = power loss in parallel direction

n/τ_p = neutral particle flux to core

ξ/τ_e = neutral power flux to core

$Q_{i,j}$ = rethermalization between specie i and j

L_{rad} = radiative loss of power

L_{recomb}, S_{recomb} = loss/source of particles due to recombination at wall

S_{wall} = source of gas diffusing from wall

S^{o}_{sput} = sputtering source of neutral impurities

$S_{gas\text{-}puff}$ = neutral source due to gas puffing

For compactness, the above rate equations have been written in terms of hydrogen densities and temperatures. However, since the model follows deuterium and tritium as seperate species, equations (7-12) - (7-22) represent 17 coupled ordinary differential equations plus 2 equations for alpha particles and impurities.

In the following sections, the various terms in these equations will be examined and the models used to evaluate them discussed.

7.3 Atomic Physics

After an extensive literature search[4-11], 19 hydrogenic reactions were included in the model and represent the most probable reaction channels at characteristic scrape-off temperatures (Table (7-1)). Treating deuterium and tritium as separate species and allowing for inter specie and isotopic reactions, the number of reactions increases from 19 to 55. Knowing the raw experimental cross-section data or analytic fits to such data, the 55 reaction rates $\langle\sigma v\rangle$ were obtained by numerically integrating the expression:

$$\langle\sigma v\rangle = \sqrt{\frac{8}{\pi\mu}} \left(\frac{1}{kT}\right)^{3/2} \int_0^\infty E\,\sigma(E)\, e^{-E/kT}\, dE \qquad (7\text{-}23)$$

derived by assuming two interacting Maxwellian species at a common temperature T[12].

The model initially starts with all non-molecular specie densities set to small values. As cool molecular gas is admitted into the scrape-off zone either by gas puffing, wall diffusion or molecular recombination at the wall, it interacts via the 55 possible reaction channels and 'burns' from molecular neutrals to molecular ions to monoatomic neutrals to monoatomic ions.

The reaction rates, being complicated functions of temperature (and hence, space), are not spatially averaged. Rather they are evaluated at the spatially averaged temperature. Exact calculations have shown that except for very low temperatures (i.e. < 10 ev) the following holds:

$$\frac{1}{d}\int_{d}^{o} \langle\sigma v\rangle\ (T(x))\ dx \approx \langle\sigma v\rangle\ (\bar{T}) \qquad (7\text{-}24)$$

where d is the scrape-off width and $\bar{T}$ is the spatially averaged temperature. This approximation is justified by the observation that the cross-sections for these 55 reactions are known only to within $\pm$ 20%.

7.4 Impurities

In section (2.5), the coronal equilibrium model for impurity radiation based upon the 'average ion' concept was examined and found to be inadequate near the plasma edge. Recall that coronal equilibrium is valid if impurity diffusion can be neglected in comparison with atomic events such as ionization and recombination.

The charged impurities in the scrape-off zone experience large parallel losses in a time characterized by $\tau_{\parallel}$ ($\sim 10^{-4}$ seconds). In addition the rapid recycling of core diffusing impurities in the scrape-off zone violates the coronal assumption. Therefore a modified version of the non-coronal model of Post[13] has been employed to evaluate impurity radiation and density in the edge region.

A set of coupled ordinary differential rate equations for the number density of each charge state of the impurity is solved in response to ionization and recombination events. Sputtered atoms from the wall and limiter represent a source in the neutral impurity rate equation, while the impurity ions diffusing from the core to the shadow act as a source of ions. Finally, the parallel transport of charged impurities in the edge region serves as a loss mechanism for impurities at the rate:

$$-(n_z/\tau_{\parallel}). \qquad (7\text{-}25)$$

Knowing the number density of each charge state (0, 1, 2...Z), the energy levels of each species and the various rate coefficients for atomic transitions, the time dependent radiative losses can be calculated. As an example of the impact of a non-equilibrium calculation, consider the integrated radiative losses for an oxygen atom in a 1 kev plasma with electron denstiy 10^{13} cm^{-3} and oxygen density 10^{11} cm^{-3}. In 2×10^{-2} seconds the

instantaneous radiative rates for both the equilibrium and non-equilibrium models are equal. However, by integrating the instantaneous radiative rates over this interval in time, the non-equilibrium calculation predicts:

$$\frac{E_{NON\text{-}EQUIB}\ (kev/ion)}{E_{EQUIB}\ (kev/ion)} \simeq 17$$

a substantial increase over the standard coronal equilibrium calculation.

Thus the non-coronal equilibrium calculation is a critical component in the modelling of the scrape-off zone.

7.5 Wall Concentration Model

The reflection of energetic ions and neutrals from the wall is modelled using the reflection coefficients described in section (5.2). Those particles not reflected from the wall slow down in the lattice and thermalize. Crude models of recycling usually neglect this gas. However this gas diffuses back into the scrape-off zone at a rate determined by wall concentration, temperature and fluence. The modelling of this non-negligible source of neutral gas is based on the Ficks' Law model of Baskes[14].

Particles of energy E which are not reflected at the wall undergo a series of binary collisions as they thermalize in the material. Let this spatial implantation profile be defined as G(x). The time rate of change of the concentration of this

mobile gas C(x,t) in response to diffusion, trapping and thermal detrapping is given by:

$$\frac{\partial C(x,t)}{\partial t} = D(T) \frac{\partial^2 C}{\partial x^2} - \frac{\partial C_T(x,t)}{\partial t} + G(x) \qquad (7\text{-}26)$$

where D(T) is the diffusivity of the mobile gas in the material at temperature T and $C_T(x,t)$ represents the concentration of atoms caught in lattice imperfections ("traps"). These traps can be the result of manufacturing processes or of radiation damage.

The concentration of atoms caught in these traps obeys the equation:

$$\frac{\partial C_T(x,t)}{\partial t} = \frac{D(T)\ C(x,t)\ C_T^e(x,t)}{\lambda^2} - C_T(x,t)\ e^{-E_T/kT}\ \nu_o \qquad (7\text{-}27)$$

where λ represents the thermal detrapping jump distance, ν_o the detrapping frequency ($\sim 10^{13}$/sec), and E_T the trap binding energy. C_T^e represents the concentration of empty traps and is related to the concentration of full traps C_T by the expression:

$$C_T^e = C_T^o - C_T \qquad (7\text{-}28)$$

where C_T^o represents the concentration of all traps (initially empty). The diffusivity D is related to the bulk material temperature T through the relation:

$$D = D_o\ e^{-Q_D/kT} \qquad (7\text{-}29)$$

where Q_D represents the migration energy and D_o a constant. Both Q_D and D_o are determined from experiment. For tritium diffusion in a stainless steel sample, for example, $Q_D \simeq .6$ eV and $D_o \simeq .12$ cm^2/sec[15].

This set of nonlinear partial differential equations is solved numerically by approximating equations (7-26) and (7-27) by N spatially finited differenced ordinary differential equations in time, N being the number of spatial grid points defining the diffusion region. This system of coupled differential equations is solved using the Gear method[16]. The rate at which gas diffuses from the wall into the scrape-off zone is then determined from the concentration gradient at the surface (Fig. (7-1)).

A calculation based on monoenergetic range theory[17] is performed to determine the spatial distribution of implanted atoms. Given a particle of initial energy E, the model predicts a gaussian implantation profile of the form:

$$G(x) = \frac{1}{\sqrt{2\pi}\,\sigma} e^{-\frac{x^2}{2\sigma^2}} \qquad (7\text{-}30)$$

where x represents the distance from the peak of the distribution and σ denotes the width of the gaussian. G(x) is normalized to unity.

However, since the incident flux is representative of a Maxwellian distribution, the range calculation has been modified to reflect this. The distribution is divided into a number of

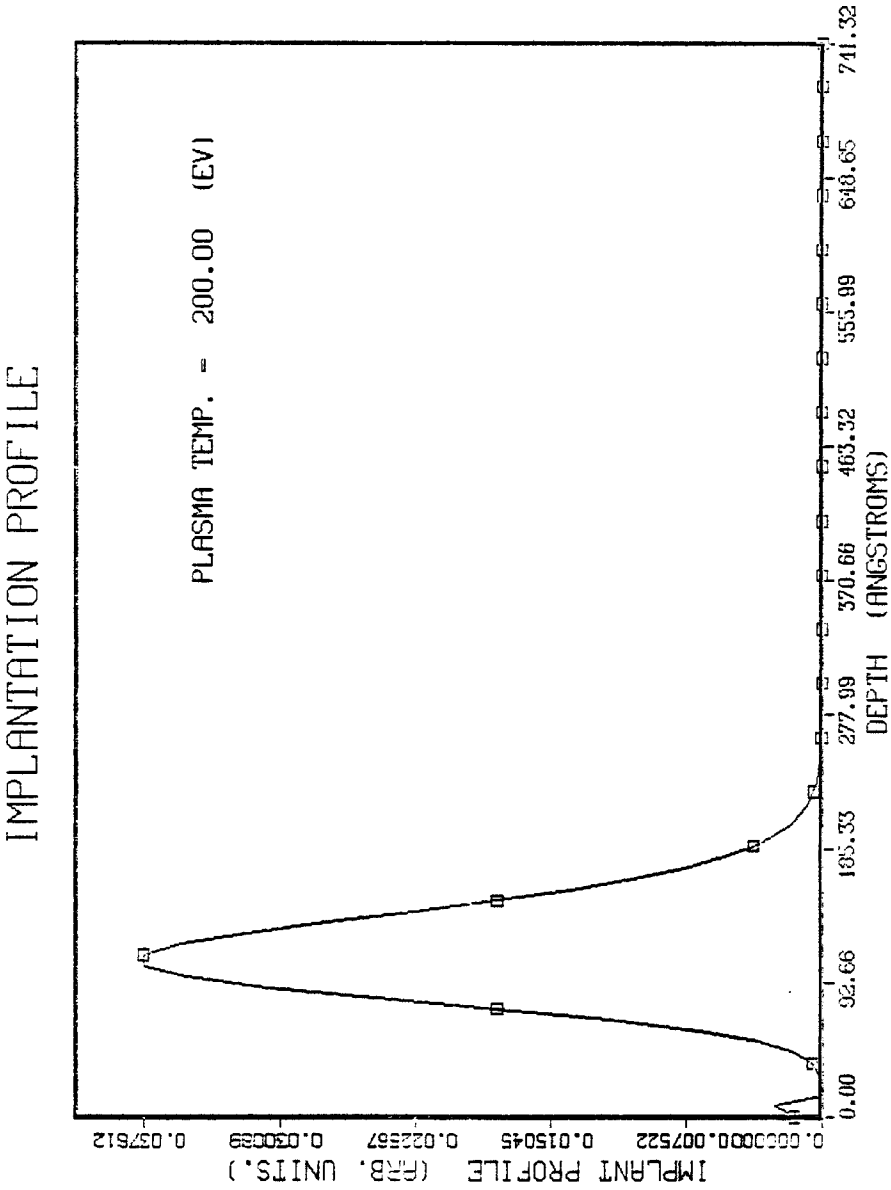

Figure (7-1) Implantation profile characteristic of a 200 eV deuterium plasma incident on a steel surface.

'monoenergetic' energy groups and a separate range calculation is performed for each group. The normalization for each gaussian is equal to the probability that the particle in question would be found between energy E and E + dE in the distribution. The net profile is obtained by summing the individual gaussians. The result of such a calculation is found in Figure (7-1) in which G(x) is plotted versus implantation depth for a 200 eV deuterium plasma incident on a steel surface. Note that typical peak depths are in the tens of angstroms range.

Using such a profile, the wall concentration model predicts the release rate of trapped gas as a function of bombardment time. Figure (7-2) is a plot of the normalized release rate for deuterium incident on a steel target as a function of time. Note that after $\sim$5 seconds, the released flux is only 90% of the incident flux ($1 \times 10^{16}/cm^2$ -sec). This source of gas is a source term in the molecular density balance equations for both deuterium and tritium. The radioactive decay of tritium in the wall has been neglected.

7.6 Sputtering

Sputtering of the wall and limiter is assumed to occur only by D, T, alphas and impurity impact. These fluxes arise both from the core and shadow regions. As described in section (5.5), light ion sputtering yields have been modelled using the

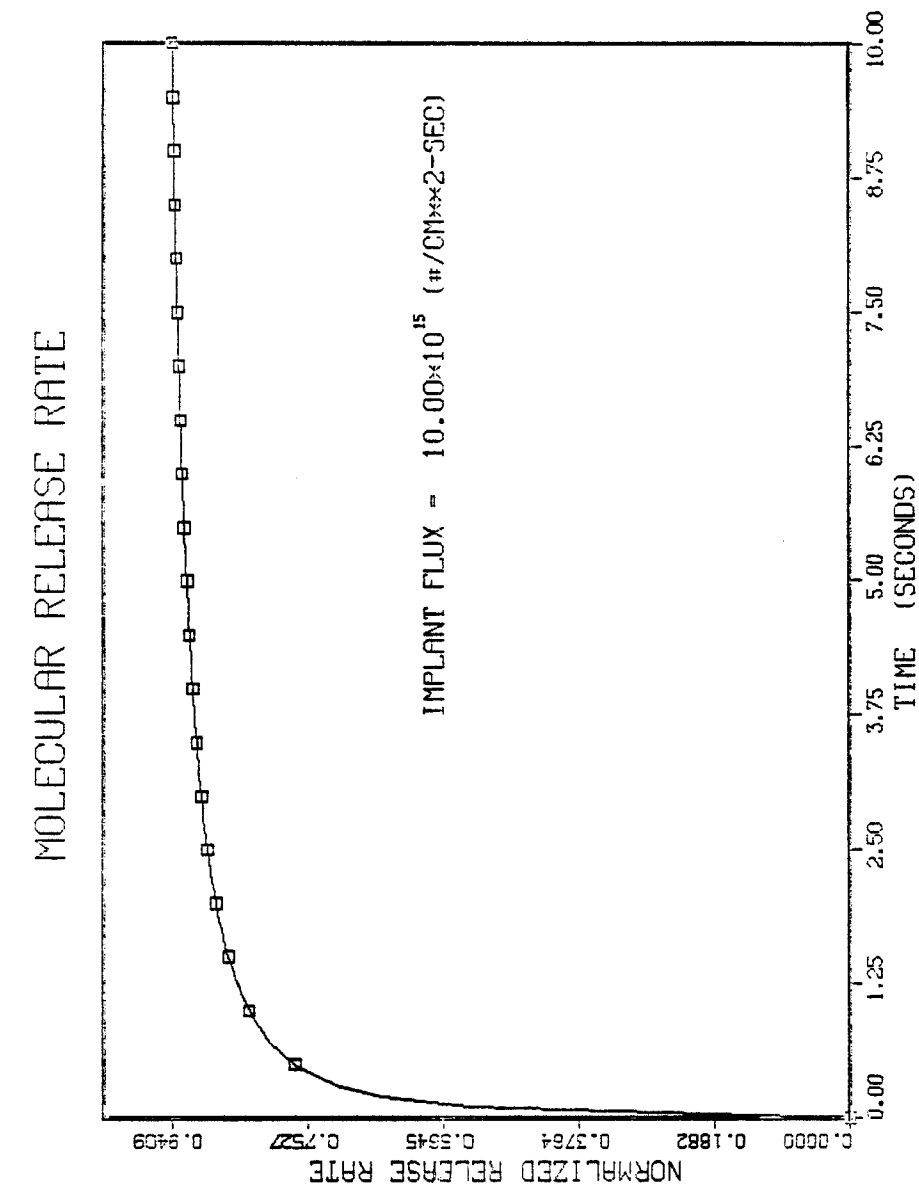

Figure (7-2) Molecular release rate of trapped gas in wall as a function of time.

expression developed at Garching while the self-sputtering coefficients are those of Smith.

Since the fluxes are characteristic of a Maxwellian distribution of energies, the yield coefficient has been averaged over the energy distribution of the incident flux:

$$\bar{S}(E) = \frac{\int S(E)\ f(E)\ dE}{\int f(E)\ dE} \qquad (7\text{-}31)$$

where for a Maxwellian:

$$f(E) \propto \sqrt{E/kT}\ \ e^{-E/kT} \qquad (7\text{-}32)$$

The presence of an ion accelerating sheath at the limiter/plasma interface has been taken into account in the calculation of limiter sputtering. The expression for sheath potential is given in section (5.3).

In order to model the phenomena of impurity redeposition after sputtering, a phenomenological parameter has been included in the sputtering model. It allows the specification of a fraction f of the calculated flux to redeposit on the surface. If f = .9, then 90% of all atoms sputtered from the surface will immediately redeposit upon the wall and limiter. Those neutral impurity atoms not being redeposited are a source term in the impurity density balance equations solved by the non-coronal equilibrium radiation package.

7.7 Parallel Transport

Charged-particle parallel transport to the limiter or divertor plate is modelled by assuming free-streaming ions at a sound speed characterized by the local ion temperature. The particle and energy balance equations have loss terms of the form:

$$\text{Particle:} \quad -n_j/\tau_{\parallel} \tag{7-33}$$

$$\text{Energy:} \quad -2kT_j(n_i/\tau_{\parallel}) \tag{7-34}$$

where $\tau_{\parallel}$ is the characteristic time for parallel transport. The loss of electrons is modelled by imposing charge neutrality on field lines.

7.8 Assumptions

Since a reliable data base for the more complex plasma-wall interactions is incomplete at this time, the following processes which may play a role in recycling have not been included in the scrape-off model. These include the presence of oxide layers, the effect of wall erosion and radiation damage on the wall concentration model, the presence of water and hydrocarbons on the torus wall, chemical sputtering, the effect of sample history on the trapping properties of the wall and the synergistic effects of simultaneous hydrogenic and helium implantation. Inclusion of such effects must await the creation of a set of reliable prescriptions for their behavior.

7.9 Solution Scheme

The coupled ordinary differential equations describing the time evolution of the spatially averaged densities and temperatures are solved using the DRODE[18] differential equation package developed at Sandia, Lawrence Livermore and Los Alamos Laboratories. In response to the source terms from the core and wall as well as the loss terms due to atomic events and parallel transport, the system of equations is carried to a quasi-equilibrium. Typically this is in the range $10^{-4} \rightarrow 10^{-3}$ seconds. Having obtained the spatially averaged parameters and assuming that the charged particle densities and temperatures can be approximated by the expression (section 7.1):

$$\Psi_j(r) = \Psi_j(a)\, e^{+(r - a)/\delta_j};\ r \geq a \qquad (7\text{-}35)$$

where $\delta_j \simeq \sqrt{2D\tau_{\parallel}}$, the boundary conditions for the core calculation, $\Psi_j(a)$, can be determined. As an economy measure, the core calculation is advanced in time with these boundary conditions fixed until the core outflux has changed sufficiently to warrant another quasi-equilibrium edge calculation.

The diffusion coefficient characterizing cross-field transport in the scrape-off zone is chosen to be Bohm-like, i.e.

$$D = 6.25 \times 10^6 \left(\frac{T}{B}\right) * f \quad (cm^2/sec) \qquad (7\text{-}36)$$

where T is the plasma temperature in ev, B the magnetic field in gauss and f a variable in the range:

$$.1 \leq f \leq 1$$

Measurements in the scrape-off zone of TFR-400[19] have yielded estimates of D consistent with Bohm diffusion.

In the next chapter the results obtained by coupling this edge model with the one dimensional radial model of Chapter 2 will be presented.

TABLE (7-1)

HYDROGENIC ATOMIC REACTIONS FOLLOWED IN THE SCRAPE-OFF ZONE.

$e + H$	$\rightarrow$	$H^+ + 2e$
$e + H_2$	$\rightarrow$	$H_2^+ + 2e$
$e + H_2$	$\rightarrow$	$H + H^+ + e$
$e + H_2$	$\rightarrow$	$2H + e$
$e + H_2^+$	$\rightarrow$	$H + H^+ + e$
$e + H_2^+$	$\rightarrow$	$2H^+ + 2e$
$e + H_2^+$	$\rightarrow$	$2H$
$H^+ + H$	$\rightarrow$	$H^+ + H$
$H^+ + H_2$	$\rightarrow$	$H_2^+ + H$
$H_2^+ + H_2$	$\rightarrow$	$H_2^+ + H_2$
$H^+ + H_2$	$\rightarrow$	$H^+ + H_2^+ + e$
$H_2^+ + H_2$	$\rightarrow$	$2H_2^+ + e$
$H^+ + H$	$\rightarrow$	$2H^+ + e$
$H_2^+ + H$	$\rightarrow$	$H^+ + H_2$
$H_2^+ + H$	$\rightarrow$	$H^+ + H_2^+ + e$
$H_2^+ + H_2$	$\rightarrow$	$H^+ + H + H_2$
$H_2^+ + H_2$	$\rightarrow$	$2H^+ + H_2 + e$
$H_2^+ + H$	$\rightarrow$	$H^+ + 2H$
$H_2^+ + H$	$\rightarrow$	$2H^+ + H + e$

CHAPTER 7 REFERENCES

1. E. Hinnov, et al., Plasma Physics 10, 291 (1968).

2. J.T. Hogan, Plasma Wall Interactions, Proc. Symp. Jülich 1976 (Pergamon Press, Oxford), p. 155.

3. S.J. Fielding, et al., J. Nucl. Mat. 76/77, 273 (1978).

4. E.L. Freeman, E.M. Jones, Culham Report CLM-R137 (1974).

5. E.M. Jones, Culham Report CLM-R175 (1977).

6. C.A. Finan, Lawrence Livermore Report UCRL-51805 (1976).

7. B. Peart, K. Dolder, J. Phys. B: Atom. Mol. Phys. 5, 1554 (1972).

8. B. Peart, K. Dolder, J. Phys. B: Atom. Mol. Phys. 7, 236 (1974).

9. A. Riviere, D. Sweetman, Proc. Phys. Soc. 78, 1215 (1961)

10. D. Vance, T. Bailey, J. Chem. Phys. 44, 486 (1966).

11. A. Riviere, Nuc. Fus. 11, 363 (1971)

12. J.R. Lamarsh, Introduction To Nuclear Reactor Theory, (Addison-Wesley, 1972), p. 255.

13. Reference (2-6).

14. M.I. Baskes, Sandia Laboratory Report SAND80-8201 (January, 1980).

15. K. Wilson, M. Baskes, J. Nucl. Mat. 76/77, 291 (1978).

16. C.W. Gear, Numerical Initial Value Problems in Ordinary Differential Equations (Prentice Hall, New Jersey, 1971).

17. D.K. Brice, Sandia Laboratory Report SAND75-0622, (July, 1977).

18. M. Baskes, private communication; also see Reference #16.

19. G. Staudenmaier, P. Staib, G. Venus, J. Nucl. Mat. 76/77, 445 (1978).

CHAPTER 8

NUMERICAL SOLUTIONS TO TOKAMAK TRANSPORT

In this chapter solutions to the one dimensional tokamak fluid equations of Chapter 2 and the zero dimensional edge equations of Chapter 7 are described. Model calculations are presented which tend to support the concept of impurity control using a gas blanket. However, before any results are presented, a brief examination of the implications of various core transport coefficients and time-dependent boundary conditions will be discussed.

8.1 Model-Imposed Limitations on Numerical Solutions

The efficient numerical solution of the tokamak transport equations is highly sensitive to a number of parameters. As mentioned in Chapter 3, spatial mesh and timestep considerations are important if fast and accurate simulations are to be made. In addition, the time behavior of the boundary conditions at the plasma edge are of fundamental importance. If, for example, the edge densities or temperatures change at each timestep, the radial code will become "bogged down" near the edge by performing several iterations and time-step reductions. Unfortunately, the speed of the entire calculation is then being determined by the outermost 1% of the plasma.

One immediate consequence of this sensitivity to edge boundary conditions is that the 1D analysis of plasma behavior from ohmic startup to ignition to equilibrium becomes prohibitive for all but time-independent boundary conditions. While fixing the edge boundary conditions at "representative" values provides a quick and dirty solution to this dilemma, it may alter the character of the discharge by suppressing or enhancing certain features at the edge which have global consequences. An excellent illustration of this potential problem arises in the numerical simulation of tokamak gas blankets.

As described in section (6.4), the existence of a cool, dense layer of plasma at the edge may have important impurity control implications. By being cool, most of the plasma ions will have energies below the sputtering threshold of the limiter and wall material, thereby reducing the introduction of performance degrading impurities into the plasma. If the blanket is optically thick enough to energetic core-born neutrals, then the charge-exchange spectrum to the liner will be representative of the plasma edge temperature. Finally, this cool, dense layer of plasma may serve as a barrier to incoming impurities by trapping them at the edge. If this trapped impurity concentration is great enough, a significant fraction of the alpha power generated in the plasma may be radiated to the first wall, thereby reducing the power lost by the plasma through transport. If the creation

of this blanket is achieved by the introduction of periodic short bursts of neutral gas at the plasma edge, clearly the specification of static boundary conditions in inappropriate.

To remedy this situation, more dynamic boundary conditions must be used. However, since experience has shown that time-dependent boundary conditions are the source of serious numerical hangups, a simulation can only be carried out for a short time, typically less than the time required for the plasma to reach a steady-state (Figure (8-1,2)). Obviously the tradeoff here is between a short but more realistic simulation which says nothing about equilibrium values and a fast simulation which while describing an equilibrium may not be describing the equilibrium consistent with the real boundary conditions. It has been the philosophy of this work to pursue the former scheme, since the limitations of this approach are purely numerical and do not involve fundamental physics assumptions.

However, even if a numerical "fix" was developed which would speed the calculation, if the plasma transport coefficients used in the simulation are based on empirical scaling, then an equilibrium solution may in principle not exist. Several parameter studies using these empirical scalings have concluded that the central energy confinement is so good that the core is overignited and runs away in temperature while because conduction from core to edge is low, the plasma bulk temperature doesn't increase. Of course physically such a temperature excursion cannot continue

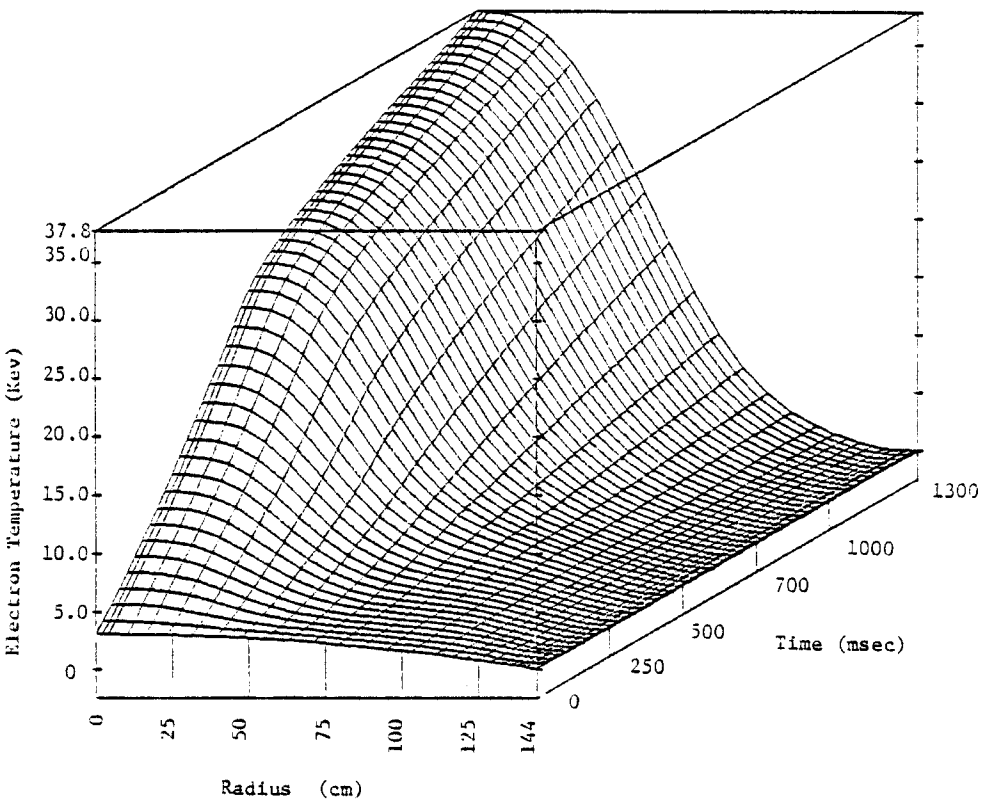

Figure (8-1) 3D plot of electron temperature demonstrating non-equilibrium.

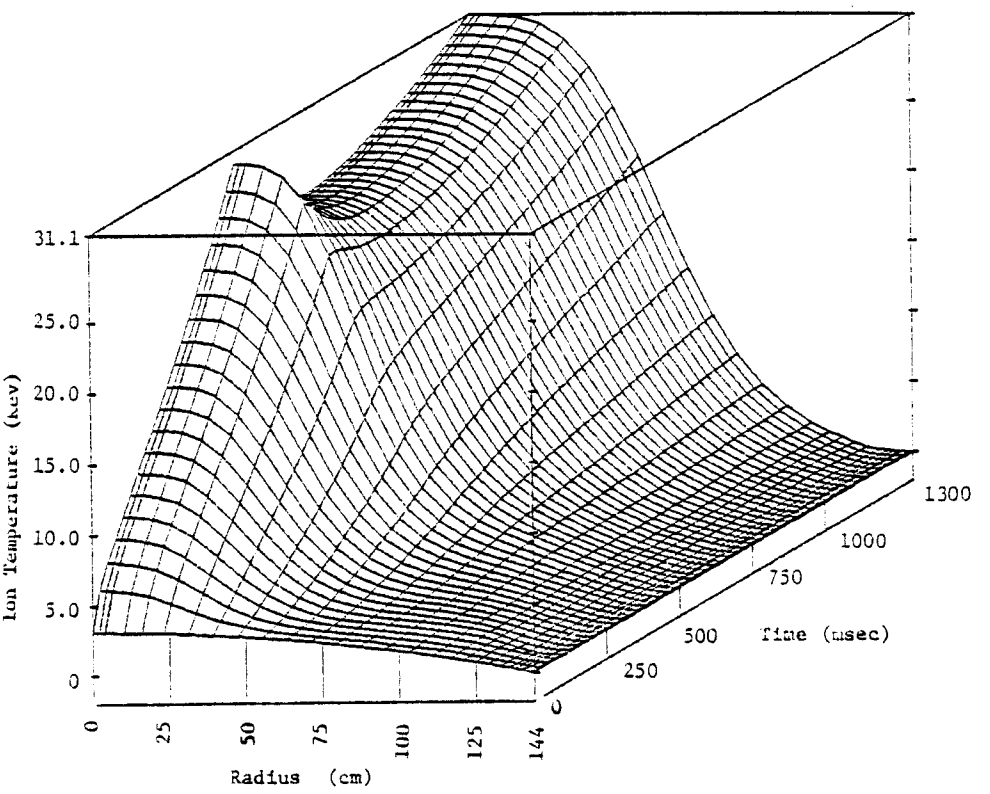

Figure (8-2) 3D plot of ion temperature demonstrating non-equilibrium.

indefinitely since at some point a beta limit will be reached or enhanced heat transport due to MHD activity out of the $q(r) < 1$ surface will flatten the temperature profiles.

Since the development of such models is only now being attempted, the philosophy of this work has been to truncate the simulation when the plasma core begins to enter such an unrealistic regime of central temperature. In order to ease the run-away problem, the calculations in this chapter are based upon diffusion coefficients whose values have been increased by an arbitrary multiplicative constant, typically in the range 2 - 4. Since these coefficients are known only to within a factor of 5 to begin with, such modifications are, while unappealing to the purist, routinely employed in the numerical simulation of plasma transport.

Therefore, due to both numerical (boundary conditions) and physical (diffusion coefficients) constraints, only quasi-equilibrium results will be presented here.

8.2 Gas Blanket Simulations

In this section results are presented for the simulation of a gas blanket in the NUWMAK conceptual reactor. The physical parameters pertinent to this device are listed in Table (8-1). 100 MW of RF power is injected into the plasma (70% to ions and 30% to electrons) for 1/2 second where the spatial absorption

profile is legislated to be a gaussian peaked on axis. Starting at 100 msec, periodic gas puffs are introduced at the edge every 200 msec, the magnitude of these fluxes into the plasma being an output of the edge model and a function of the assumed molecular gas flow rate. Plasma transport coefficients in the core are taken to be (3) *neoclassical + PLT empirical while diffusion in the scrape-off zone is characterized as Bohm-like. The impurity followed in the calculation is taken to be iron. The limiter (of 10 cm width) is assumed to direct about 30% of all incident particles into a pumping port, thereby removing them from the calculation.

Two gas puffing scenarios are considered. In case A (low gas injection rate), 5E22 DT molecules/sec are admitted to the scrape-off zone during each puff while in case B (high gas injection rate), 1E23 DT molecules/sec are injected. Table (8-2) is a list of the results at 1200 msec into the discharge for each case. Figures (8-3,9) and (8-10,16) are plots of density and temperature profiles as a function of time for case A and B, respectively.

An examination of Table (8-2) reveals the following observations: (1) the higher influx of gas in case B lowers the edge and shadow temperatures by factors of between 2 and 3 over case A. The achievement of these low edge temperatures is a first step towards the creation of a gas blanket useful in

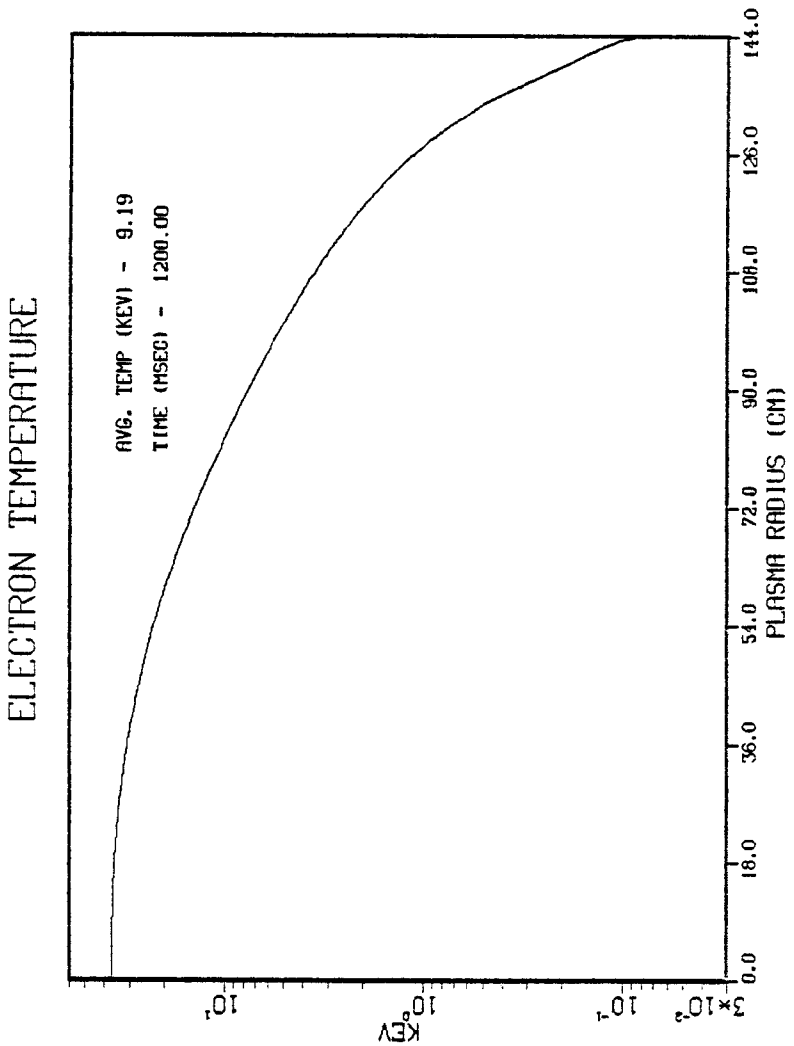

Figure (8-3) Case A: Electron temperature vs. plasma radius.

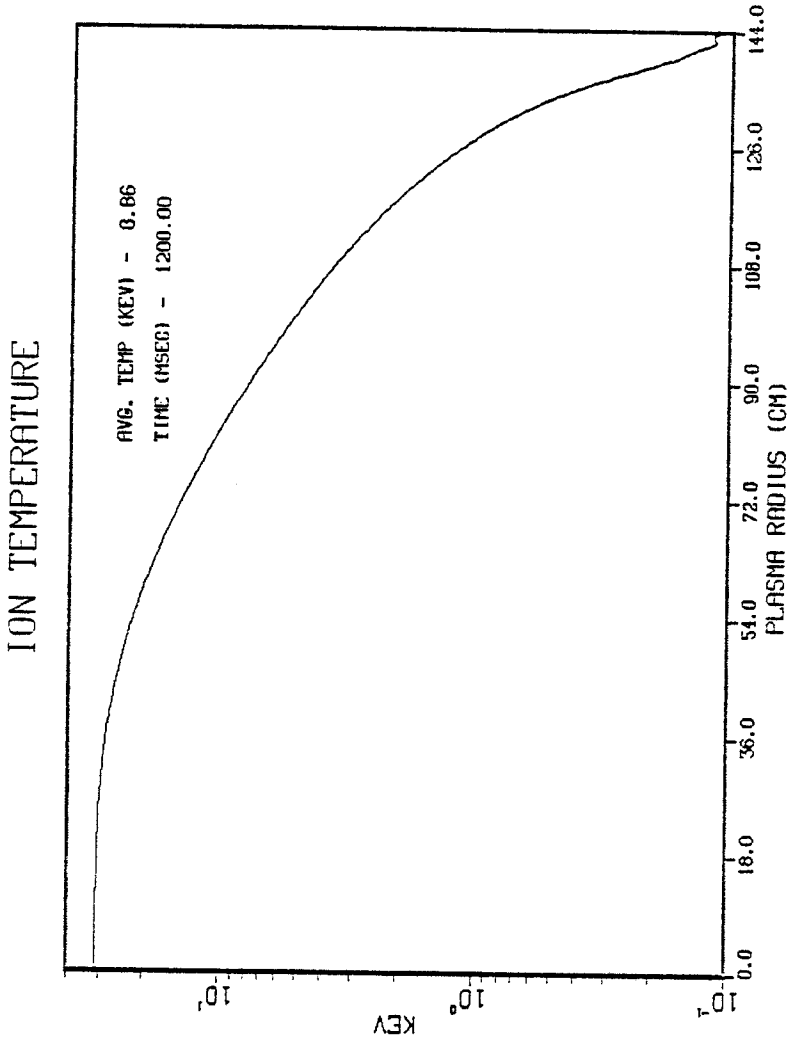

Figure (8-4) Case A: Ion temperature vs. plasma radius.

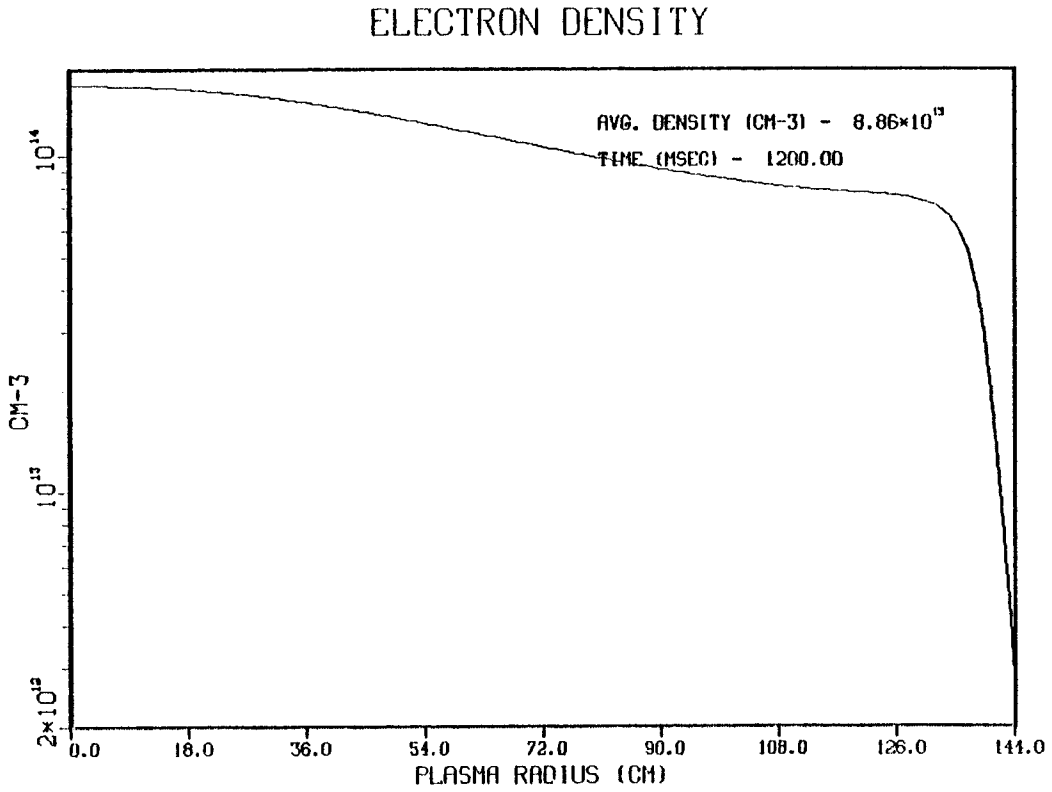

Figure (8-5) Case A: Electron density vs. plasma radius.

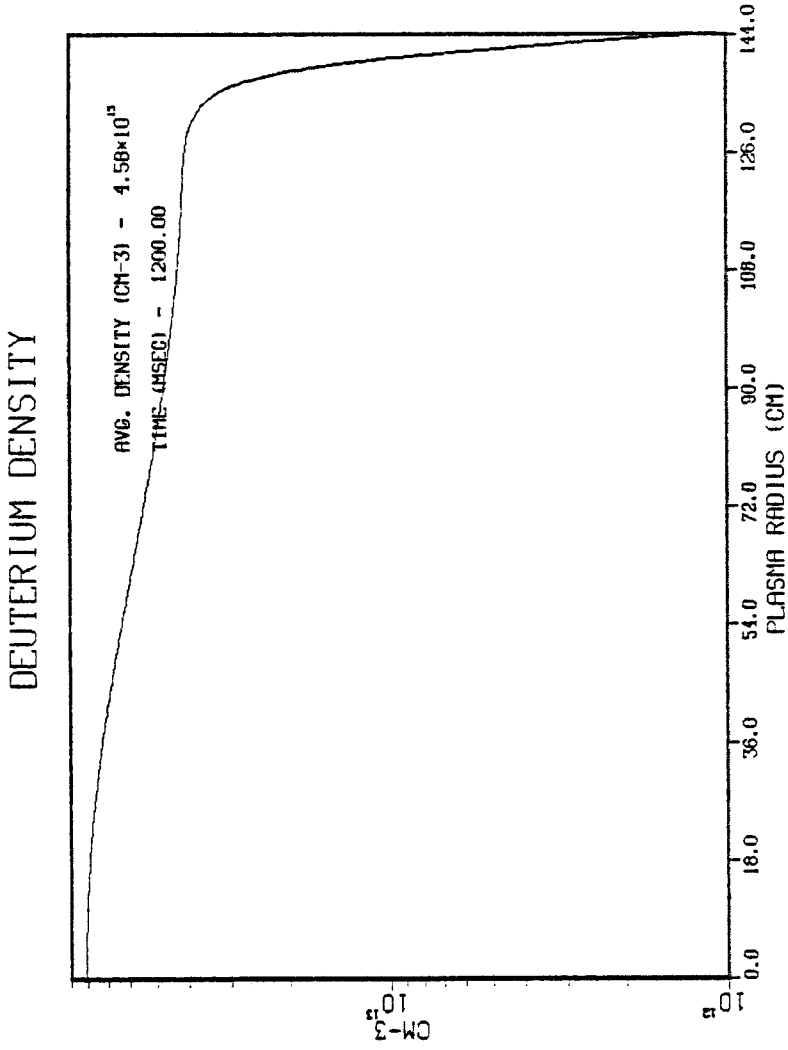

Figure (8-6) Case A: Deuterium density vs. plasma radius.

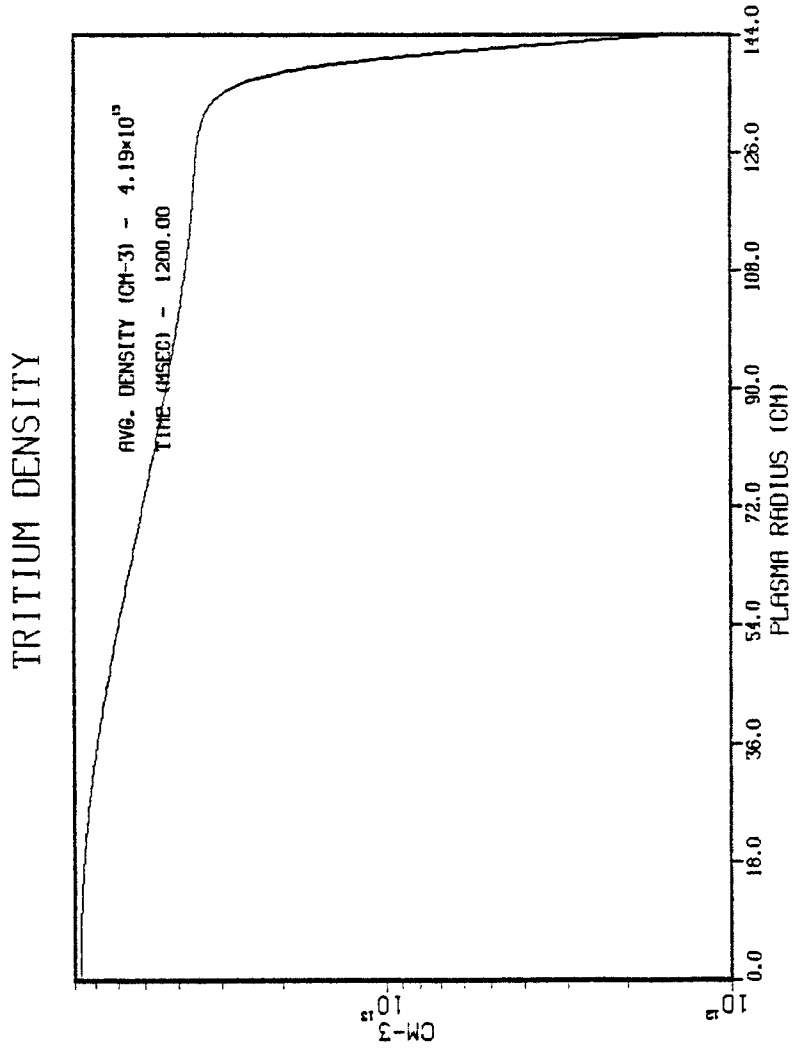

Figure (8-7) Case A: Tritium density vs. plasma radius.

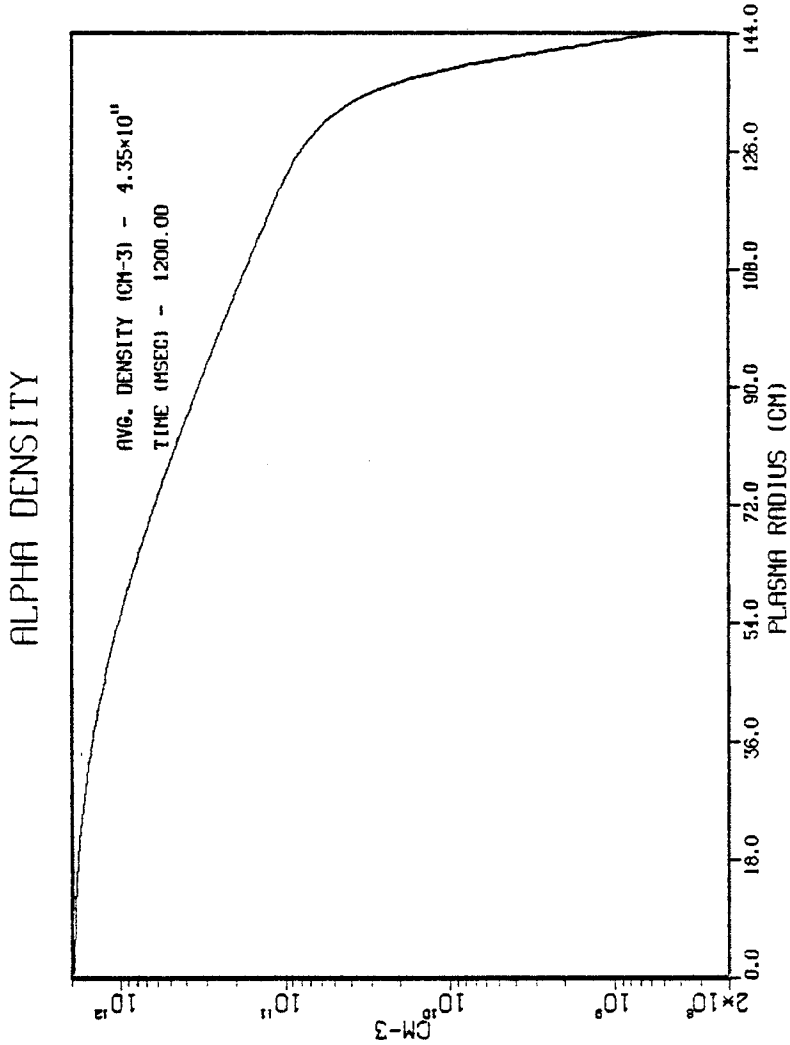

Figure (8-8) Case A: Alpha temperature vs. plasma radius.

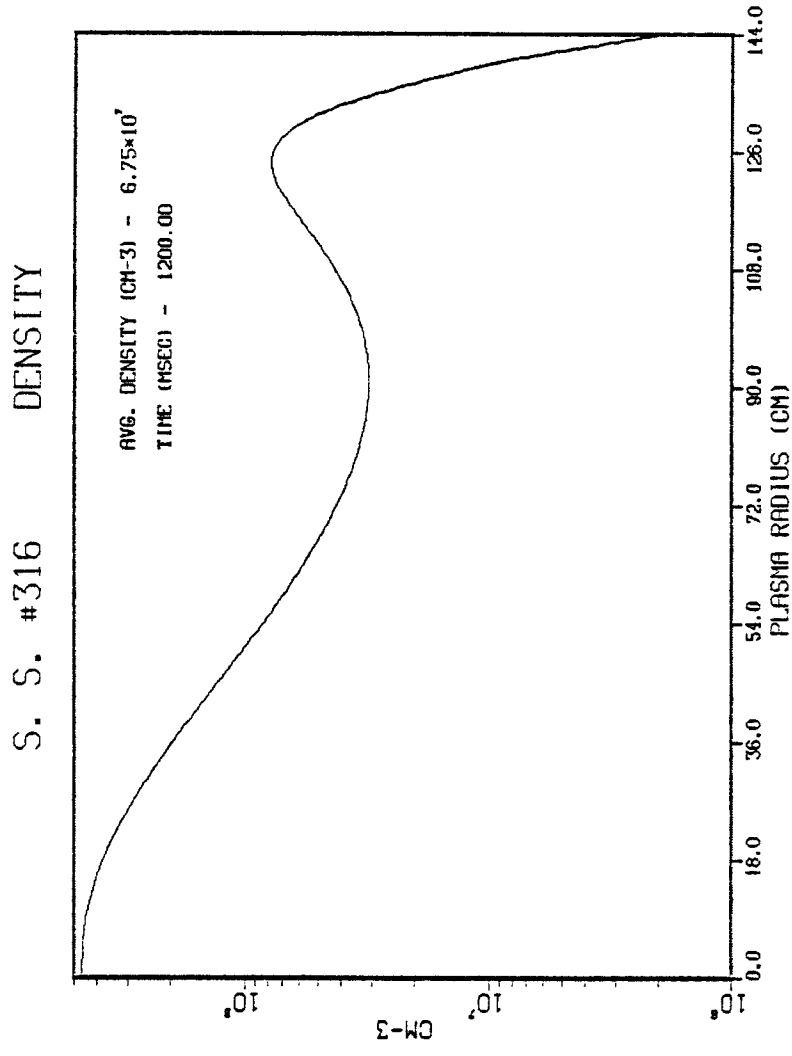

Figure (8-9) Case A: Impurity temperature vs. plasma radius.

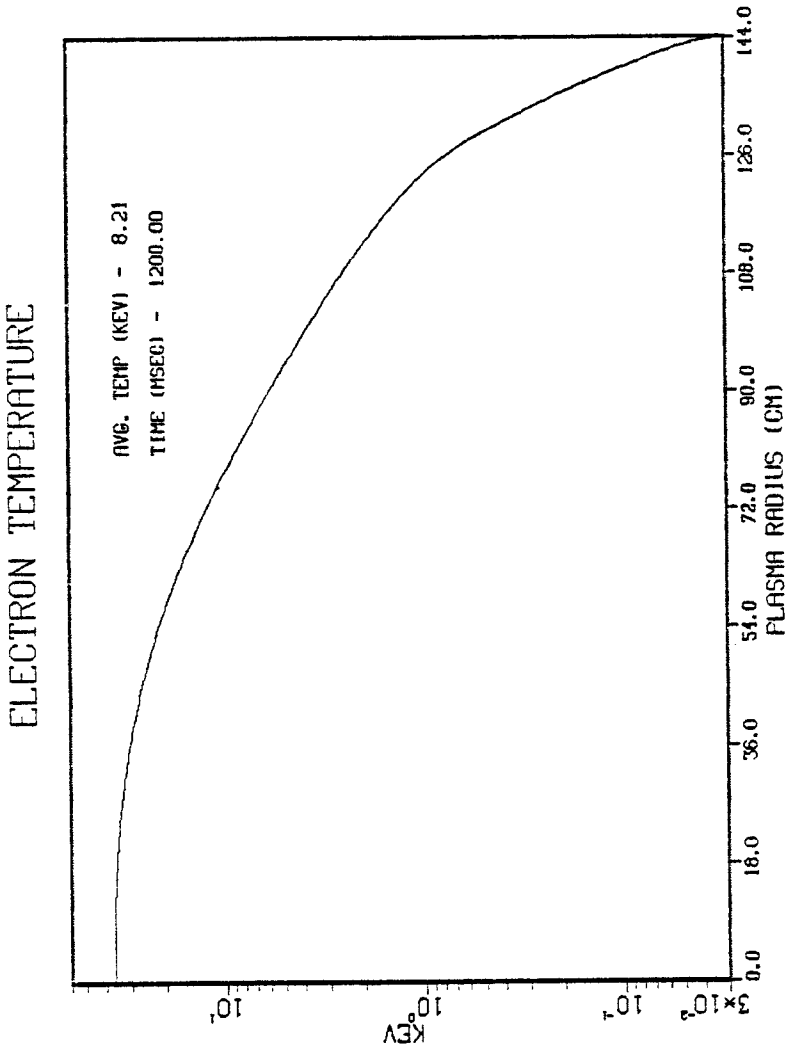

Figure (8-10) Case B: Electron temperature vs. plasma radius.

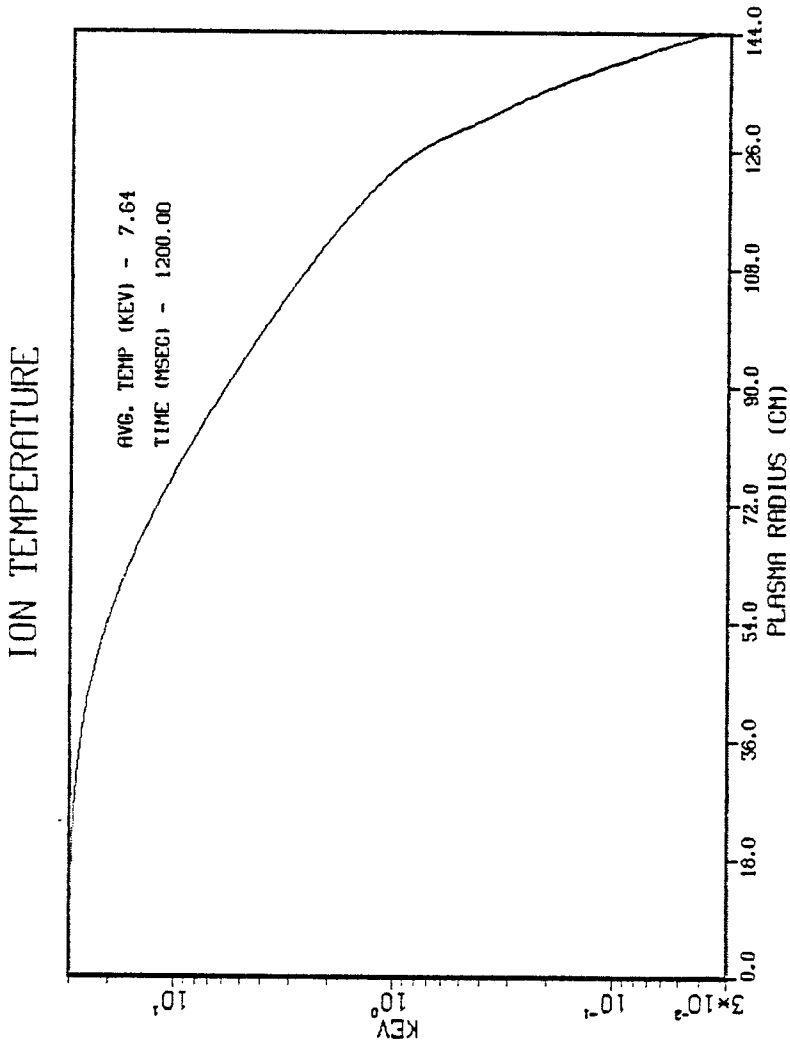

Figure (8-11) Case B: Ion temperature vs. plasma radius.

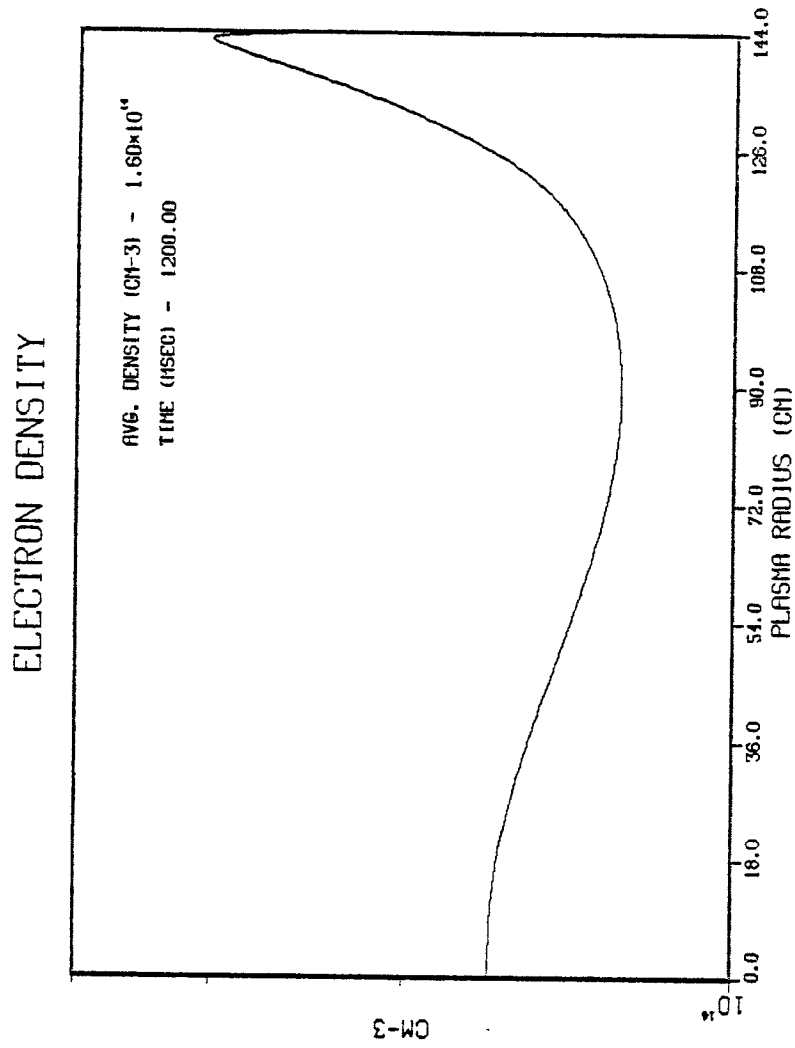

Figure (8-12) Case B: Electron temperature vs. plasma radius.

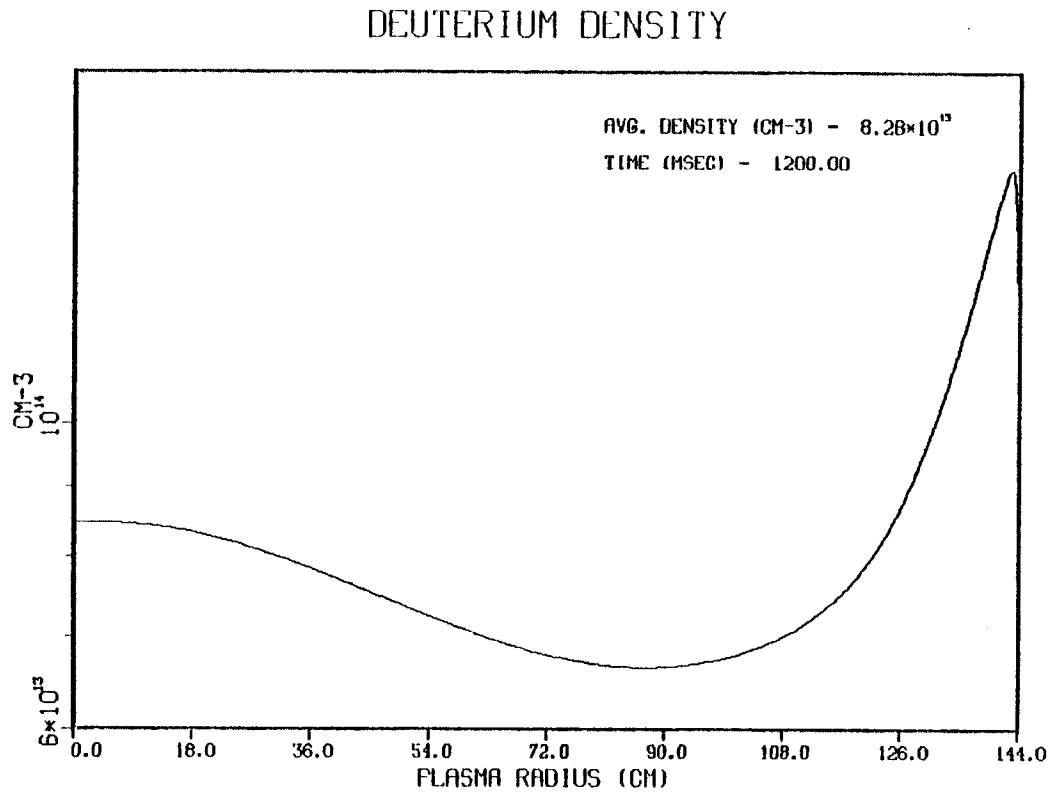

Figure (8-13) Case B: Deuterium density vs. plasma radius.

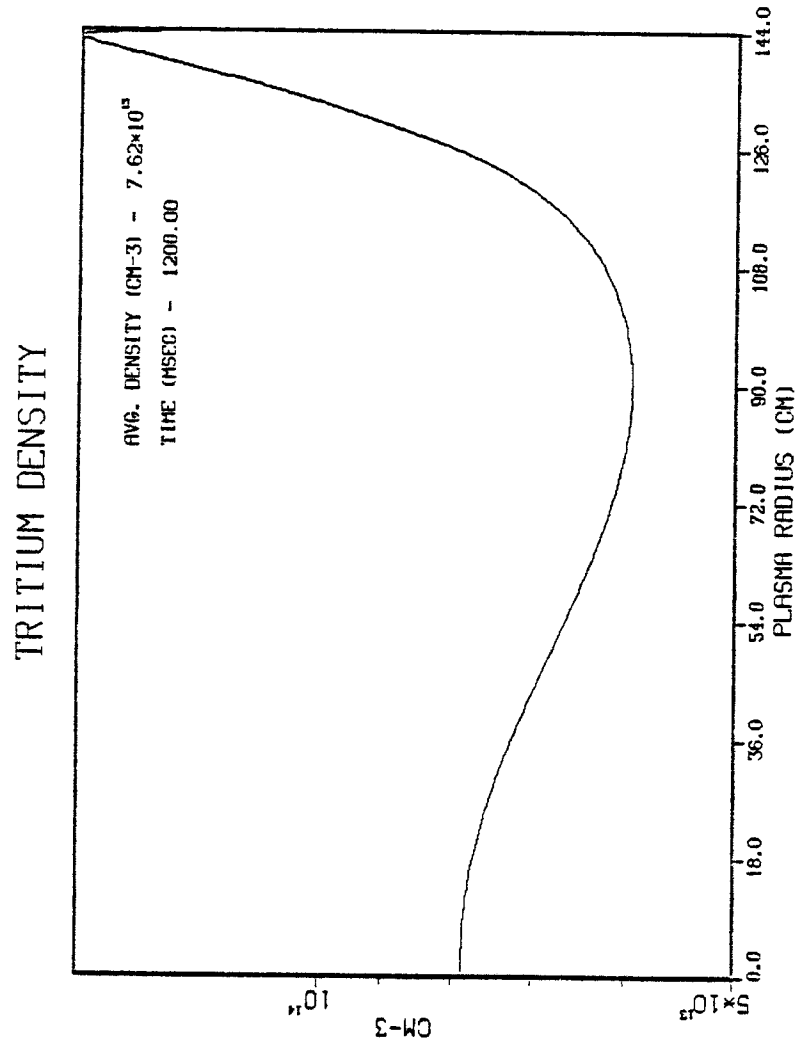

Figure (8-14) Case B: Tritium density vs. plasma radius.

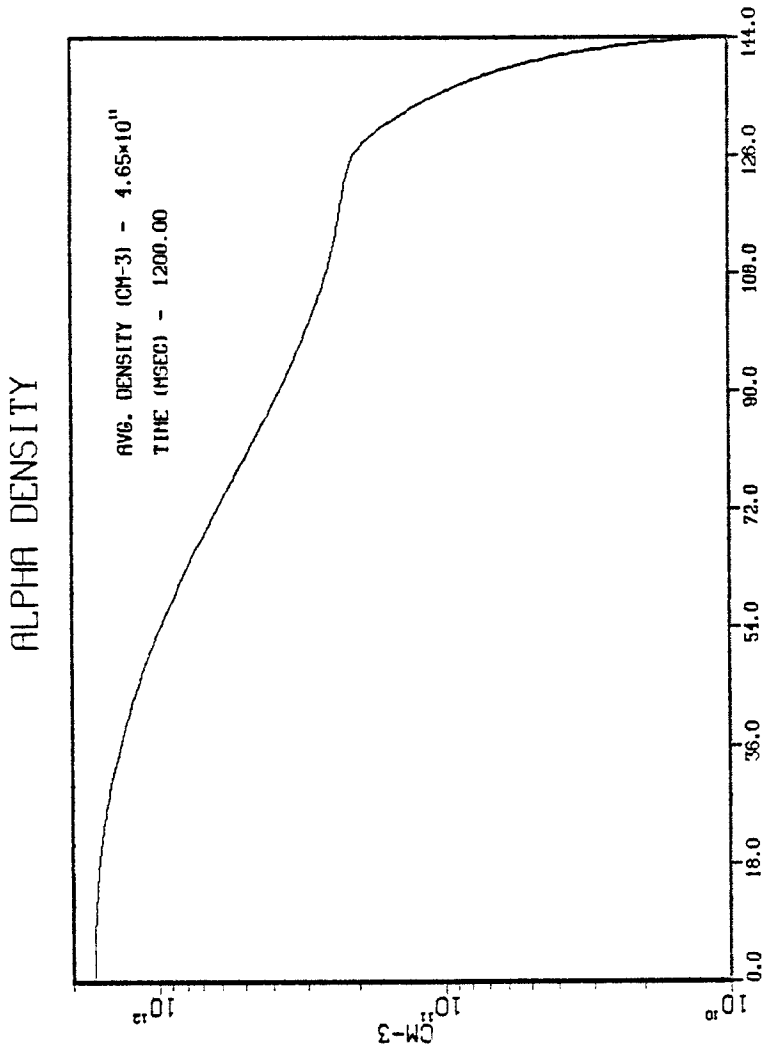

Figure (8-15) Case B: Alpha density vs. plasma radius.

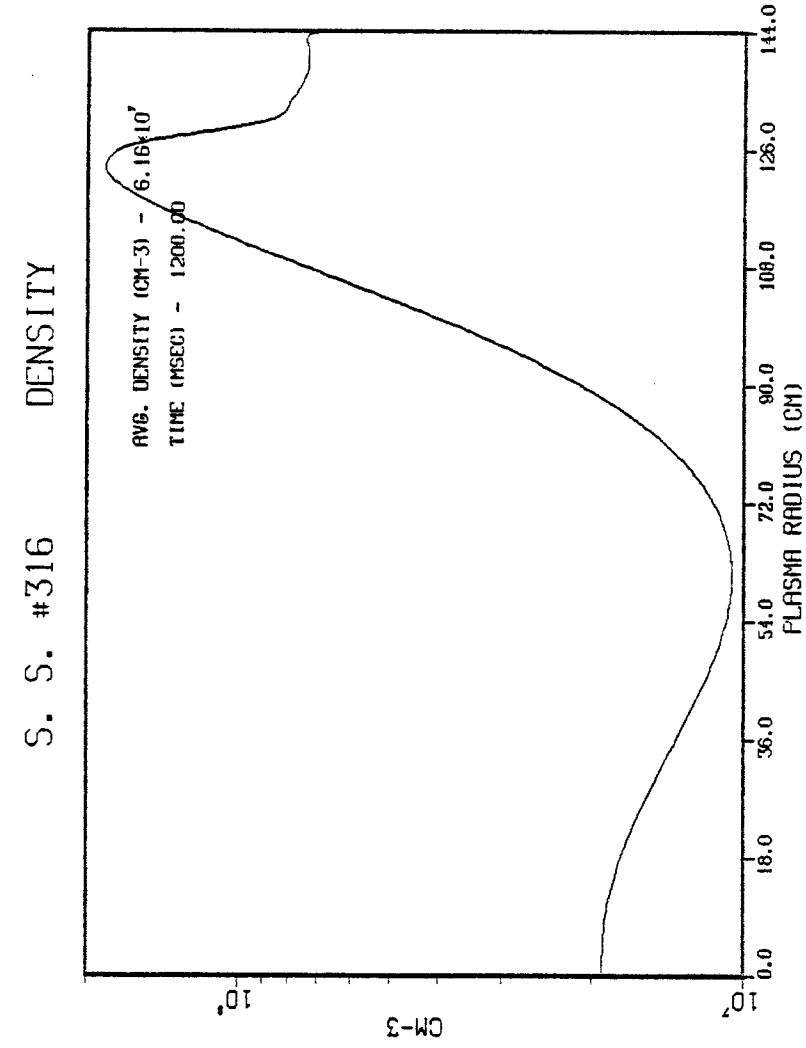

Figure (8-16) Case B: Impurity density vs. plasma radius.

controlling impurities. (2) The spectrum of charge-exchange neutrals arriving at the liner in case A is much harder (T_{eff} = 365 ev) than in case B (T_{eff} = 75 ev). This cooling of the charge exchange flux will reduce the sputtering of the liner and the subsequent pollution of the plasma. (3) The large gas feed rate of case B has inverted the edge electron and ion density profiles. In conjunction with observation (1) above, a cool, dense gas blanket has formed which will reduce wall erosion. In case A by 1200 msec no such blanket has formed. (4) While, the globally averaged alpha ash densities are nearly equal in each case, the edge alpha density in case B is greater than that in case A by more than a factor of 20, indicating that the edge plasma blanket is trapping the ash.

These observations indicate that a gas blanket can be created by the gas puffing scenarios of case B and that alpha ash trapping is occuring at the edge. The significance of the concept as an impurity control mechanism is dramatically demonstrated by refering to the spatial impurity profile of Case B (Figure 8-16). As with the alpha densities, the globally averaged impurity densities are nearly equal, yet in case B the impurity profile is sharply peaked near the edge! The trapping of the impurities in a "radiating halo" near the edge is demonstrated by observing that the central impuruity density in Case A is over 20 times larger than in Case B, indicating a purging of the core, while the

radiative losses in Case B are 60% larger than for Case A.

Admittedly these calculations are not representative of an equilibrium. However, they indicate that a transient cooler edge, cleaner discharge which preserves alpha power production can be achieved by periodic gas puffing at a rate commensurate with fueling. Similar calculations have been performed with (1)* neoclassical + PLT empirical coefficients, revealing no essential deviations from those tabulated in Table (8-2). While the central temperatures were 50% larger, the bulk temperatures were unchanged.

In order to get a better picture of the dynamics (and not just the t = 1200 msec statics) of gas blanket creation and impurity trapping, Case A was extended to 2700 msec and the profiles were monitored every 400 msec. Refering to Figs. (8-17,22) note that for t = 1600 msec, a gas blanket "spontaneously" forms at the edge in contrast to the lack of such a blanket at 1200 msec in the previous Case A simulation. While the gas feed rate is too small to "actively" create a blanket, the reemission of gas trapped in the wall provides a mechanism for the "passive" creation of blankets. That this process is the source responsible for blanket formation follows from Figure (7-2). After 1.3 seconds of bombardment the reflux from the wall is nearly 80% of the incoming flux. Hence the rise in the edge density can be correlated with the time constant of the wall source of neutral gas. Obviously only a model of plasma wall interactions can

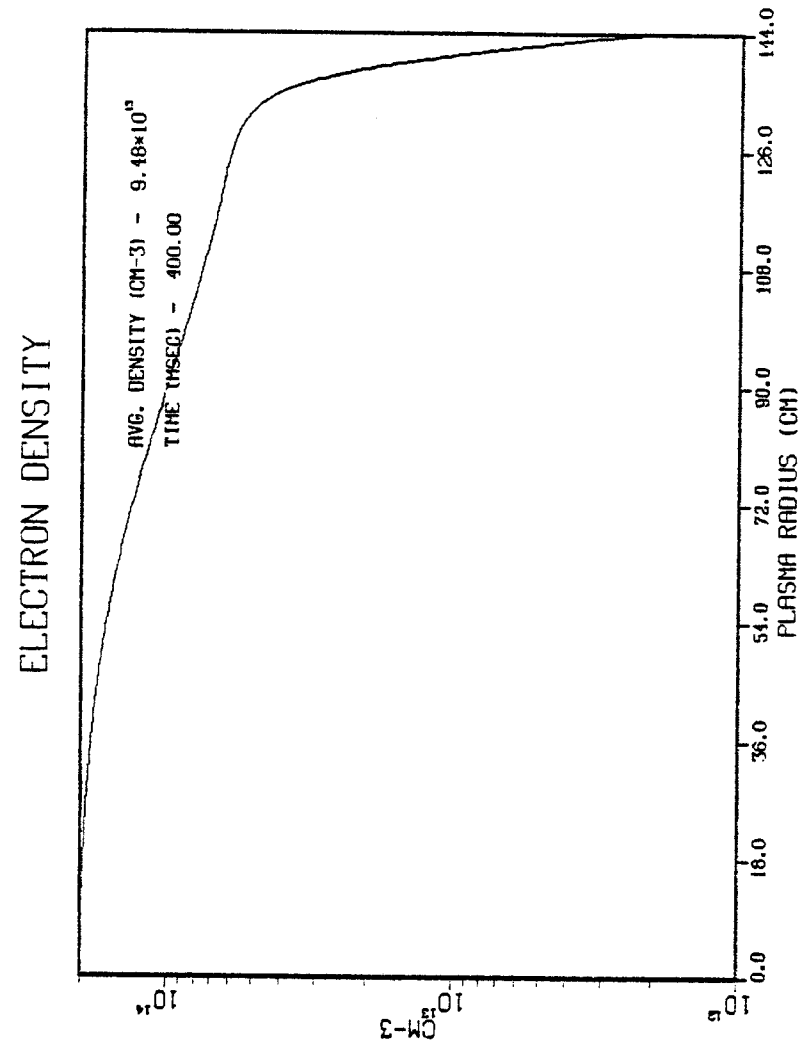

Figure (8-17) Case A: Electron density vs. plasma radius at t = 400 msec.

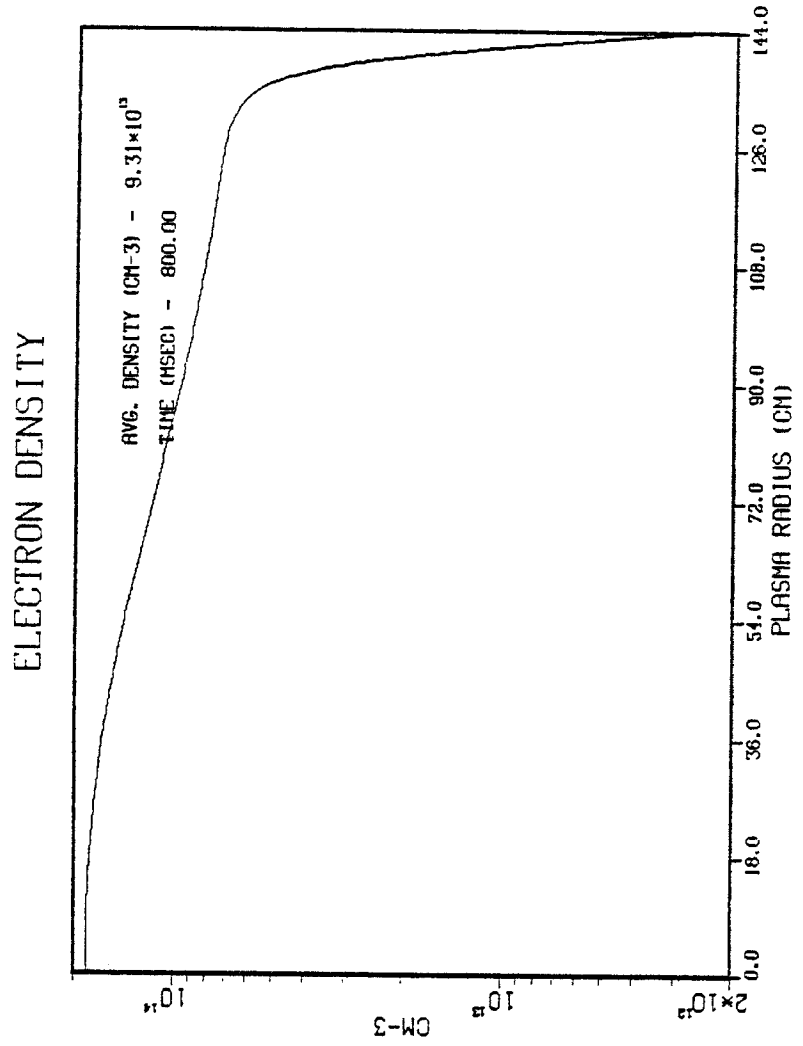

Figure (8-18) Case A: Electron density vs. plasma radius at t = 800 msec.

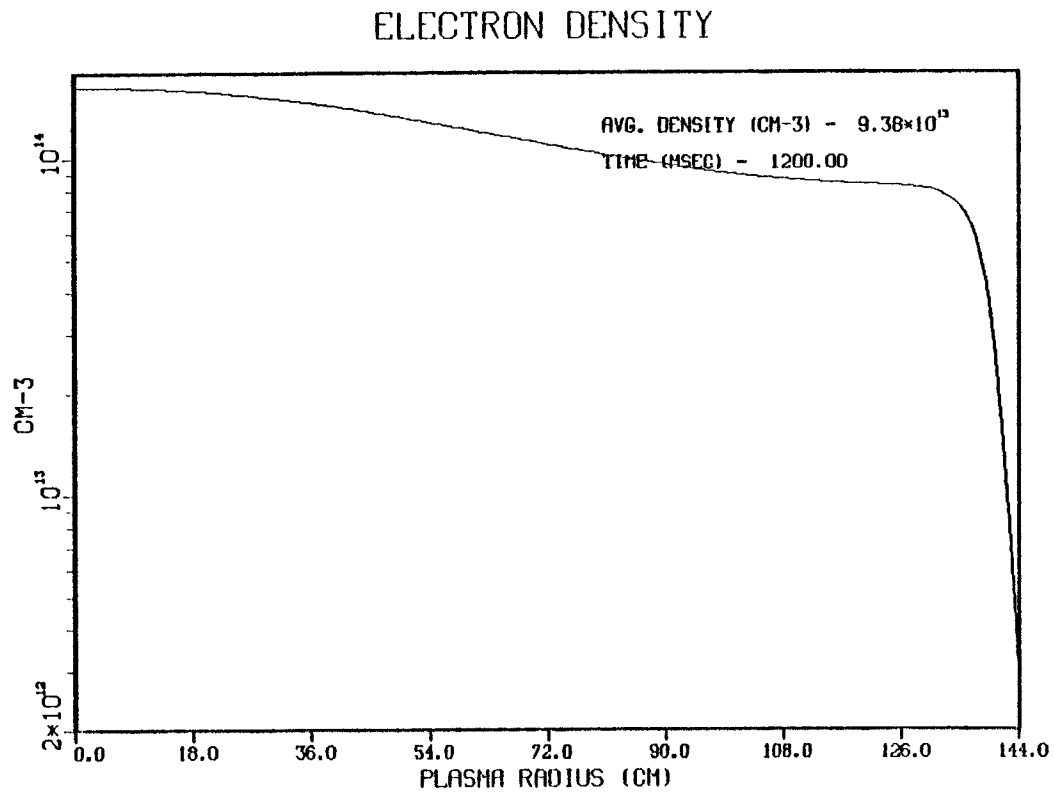

Figure (8-19) Case A: Electron density vs. plasma radius at t = 1200 msec.

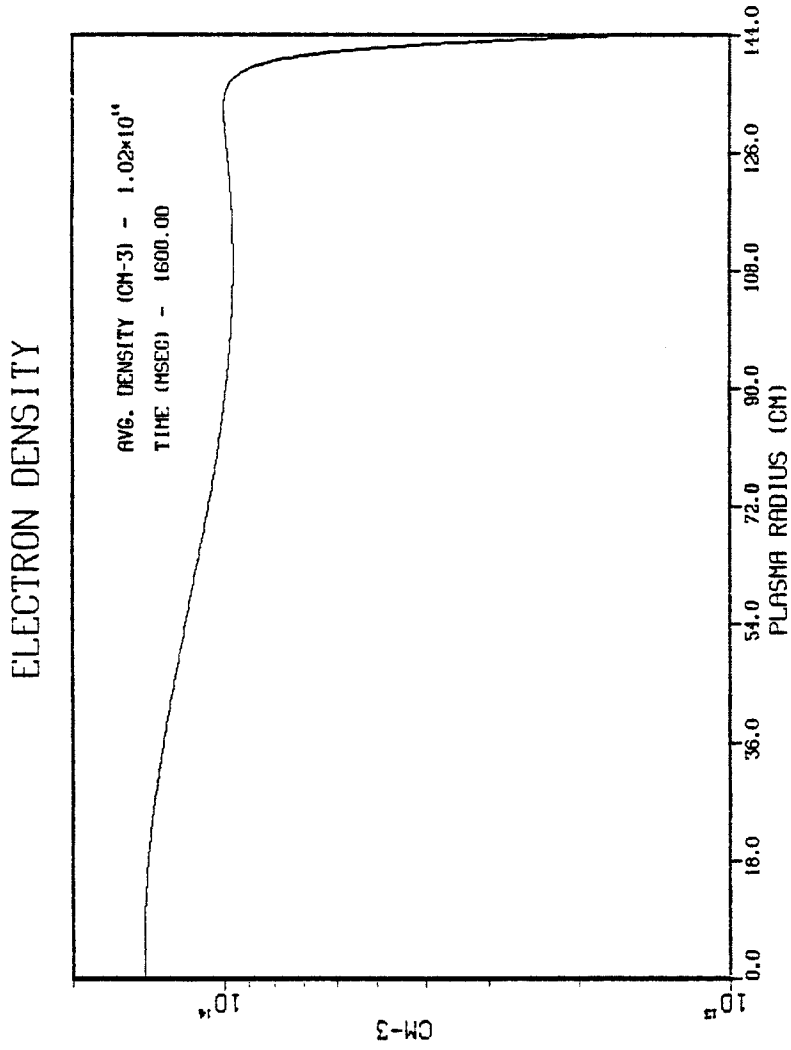

Figure (8-20) Case A: Electron density vs. plasma radius at t = 1600 msec.

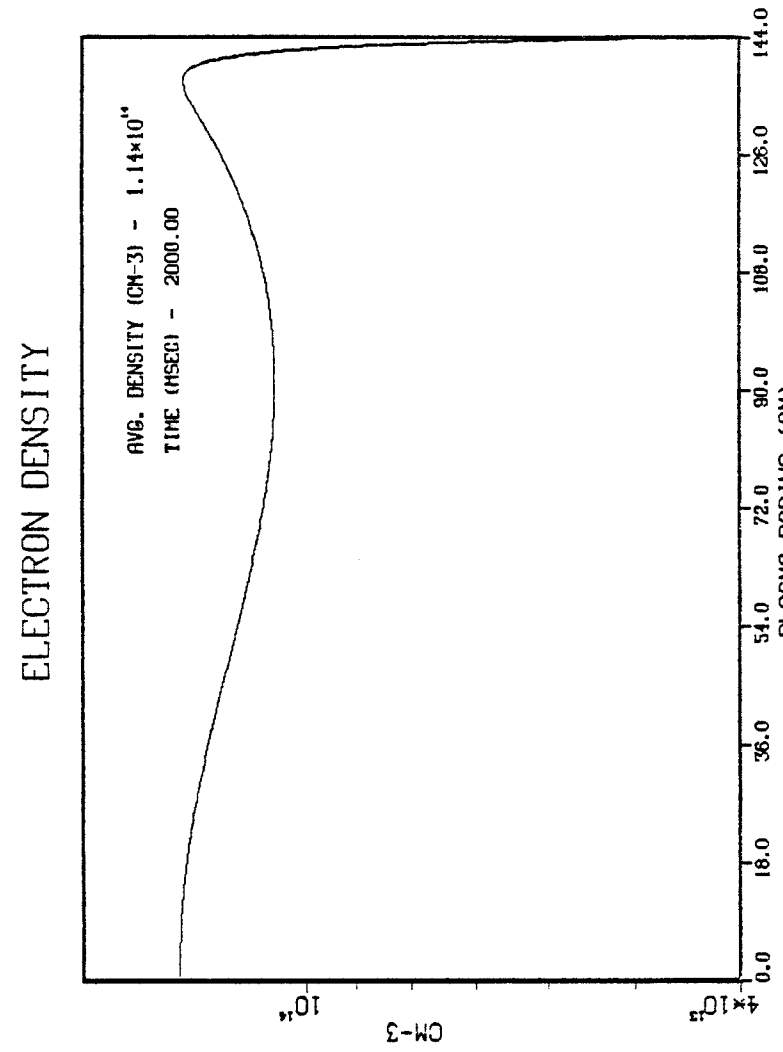

Figure (8-21) Case A: Electron density vs. plasma radius at t = 2000 msec.

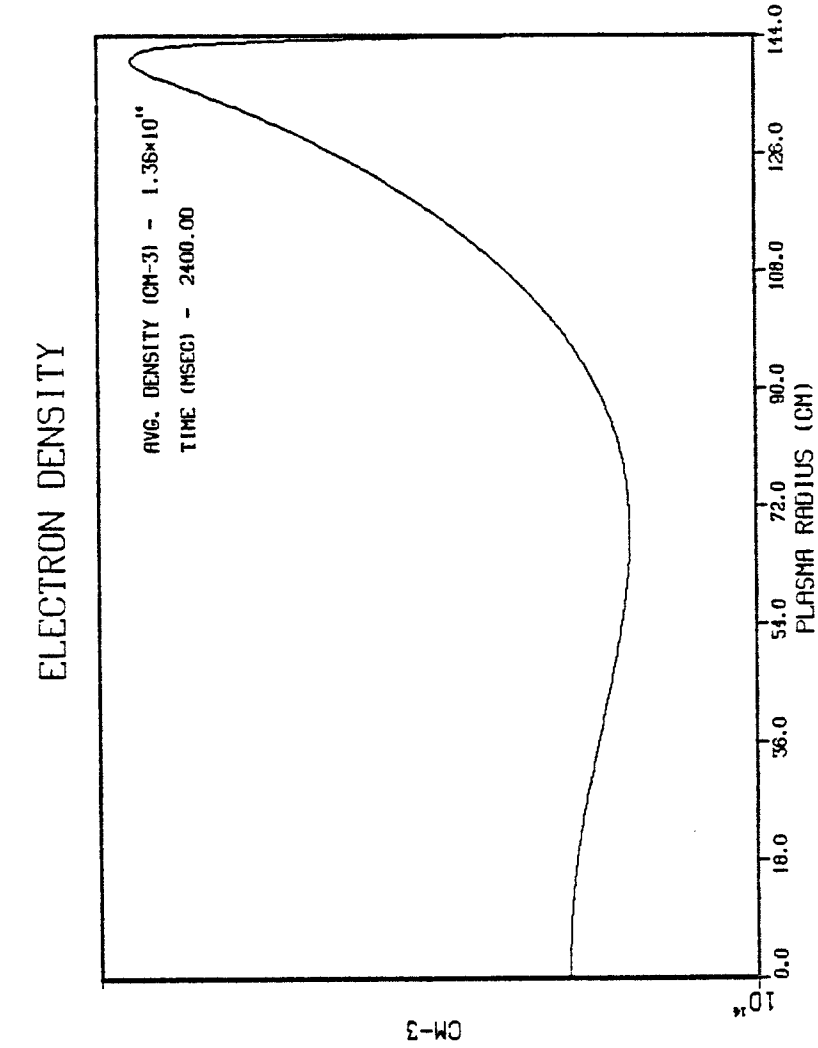

Figure (8-22) Case A: Electron density vs. plasma radius at t = 2400 msec.

supply such information, indicating that the impact of such interactions on the overall properties of the discharge are non-trivial.

The dynamics of impurity trapping can be seen in Figures (8-23,28). Initially the impurities are present throughout the plasma. But as time increases and the plasma density becomes inverted near the edge at $t = 1600$ msec, active impurity purging of the core takes place since from $t = 400$ msec to $t = 2400$ msec, the central impurity density has dropped by more than a factor of 1000! Since the question of equilibrium cannot be pursued at the present time, this trapping of impurities in the plasma blanket at the edge may be transitory. However, the model for plasma wall interactions developed in Chapter 7 in conjunction with the 1D transport model of Chapter 2 has shown that at least a transitory radiating halo with impurity control properties can be created and maintained.

While the question of successful divertorless tokamak operation can only be satisfactorily answered by an equilibrium analysis, the results presented here indicate that such divertorless operation is possible at least for a short time. If this transitory blanket can be maintained for a sufficiently long period, the prospects for divertorless operation are encouraging.

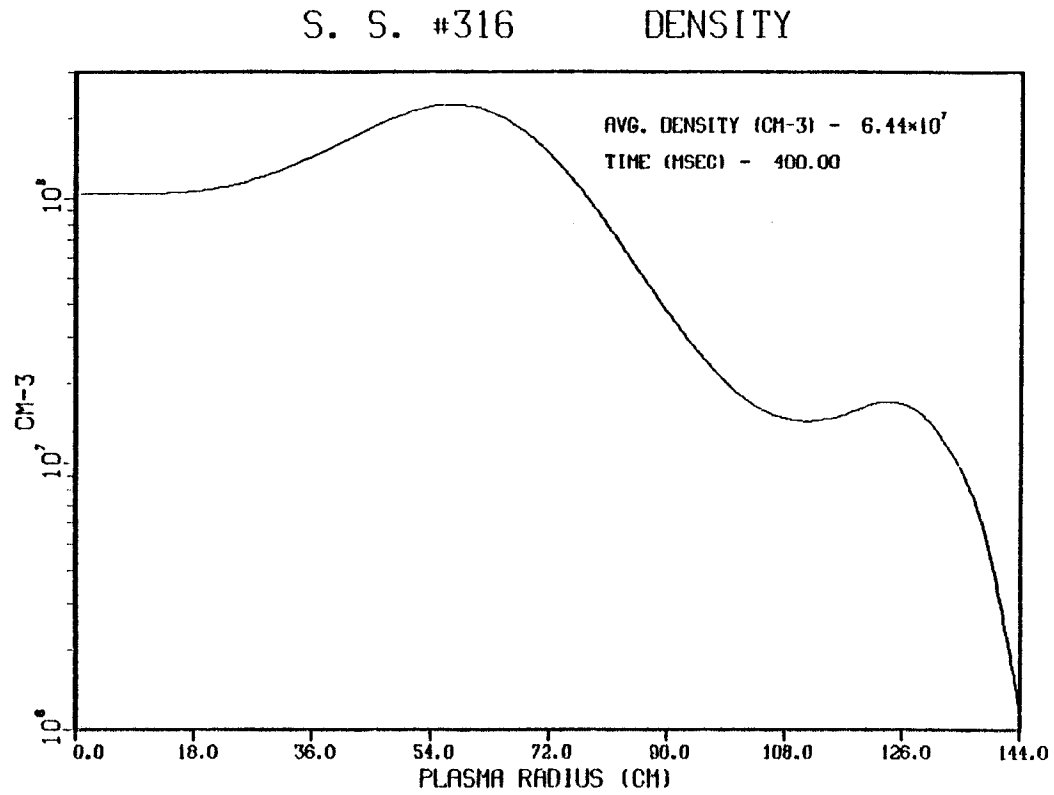

Figure (8-23) Case A: Impurity density vs. plasma radius at t = 400 msec.

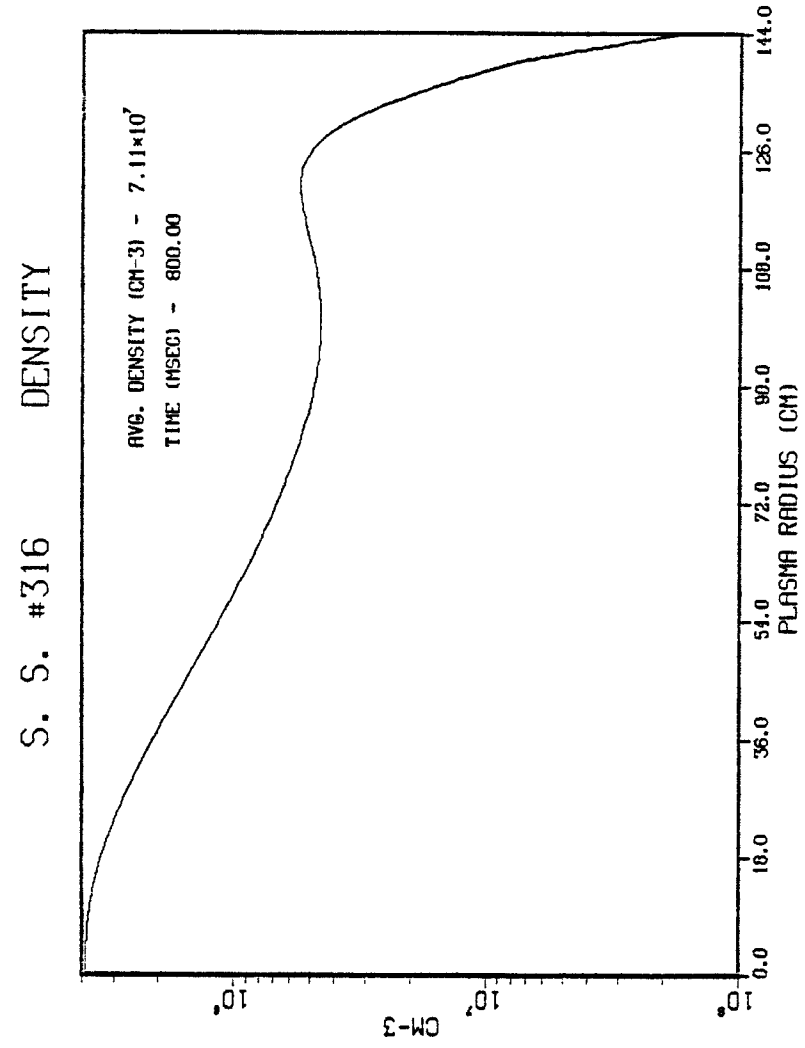

Figure (8-24) Case A: Impurity density vs. plasma radius at t = 800 msec.

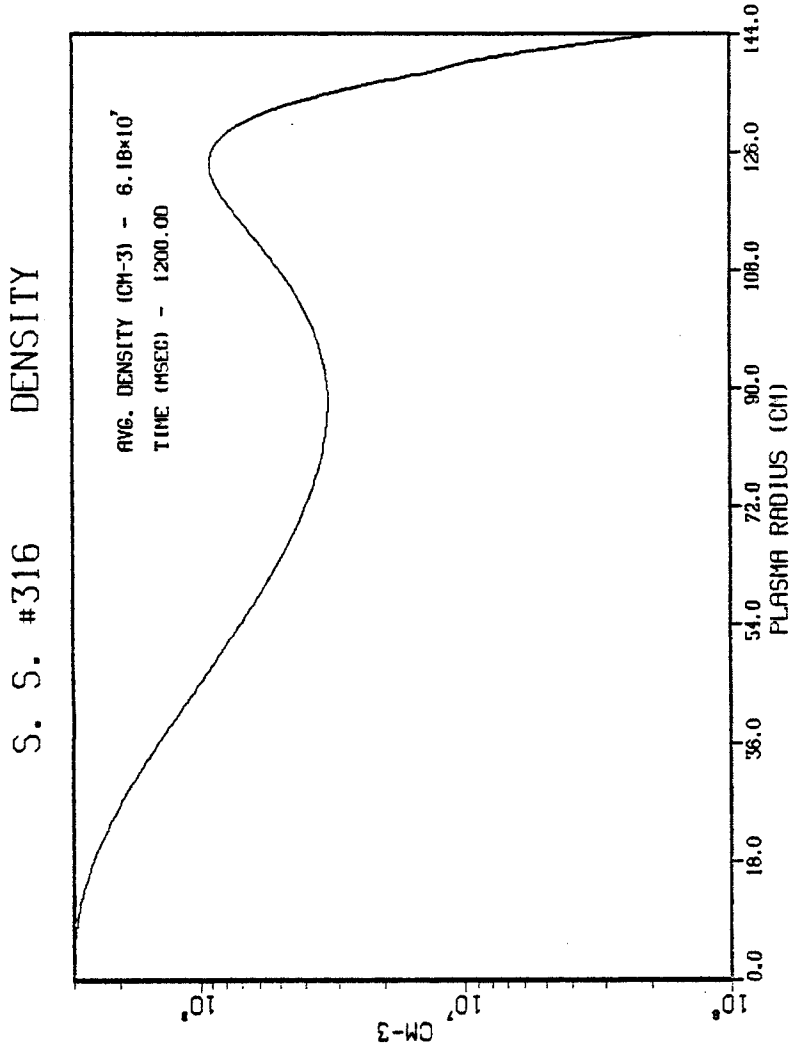

Figure (8-25) Case A: Impurity density vs. plasma radius at t = 1200 msec.

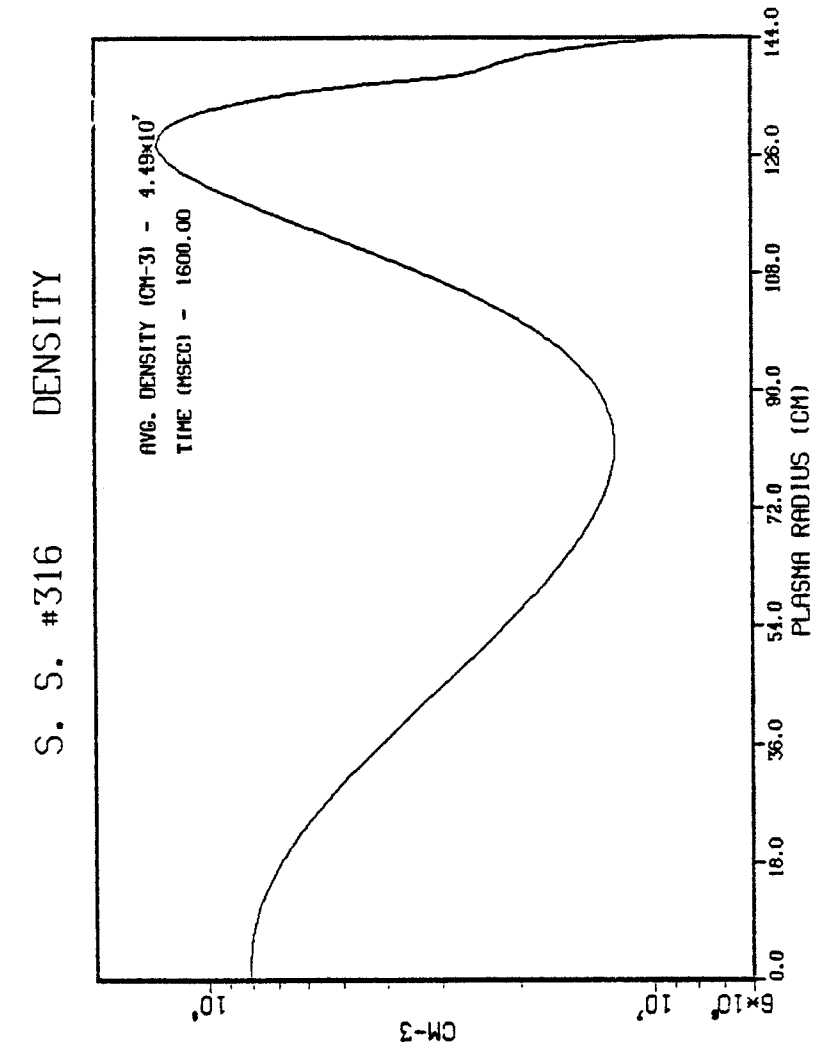

Figure (8-26) Case A: Impurity density vs. plasma radius at t = 1600 msec.

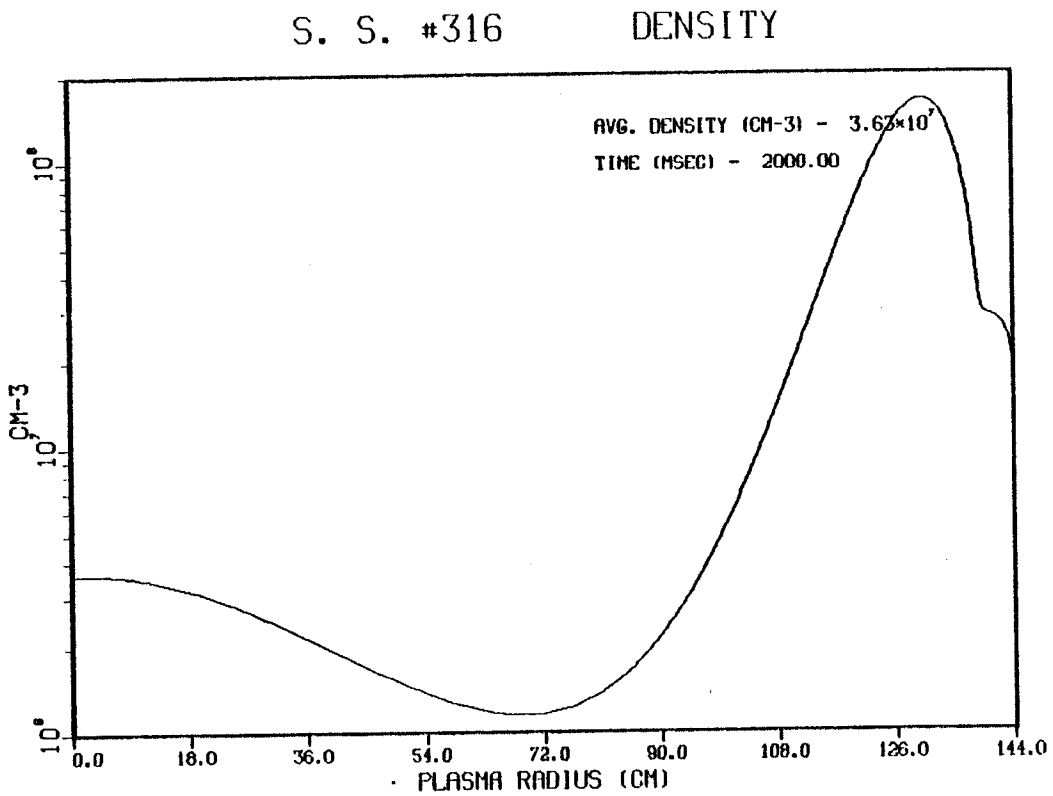

Figure (8-27) Case A: Impurity density vs. plasma radius at t = 2000 msec.

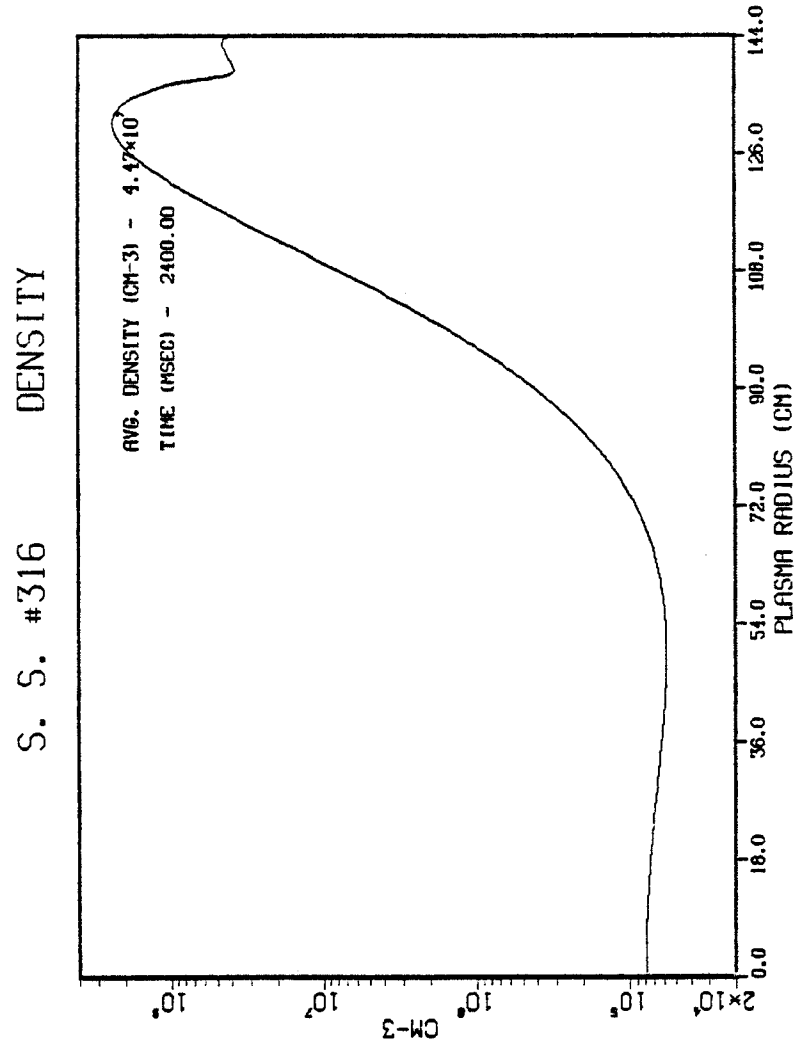

Figure (8-28) Case A: Impurity density vs. plasma radius at t = 2400 msec.

TABLE (8-1)

NUWMAK PHYSICAL PARAMETERS

Major Radius (cm)	512.5
Equiv. Circular Plasma Radius (cm)	144.
Plasma Radius at Midplane (cm)	112.5
Toroidal Magnetic Field on Axis(T)	6.05
Plasma Current (MA)	5
Plasma Volume (cm^3)	2.1×10^8
Wall Surface Area (cm^2)	3.6×10^6

TABLE (8-2)

A COMPARISON OF THE IMPACT OF MOLECULAR GAS FLOW RATE ON PLASMA PERFORMANCE (CASE A → 5×10^{22} MOLECULES/SEC, CASE B → 1×10^{23} MOLECULES/SEC.)

Variable	Units	Case A	Case B
$T_e(o)$	KeV	36.6	36.4
$T_i(0)$	KeV	30.8	29.6
$n_i(o)$	cm^{-3}	1.6×10^{14}	1.6×10^{14}
$n_\alpha(o)$	cm^{-3}	1.9×10^{12}	1.7×10^{12}
$n_z(o)$	cm^{-3}	4.6×10^{8}	1.9×10^{7}
$T_e(a)$	eV	83	32
$T_i(a)$	eV	115	36
$n_i(a)$	cm^{-3}	2.6×10^{12}	2.2×10^{14}
$n_\alpha(a)$	cm^{-3}	5.1×10^{8}	1.1×10^{10}
$n_z(a)$	cm^{-3}	1.9×10^{6}	6.5×10^{7}
$\bar{T}_e$	KeV	9.2	8.2
$\bar{T}_i$	KeV	8.9	7.6
$\bar{n}_i$	cm^{-3}	8.8×10^{13}	1.6×10^{14}
$\bar{n}_\alpha$	cm^{-3}	4.4×10^{11}	4.7×10^{11}
$\bar{n}_z$	cm^{-3}	6.7×10^{7}	6.2×10^{7}

TABLE (8-2) (continued)

Variable	Units	Case A	Case B
P_{α}	MW	72	77
P_{cx}	MW	7.6	3.2
P_{Rad}	MW	3.6	5.7
Γ_{cx}	$cm^{-2}-sec^{-1}$	2.9×10^{16}	6×10^{16}
T_{eff}	eV	365	75
$\bar{n}_i$(shadow)	cm^{-3}	2.2×10^{12}	6.2×10^{12}
$\bar{n}_{\alpha}$(shadow)	cm^{-3}	3.8×10^{8}	3.1×10^{8}
$\bar{n}_z$(shadow)	cm^{-3}	8×10^{4}	4.2×10^{3}
$\bar{T}_e$(shadow)	eV	43	18
$\bar{T}_i$(shadow)	eV	65	31
E_{cold}	eV	28	22
E_{hot}	eV	91	52
P_{LIM}	sec^{-1}	3.2×10^{23}	6.2×10^{23}
L_{LIM}	W/cm^2	241	198

CHAPTER 9

SUMMARY AND CONCLUSIONS

The impact of various plasma wall interactions on the burn dynamics of tokamaks can now be quantified using a zero dimensional model of the scrape-off zone. By incorporating this model into a one dimensional radial transport code, self-consistent boundary conditions and influxes can be predicted. This model removes several of the arbitrary assumptions currently in tokamak transport codes and will enable extrapolations into future reactor regimes to be made with greater confidence.

While the present numerical limitations placed on the 1D code by this edge model prohibit the pursuit of true plasma equilibria, the results obtained for times early in the discharge tend to support the concept of divertorless tokamak operation via the gas blanket approach to impurity control. Simulations show that the creation of the blanket can be the result of both active gas puffing at a rate commensurate with fueling and through the passive introduction of neutral gas into the scrape-off layer by the diffusion of wall-trapped gas.

Significant trapping of both alpha ash and impurities by the blanket at the edge is observed. The buildup of alpha ash in this layer will determine to a large extent the length of burn

times in non-divertor devices. Since an accurate evaluation of this and other edge-related conditions is critical to the resolution of this and other edge-related questions, the predictive power of this edge model can easily be recognized.

While this work has concentrated on the development of a comprehensive edge model for tokamaks, many improvements in the code can and should be made in the future. A partial list would include: (1) the creation of a radially dependent model to more properly account for the short mean free path of thermal diatomic molecules in the scrape-off zone, (2) the simulation of plasma equilibria by making the core calculation less sensitive to fluctuationsin the edge boundary conditions, thereby allowing definitive statement within the transport model to be made regarding such questions as steady-state blanket and halo performance, estimation of limiter and wall erosion rates, and the fueling requirements for a steady-state burn, (3) the optimization of edge radiation by considering several low Z impurities and their impact on global plasma performance, and (4) the use of RF to enhance the diffusion coefficients at the edge, thereby increasing the low Z recycling rate and increasing the power radiated from the edge.

As the next generation of plasma experiments enters the reactor regime, more relevant plasma wall data will become available for inclusion in the edge model. However, even though

incomplete at the present time, the complexity and data base of the model is such that it will prove to be a valuable tool in the analysis and optimization of tokamak discharges.